LIDAR APPLICATIONS FOR COASTAL ENGINEERING: SEA BOTTOM MAPPING AND WATER WAVE MEASUREMENT

BY

JENNIFER L. IRISH AND NOBUHISA KOBAYASHI

RESEARCH REPORT NO. CACR-05-02

CENTER FOR APPLIED COASTAL RESEARCH

Ocean Engineering Laboratory
University of Delaware
Newark, Delaware 19716

ACKNOWLEDGMENTS

This report is my dissertation submitted in April 2005 to the Faculty of the University of Delaware in partial fulfillment of the requirements for the degree of Doctor of Philosophy in Civil Engineering.

I am especially grateful for the opportunity provided by my advisor, Dr. Nobuhisa Kobayashi, to complete this dissertation. I also thank Dr. Ib Svendsen for his leadership and guidance during my first years of study at the University of Delaware.

I am deeply grateful to my friends and colleagues at the Joint Airborne Lidar Bathymetry Technical Center of Expertise (JALBTCX), whose technical guidance and moral support were invaluable in completing this work: Ms. Jennifer McClung Wozencraft, Mr. Gary Guenther, Dr. Grant Cunningham, Mr. Larry Parson, Ms. Mary Whittington, Ms. Frida Lejdebrink Greathouse, and most especially Mr. Jeff Lillycrop.

The U.S. Army Engineer Research and Development Center through the JALBTCX and the Coastal Program–Wave Research sponsored this work with the SHOALS airborne lidar bathymetry system and the lidar wave gage, respectively. I thank Mr. Jeff Lillycrop and Dr. Donald Resio, the managers of these programs, for the opportunity to lead these studies.

TABLE OF CONTENTS

LIST OF TABLES v
LIST OF FIGURES vi
ABSTRACT xii
1. INTRODUCTION 1
1.1 Lidar Depth Measurement 1
1.2 Lidar Wave Measurement 5
2. AIRBORNE LIDAR FOR SEA BOTTOM MAPPING 8
2.1 History of Airborne Lidar Bathymetry–A Literature Review 8
2.1.1 Proof-of-Concept Testing 8
2.1.2 First-Generation Airborne Lidar Bathymetry Systems 9
2.1.3 Second-Generation Airborne Lidar Bathymetry Systems 10
2.1.3.1 The Airborne Oceanographic Lidar System 10
2.1.3.2 Other Efforts 12
2.1.4 Third-Generation Airborne Lidar Bathymetry Systems 12
2.1.4.1 The LARSEN-500 System 12
2.1.4.2 Other Efforts 13
2.1.5 Fourth-Generation Airborne Lidar Bathymetry Systems 14
2.1.5.1 The LADS System 15
2.2 Airborne Lidar Bathymetry Principles 15
2.2.1 Lidar Ranging 17
2.2.2 Water Depth Measurement 18
2.2.3 Horizontal and Vertical Positioning 23
2.3 The SHOALS System 24
2.3.1 SHOALS Transceiver 27
2.3.2 SHOALS Horizontal and Vertical Positioning 29
2.3.3 Supplemental Video 31
2.3.4 Post-Flight Processing 31
2.3.5 SHOALS Performance 32
2.4 Detailed Mapping of Complex Coastal Environments: Tidal Inlets 34
2.4.1 Moriches Inlet, NY 35
2.4.2 New Pass, FL: A Study of Morphologic Evolution 39
2.4.2.1 Field Measurement Summary 41
2.4.2.1.1 SHOALS Bathymetry 41
2.4.2.1.2 Hydraulic Conditions 42

2.4.2.2 Data Analysis 45
2.4.2.3 Results 55
2.5 Beach Nourishment Project Design 55
2.5.1 Longboat Key, FL 56
2.5.2 Island Beach State Park, NJ 58
2.5.3 St. Joseph, MI 58
2.5.4 Presque Isle, PA 61
2.5.5 Data Analysis 63
2.5.6 Results 65
2.6 Storm Response: Hurricane Opal 71
2.6.1 Hurricane Opal 72
2.6.2 Panama City Beach, FL 74
2.6.3 East Pass, FL 79
2.7 Regional-Scale Mapping 86
2.7.1 The Hawaiian Islands 87
2.7.2 The Gulf of Mexico: Surveys to Support Regional Sediment Management 91
3. FIXED-PLATFORM LIDAR FOR WAVE MEASUREMENT 93
3.1 History of Non-Intrusive Wave Measurement–A Literature Review 95
3.1.1 Radar Methods 95
3.1.1.1 Radar Theory 95
3.1.1.2 Determination of Wave Characteristics 97
3.1.1.3 Radar Sensors for Ocean and Coastal Applications 101
3.1.2 Photogrammetric Methods 102
3.1.3 Video Methods 102
3.1.4 Lidar Methods 103
3.1.4.1 Lidar Theory 104
3.1.4.2 Lidar Sensors for Wave Measurement 104
3.2 Prototype Design 107
3.2.1 Sensor Platform 108
3.2.2 Data Acquisition Suite 110
3.3 Field Experiment 110
3.3.1 Experimental Setup 110
3.3.2 Data Collection 113
3.3.3 Sensor Difficulties 115
3.4 Sensitivity to Environmental Conditions 116
3.4.1 Nadir Angle and Wind Speed 117
3.4.2 Wave Climate 119
3.4.3 Sensor Elevation 119

3.4.4 Rain 120
3.4.5 Ambient Light Conditions 123
3.5 Accuracy for Measuring Spectral Wave Parameters 123
3.5.1 Spectral Analysis Methodology 123
3.5.1.1 Fourier Series, Fourier Transform, and Correlation Functions 123
3.5.1.2 Wave Spectra and Wave Characteristics 127
3.5.1.2.1 Non-Directional Wave Spectra 127
3.5.1.2.2 Directional Wave Spectra 128
3.5.1.2.3 Wave Spectra Characteristics 129
3.5.1.3 Application to Discrete Time Series 130
3.5.2 Data Processing 131
3.5.3 Comparison with PUV 133
3.5.4 Comparison with 8-m Array 142
3.6 Future Applications 148
3.6.1 Additional Prototype Testing 148
3.6.2 Operational Lidar Wave Gage Design 149
4. CONCLUSIONS 152
4.1 Future Direction for Airborne Lidar Bathymetry Advancements 152
4.1.1 Shallow Water Depths and Shoreline Position 152
4.1.1.1 Depth Measurement in the Surf Zone 154
4.1.1.2 Detection of Coincident Surface and Bottom Returns 155
4.1.2 Sea Bottom Classification 156
4.1.3 Depth Measurement in Turbid Waters 157
4.2 Future Non-Intrusive Wave Measurement 159
4.2.1 Surf Zone and Swash Zone LWG Applications 159
4.2.2 Other Technologies 160
4.3 Concluding Remarks 160
BIBLIOGRAPHY 162

LIST OF TABLES

Table 2.1 Summary of SHOALS system specifications. 26

Table 2.2 SHOALS operation and performance characteristics. 30

Table 2.3 Mean wave conditions near New Pass, FL in 1994. 47

Table 2.4 Volume changes at New Pass, FL. 49

Table 2.5 Computed sediment volume differences. 66

Table 3.1 Spectral analysis parameters. 133

Table 3.2 Statistics from LWG and PUV comparisons. 136

Table 3.3 Operational LWG design requirements. 150

Table 4.1 Existing operational ALB capabilities. 153

LIST OF FIGURES

Figure 1.1 Conventional United States navigation project survey plan (a) versus airborne lidar survey plan (b). Location is East Pass, FL (from Irish, 2000). 3

Figure 1.2 ALB system survey capabilities versus boat-mounted multibeam acoustic system survey capabilities (modified from Irish, 2000). 4

Figure 1.3 Combined in situ (diamond) and remote (circles) measurement scheme at a navigation project (East Pass, FL; from Irish et al., 2001)..... 6

Figure 2.1 ALB operating principle (modified from Irish, 2000)..... 16

Figure 2.2 Definition of laser pulse width and maximum traveling time, $t_{L\,max}$ (modified from Wehr and Lohr, 1999)..... 19

Figure 2.3 Water column and interface effects on system performance (modified from Irish, 2000)..... 20

Figure 2.4 Idealized blue-green laser waveform showing the principle return signal components (modified from Guenther et al., 2000)..... 22

Figure 2.5 (a) SHOALS system mounted on a Twin Otter and (b) layout of SHOALS system inside Twin Otter (from Irish, 2000)..... 25

Figure 2.6 SHOALS post-processing window showing the lidar waveforms collected for each laser pulse..... 28

Figure 2.7 SHOALS scan and flight patterns (from Irish, 2000)..... 30

Figure 2.8 SHOALS field verification (modified from Irish et al., 2000a). 33

Figure 2.9 Location map for Moriches Inlet, NY. 36

Figure 2.10 SHOALS survey in 1994 at Moriches Inlet, NY (from Irish and White, 1998)..... 37

Figure 2.11 Bathymetric difference plot between 1994 and 1996 SHOALS surveys at Moriches Inlet, NY. The 1-m erosion contours are highlighted in red and the 1-m accretion contours are highlighted in blue (modified from Irish and White, 1998). 38

Figure 2.12 Location map for New Pass, FL (from Irish and Lillycrop, 1997). 40

Figure 2.13 New Pass, FL lidar bathymetry, December 1994 (from Irish and Lillycrop, 1997). 43

Figure 2.14 Three-dimensional view of New Pass, FL lidar bathymetry, December 1994. North is to the left, and the area shown is 1.5 km cross-shore by 3.0 km alongshore (from Irish and Lillycrop, 1997). 44

Figure 2.15 (a) wave height, (b) water level, and (c) wave direction from USACE wave gage near New Pass between March and December 1994. Julian day 60 is 1 March 1994 (from Irish and Lillycrop, 1997). 46

Figure 2.16 New Pass, FL control areas for volume computations (from Irish and Lillycrop, 1997). 48

Figure 2.17 Accretion (grey) and erosion (black) at New Pass, FL between March and September 1994 (from Irish and Lillycrop, 1997)..... 50

Figure 2.18 Accretion (grey) and erosion (black) at New Pass, FL between September and December 1994 (from Irish and Lillycrop, 1997)..... 52

Figure 2.19 Cross-sections through the ebb shoal perpendicular to the dredge cut. The cross-sections are taken along A-A' shown on Figure 2.18. In this figure, the original dredge cut is indicated by the steep slope between stations 2+00 and 3+00 (from Irish and Lillycrop, 1997). 53

Figure 2.20 Navigation channel thalweg positions at New Pass, FL (from Irish and Lillycrop, 1997). 54

Figure 2.21 Location map for four beach nourishment projects..... 57

Figure 2.22 Longboat Key, FL, November 1995: (a) representative section of SHOALS bathymetry and (b) simulated profile bathymetry at 300-m spacing. All depths are in meters referenced to NGVD29 (from Irish et al., 1997)..... 59

Figure 2.23 Island Beach State Park, NJ, June 1994: (a) SHOALS bathymetry and (b) simulated profile bathymetry at 300-m spacing. All depths are in meters referenced to NGVD29 (from Irish et al., 1997). 60

Figure 2.24 St. Joseph, MI, August 1995: (a) representative section of SHOALS bathymetry and (b) simulated profile bathymetry at 300-m spacing. All depths are in meters referenced to IGLD (from Irish et al., 1997)..... 62

Figure 2.25 Presque Isle, PA, August 1995: (a) representative section of SHOALS bathymetry and (b) simulated profile bathymetry at 300-m spacing. All depths are in meters referenced to IGLD (from Irish et al., 1997)..... 64

Figure 2.26 Measured beach fill volume error versus alongshore profile spacing (modified from Irish et al., 1997). 67

Figure 2.27 Cost error at Presque Isle, PA (from Irish et al., 1997). 70

Figure 2.28 Florida panhandle indicating Panama City Beach and East Pass (from Irish et al., 1996)..... 72

Figure 2.29 Infrared satellite image of Hurricane Opal at 1300 CDT, 4 October 1995 (from Irish et al., 1996)..... 73

Figure 2.30 Pre-storm and post-storm bathymetry at Panama City Beach, FL (7 km along-shore; depths are in feet referenced to NGVD29; 1 ft = 0.3048 m; from Irish et al., 1996). 76

Figure 2.31 Three-dimensional view of scour formation at Panama City Beach, FL (location is shown in Figure 2.30b; east is to the right; from Irish et al., 1996). 77

Figure 2.32 Representative pre-storm and post-storm profiles (Profile 32 as seen on in Figure 2.30; depths are in feet relative to NGVD29; 1 ft = 0.3048 m; from Irish et al., 1996). 79

Figure 2.33 Depth change between pre-storm and post-storm surveys at Panama City Beach, FL. Light grey indicates accretion and black indicates erosion (7 km along-shore; depths are in feet referenced to NGVD28; 1 ft = 0.3049 m; from Irish et al., 1996). 80

Figure 2.34 Post-storm SHOALS bathymetry at East Pass, FL. Depths are in feet referenced to NGVD29 where 1 ft = 0.3048 m (from Irish et al., 1996). 82

Figure 2.35 Aerial photograph of East Pass, FL after Hurricane Opal (north is to top; from Irish et al., 1996). 84

Figure 2.36 Depth change between pre- and post-storm surveys at East Pass, FL. Depth changes are in feet where 1 ft = 0.3048 m. Areas of accretion are in grey and areas of erosion are in black (from Irish et al., 1996). 85

Figure 2.37 Hawaiian Islands coastlines surveyed with SHOALS (shown in black) in 1999 (from Irish, 2000). 88

Figure 2.38 SHOALS data at Maui, HI. Shoreline is black line. Depth contours are every 3 m. North is to top (from Irish, 2000)..... 89

Figure 2.39 Image of SHOALS data (right) and aerial photograph (left) at Molokai, HI created by USGS (modified from Wozencraft et al., 2000). Shoreline is to top and offshore to bottom. 90

Figure 2.40 RSMDP (a) area and (b) DTM generated from SHOALS data collected in 1999 (north is to the top; from Wozencraft and Irish, 2000). 92

Figure 3.1 Location of FRF, Duck, NC. 94

Figure 3.2 Electromagnetic backscattering (modified from Driver, 1985)..... 96

Figure 3.3 Idealized Doppler spectrum..... 98

Figure 3.4 Prototype LWG diagram. 109

Figure 3.5 LWG, PUV, and 8-m linear array locations at the FRF and December 1999 bathymetry. Depth contours are in meters and position is relative to local FRF horizontal coordinate system. 111

Figure 3.6 LWG and PUV mounted on SIS. 112

Figure 3.7 Footprint locations on water surface for rangefinders RF1, RF2, RF3, and RF4. 112

Figure 3.8 Sample LWG surface elevation time series (11 December 1999 at 0943 EST). 114

Figure 3.9 Percentage of quality data collected relative to wind speed and nadir angle for all data collected. In the center plot, grid boxes are color-coded from black to light grey corresponding to 0% quality data to 100% quality data, respectively. A blank, or white, grid box indicates no data were collected for that wind speed and nadir angle pair. In the plots on the left and on the bottom, filled diamonds represent the subset of data with nadir angle of 10 deg or less and wind speed of 5 m/s or more. 118

Figure 3.10 Horizontal variation in footprint position: (a) 8-cm variation with spectral wave height of 0.6 m and (b) 15-cm variation with spectral wave height of 1.3 m. 120

Figure 3.11 Percentage of quality data collected relative to sensor elevation above water surface. Filled diamonds represent the subset of data with nadir angle of 10 deg or less and wind speed of 5 m/s or more. 121

Figure 3.12 Percentage of quality data collected during rain. Filled diamonds represent the subset of data with nadir angle of 10 deg or less and wind speed of 5 m/s or more. 122

Figure 3.13 Percentage of quality data collected relative to ambient light conditions. Filled diamonds represent the subset of data with nadir angle of 10 deg or less and wind speed of 5 m/s or more. 124

Figure 3.14 Directional spectrum for LWG (solid line and circles) and PUV (dashed line and x's) on 9 December 1999 at 1226 EST. 134

Figure 3.15 Directional spectrum for LWG (solid line and circles) and PUV (dashed line and x's) on 11 December 1999 at 1151 EST. 135

Figure 3.16 Comparison between the LWG and PUV peak frequency, f_p. Solid line on figure indicates an exact match while dashed lines on figure indicate one resolution frequency bandwidth. 137

Figure 3.17 Comparison between the LWG and PUV spectral wave height, H_{mo}. Solid line on figure indicates an exact match while dashed lines on figure indicate 10% about the measured spectral wave height. 138

Figure 3.18 Comparison between the LWG and PUV peak direction, θ_p. Solid line on figure indicates an exact match while dashed lines on figure indicate 20 deg about the measured peak direction. 140

Figure 3.19 Deviation in mean wave direction at spectral peak, computed from the LWG and PUV data, as a function of H_{mo}. Percent within indicates percent of measured direction differences within the direction difference given by the x-axis. 141

Figure 3.20 Directional spectrum for LWG (solid line and circles) and 8-m array (dashed line and x's) on 11 December 1999 at 1151 EST. 143

Figure 3.21 Directional spectrum for LWG (solid line and circles) and 8-m array (dashed line and x's) on 12 December 1999 at 1043 EST. 144

Figure 3.22 Comparison between the LWG and 8-m array peak frequency, f_p. Solid line on figure indicates an exact match while dashed lines on figure indicate one resolution frequency bandwidth. 145

Figure 3.23 Comparison between the LWG and 8-m array spectral wave height, H_{mo}. Solid line on figure indicates an exact match while dashed lines on figure indicate 10% about the measured spectral wave height..... 146

Figure 3.24 Comparison between the LWG and 8-m array peak direction, θ_p. Dashed line on the figure represents a linear fit to the peak direction as predicted by Snell's Law..... 147

Figure 3.25 Operational LWG diagram. 151

Figure 4.1 Compact Airborne Spectrographic Imager (CASI) hyperspectral imagery fused with SHOALS data to map bottom type at Key Biscayne, FL in 1994 (from Irish, 2001). 158

ABSTRACT

This study investigates the use of lidar for remote sensing of the coastal environment. Specifically, this study presents a sensor for measuring sea bottom depth using a scanning lidar from an aircraft and a sensor for measuring water waves using lidar from a fixed platform.

This study first presents the U.S. Army Corps of Engineers SHOALS system, the first operational airborne sensor in the United States to use lidar technology to measure bathymetry in the coastal zone. The SHOALS system uses a dual-frequency laser to rapidly collect near-synoptic, high-density bathymetry remotely while meeting accepted international hydrographic survey accuracy standards. Such surveys, collected over the last decade, were used to advance understanding of coastal processes and to improve coastal engineering practices. This study discusses the evolution of airborne lidar bathymetry (ALB) and details the SHOALS system.

Examples and analyses of ALB data collected at a number of coastal areas throughout the United States are presented. Consecutive ALB surveys collected at Moriches Inlet, NY and New Pass, FL are presented and analyzed to help assess these complex coastal environments. Four ALB surveys of shore protection areas are analyzed to assess the value of high-resolution bathymetry for determining sand volumes. ALB surveys collected along Florida's panhandle following landfall of Hurricane Opal are presented to demonstrate emergency response capabilities. Finally, regional-scale surveys in the Gulf of Mexico and Hawaiian Islands are presented to demonstrate the ability for ALB sensors to perform surveys to support regional studies.

While ALB systems rapidly perform high-resolution bathymetry surveys, data collection is limited by water clarity. Typically, ALB sensor depth detection is limited to depths around three times the visible depth. Depth detection is also hindered by the presence of white water, which prohibits the laser beam from penetrating the sea surface.

The second part of this study presents the design and testing of a prototype sensor to expand the application of lidar for long-term measurement of water waves from a fixed platform. The LWG uses four lasers to directly measure water surface elevation at discrete locations from above the water's surface. Therefore, unlike bottom-mounted gages, the surface elevation measurement from the LWG is independent of other hydrodynamic processes. The prototype LWG consists of four rangefinders, where each collects water surface elevation time series at a rate of 10 Hz.

The lidar wave gage (LWG) was field tested at the U.S. Army Corps of Engineers Field Research Facility in North Carolina. During the field test, ground truth data were collected concurrently with the LWG data using a biaxial current and pressure gage (PUV) mounted directly beneath the LWG. Additional ground truth data were available from the existing wave-gaging infrastructure at the testing facility.

This study describes the principles of LWG operation and field experiment set up. This study also investigates the LWG environmental and technical constraints and LWG performance in measuring spectral wave parameters. LWG spectral wave height, peak frequency, and mean direction at the spectral peak were comparable to those measured by the PUV. However, field testing showed that successful LWG operation was limited to small laser beam angles, relative to vertical, and to wind speeds large enough to roughen the sea surface.

Chapter 1

INTRODUCTION

Remote sensing of the coastal environment is an important tool for coastal engineers and researchers. When remote sensing technologies are deployed from an aircraft, they provide the means to rapidly assess dynamic conditions on a regional scale. Remote sensing technologies, when deployed from the air or from a fixed platform, also provide the means to gather quantitative information in difficult to reach, or hazardous locations. These sensors may also be used in areas where the environment is such that in situ measurement is impossible.

Lidar (LIght Detection And Ranging) is one such remote sensing technology. By employing lasers, lidar technology may be used to measure several properties including distance and velocity. In addition, other environmental characteristics may be inferred from the laser's returned energy signal.

The following chapters describe two lidar sensors, both using lidar to directly range distance, for quantifying the coastal environment. The first is a sensor designed to measure water depth in coastal areas by deploying lidar from an aircraft. The second is a sensor designed to measure ocean wave characteristics using lidar from a fixed platform.

1.1 Lidar Depth Measurement

With the advent of lidar mapping technology, near-synoptic, high-resolution, regional-scale mapping of the coastal zone is now realizable (Irish, 2000).

During the last decade, airborne lidar bathymetric and topographic sensors have become fully operational tools used by the terrain mapping community. Today, there are 6 bathymetric lidar sensors and more than 50 topographic lidar sensors in operation throughout the world.

Airborne lidar is an ideal tool for monitoring the coastal zone on regional scales (Wozencraft and Irish, 2000). In contrast to conventional coastal mapping techniques, that include singlebeam and multibeam acoustic techniques combined with wading-depth profile techniques, Airborne Lidar Bathymetry (ALB) and topography sensors rapidly (orders of magnitude faster) collect high-resolution soundings and/or elevations throughout an entire coastal region, or sub-region (Figure 1.1 and Figure 1.2). Such comprehensive data sets allow coastal engineers, scientists, and managers to quantify terrain change and geomorphic feature interaction throughout the entire coastal system.

ALB sensors in operation today have the ability to simultaneously map the nearshore, the adjacent beach, and coastal structures, both above and below the waterline, even in areas where environmental conditions are too dangerous or difficult to use conventional survey techniques. Another major advantage of using ALB is that the speed with which a survey is collected provides a near-synoptic map of bathymetric conditions at a particular time. ALB survey speed is also an advantage when bathymetric conditions must be assessed quickly, such as following a coastal storm or other emergency.

Chapter 2 discusses the evolution of ALB and details the first operational ALB system in the United States. Data collected with this operational ALB have been

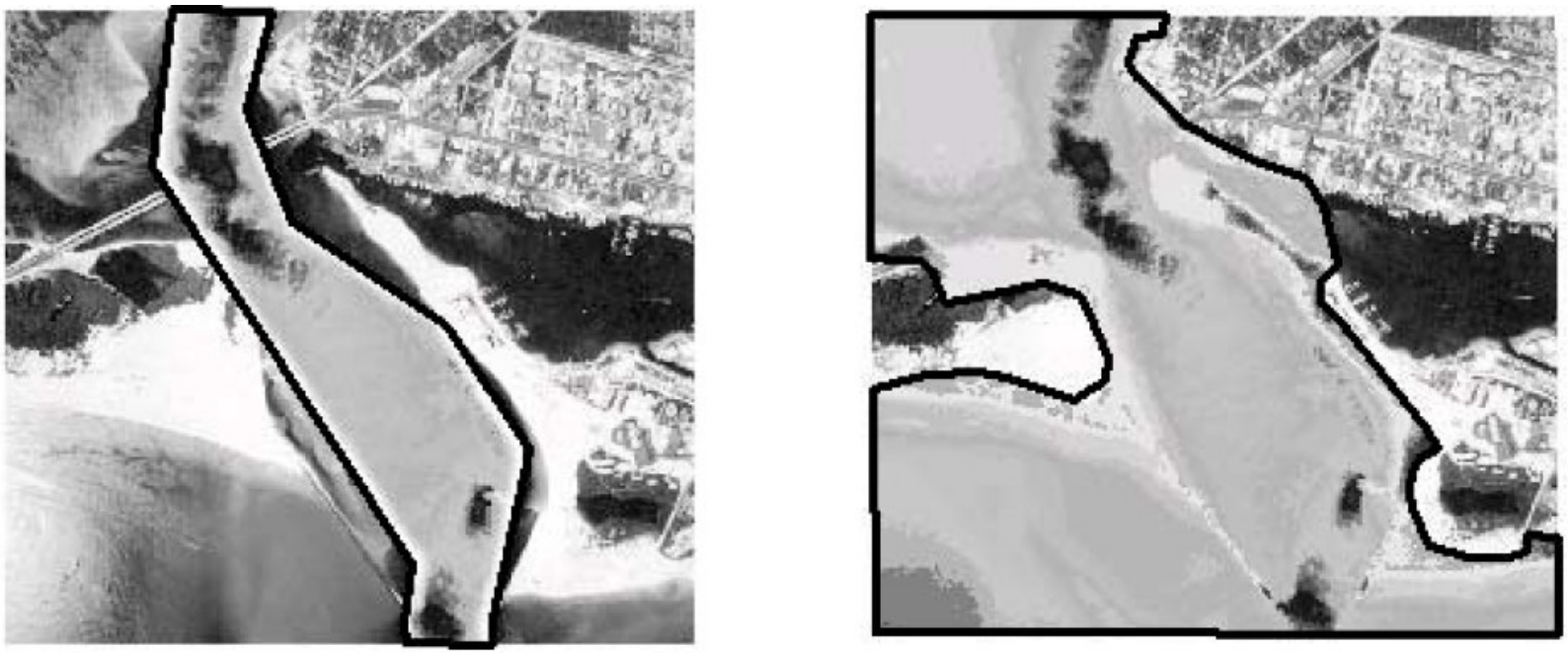

Figure 1.1 **Conventional United States navigation project survey plan (a) versus airborne lidar survey plan (b). Location is East Pass, FL (from Irish, 2000).**

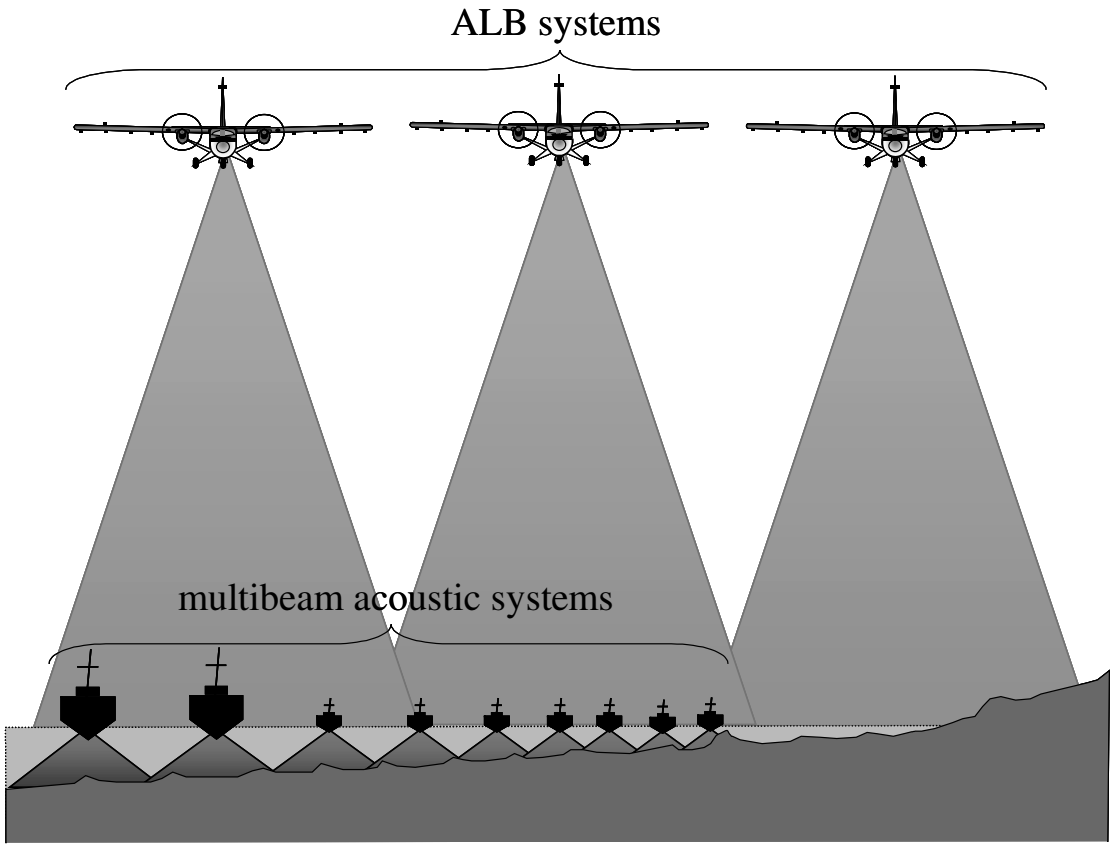

Figure 1.2 ALB system survey capabilities versus boat-mounted multibeam acoustic system survey capabilities (modified from Irish, 2000).

used extensively over the last decade to advance our understanding of coastal processes and our ability to improve coastal engineering practices. Several such examples are presented in Chapter 2.

1.2 Lidar Wave Measurement

Accurate, meaningful measurement of directional wave field evolution within the nearshore regime, particularly at coastal navigation projects, may be difficult to obtain with present in situ and remote sensing technology. Such phenomena as trapped waves, wave breaking (both depth and current induced), and wave-current interaction are not well understood at present largely because of the inability to accurately quantify these processes in nature. Oftentimes, bottom-mounted gages are not easily deployed or may themselves be hazards to navigation, and the performance of pressure gages for measuring waves is limited in the presence of strong currents. Further, surface-piercing gages may be destroyed in a dynamic coastal environment. Due to the severity of the physical environment and the difficulty of properly characterizing the changes that take place within the spatial wave field, new wave measurement technologies are needed to augment existing in situ methods.

Remote sensing technologies may prove a viable solution to measuring wave characteristics in areas where conventional measurement methods are not possible. Furthermore, remote sensing technologies show promise for accurately measuring the temporal evolution of wave characteristics over an entire region. Complex nearshore processes, such as those at a tidal inlet, may be better quantified by combining in situ wave measurement methods with new remote sensing technologies that operate from fixed platforms (Figure 1.3).

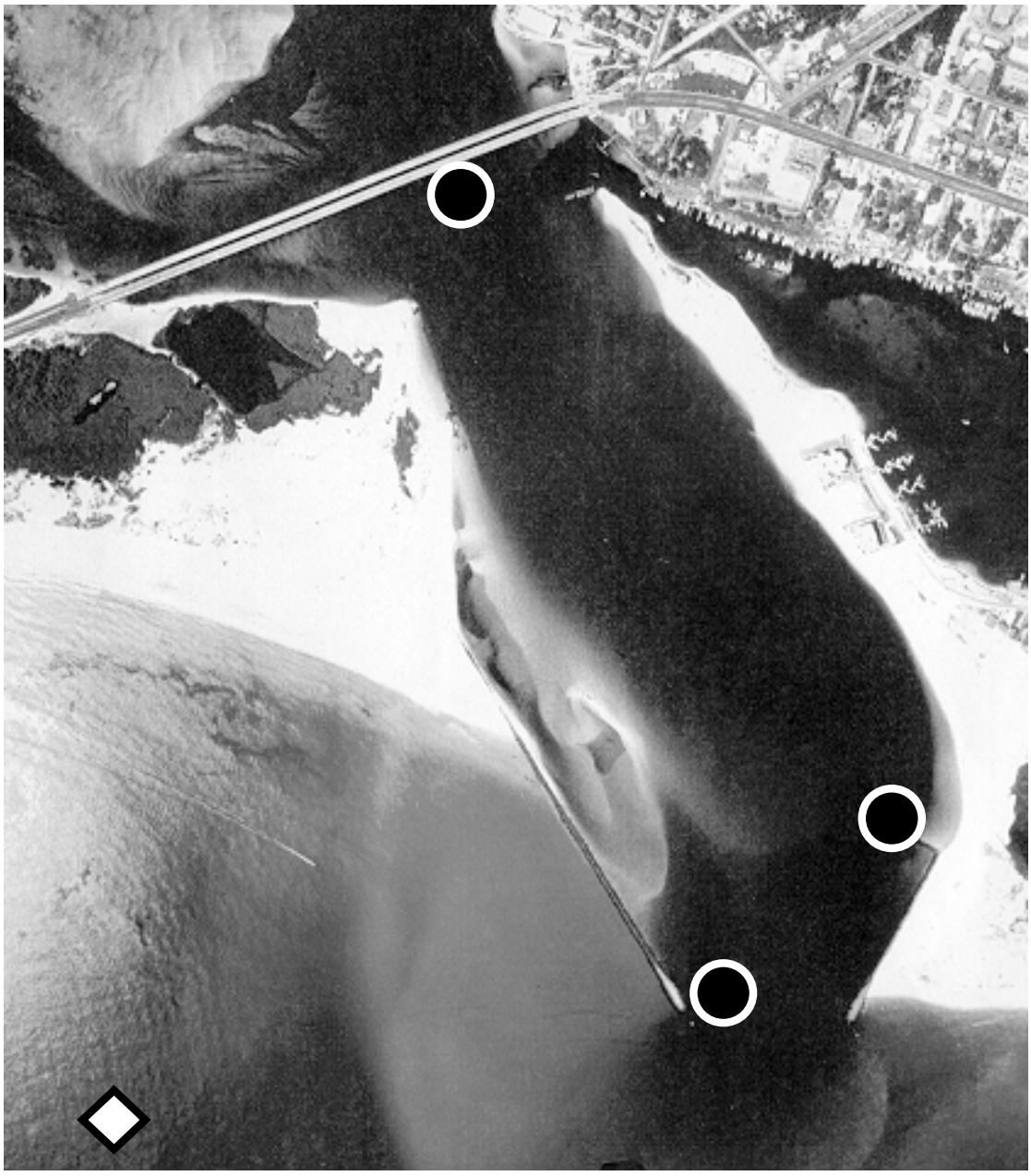

Figure 1.3 Combined in situ (diamond) and remote (circles) measurement scheme at a navigation project (East Pass, FL; from Irish et al., 2001).

Chapter 3 discusses the design and testing of a prototype wave gage that uses lidar to actively measure ocean waves from a fixed platform (Irish et al., submitted). Following a discussion of ocean wave remote sensing methods developed to date, the Lidar Wave Gage (LWG) is described. Finally, field test results are presented, and LWG performance is assessed.

Chapter 2

AIRBORNE LIDAR FOR SEA BOTTOM MAPPING

This chapter describes Airborne Lidar Bathymetry (ALB) technology and its application for coastal engineering and research. The history of ALB development and the physical principles upon which ALB is based are presented in the first two sections of this chapter. Chapter 2.3 then fully describes the U.S. Army Corps of Engineers (USACE) Scanning Hydrographic Operational Airborne Lidar Survey (SHOALS) system, the first operational ALB in the United States The remainder of this chapter is dedicated to presenting examples of how ALB is helping to advance our understanding of the coastal environment and improving coastal engineering practice by presenting several data sets and case studies using SHOALS bathymetry.

2.1 History of Airborne Lidar Bathymetry–A Literature Review

Guenther (in press), Guenther et al. (2000), and Guenther (1985) provided complete reviews of the history and evolution of ALB. Chapter 2.1 follows these reviews and adds additional detail on development of landmark sensors and predecessors to the SHOALS system.

2.1.1 Proof-of-Concept Testing

Pioneering efforts by Ott (1965) and Sorenson et al. (1966) demonstrated that lasers onboard an aircraft could be used to locate submarines. Following these demonstrations, Sorenson (1966) proposed an airborne bathymeter system that would

employ laser-ranging methods. Syracuse University Research Center was the first to conduct field tests to prove that an airborne, pulsed laser could indeed be used to measure nearshore water depths (Hickman and Hogg, 1969).

2.1.2 First-Generation Airborne Lidar Bathymetry Systems

Hickman and Hogg's (1969) success was shortly followed by development and testing of several first-generation ALB systems by the U.S. Navy (Cunningham, 1972 and Witt et al., 1976). Among these first-generation ALB systems was the U.S. Naval Oceanographic Office's Pulsed Light Airborne Depth Sounder (PLADS), which was reported to have collected laser depth measurements as deep as 70 m in the clear waters off the Florida Keys. In 1975, the National Aeronautics and Space Administration (NASA) also reported successful development and testing of a first-generation ALB sensor (Kim et al., 1975).

While ALB sensor development and testing was being conducted here in the United States, governments in Canada, Sweden, the Soviet Union, and Australia were developing and testing their own experimental lidar bathymeter systems. Ivanov et al. (1972) reported successful ship-borne lidar bathymeter testing in the Soviet Union, and shortly thereafter, Carswell and Sizgoric (1974) reported similar success in Canada.

An effort to advance sensor design was co-sponsored in the United States by the Office of Naval Research, the National Oceanographic and Atmospheric Administration (NOAA), and the U.S. Geological Survey (USGS) (Hickman et al., 1972 and Hickman et al., 1974). As part of this effort, Sparcom, Inc., using a pulsed laser in a large tank, conducted a series laboratory tests to further understanding of light transport mechanisms.

Shortly thereafter, experimental ALB systems were developed and field tested in the United States by NASA and the Naval Air Development Center, in Australia by the Australian Department of Defence, and in Canada by the Canada Centre for Remote Sensing (CCRS) (Kim et al., 1975; Abbot and Penny, 1975; Ferguson, 1975; Shannon, 1975; and Witt et al., 1976). In the late 1970s, the Canadian government also reported successful trials with a first-generation airborne system (O'Neil et al., 1978).

2.1.3 Second-Generation Airborne Lidar Bathymetry Systems

These early forays into the application of lidar to measure water depths paved the way for second-generation system development. The following two sections describe the landmark system developed in the United States, the Airborne Oceanographic Lidar (AOL), and other international activities.

2.1.3.1 The Airborne Oceanographic Lidar System

Following the success of these first-generation ALB systems, NASA sponsored development of a second-generation ALB system, the AOL. This landmark system was successfully field tested in 1977 jointly by NASA and NOAA (Guenther and Goodman, 1978; Guenther et al., 1979; and Hoge et al., 1980).

The AOL improves over first-generation systems in three important ways. First, the AOL was the first ALB system to record the full time history of returned laser energy, beginning at the sea surface and terminating at the sea bottom (lidar waveform). Second, the AOL system made swath ALB mapping possible by directing the laser pulses across the flight path using a scanner. Finally, significant advancements were made for post-processing of recorded lidar waveforms.

The AOL system uses a neon laser operating at 540.1 nm and pulsing at rates as high as 400 Hz (Hoge et al., 1980). The laser pulses are directed toward the sea surface by a conical type scanner. The AOL receiver records the laser energy returned by the sea surface, throughout the water column, and the sea bottom. A Photo-Multiplier Tube (PMT) was employed to amplify the laser return from the sea bottom.

The 1977 AOL system field tests were conducted from NASA's Wallops Island, VA facility in both the coastal waters of the Atlantic Ocean and the estuarine waters of Chesapeake Bay. Objectives of this field experiment were to quantify the AOL system's performance over a range of water depths, environmental conditions (e.g. water clarity), and sensor settings (e.g. laser beam angle relative to vertical).

Ground truth water depth measurements were obtained by a NOAA shipboard sonar system. Hoge et al. (1980) reported that the root-mean-square (RMS) error in lidar depths, relative to the NOAA sonar depths, ranged from 7 cm to 20 cm. During field testing, the AOL system demonstrated capabilities to accurately measure water depths as deep as 10 m in the Atlantic Ocean. AOL depth measurement capabilities were more limited, just under 5 m, in the more turbid waters of Chesapeake Bay.

A post-processing computer program to thoroughly analyze the recorded lidar waveforms was developed by Borman (1978) and improved upon by Guenther and Borman (1981). This program contained sophisticated algorithms to perform system calibration, automated depth extraction, and water surface wave correction. These fundamental algorithms make up the basis for most ALB post-processing routines in use today.

2.1.3.2 Other Efforts

Concurrent with design and testing of the AOL system, several other second-generation systems were developed. Clegg and Penny (1978) described a second-generation ALB system developed for the Australian government: WRELADS I. Shortly thereafter, Abbot et al. (1978) reported successful test results with WRELADS I.

Balandin and Volodarskiy (1979) reported promising results from their development and testing of a second-generation system in the Soviet Union. O'Neil (1981) also reported successful design and testing of a second-generation system by the CCRS. This Canadian system, modified to include a scanner, was also successfully field tested in Sweden, in the waters of the Baltic Sea, by the Swedish Defence Research Institute (Steinvall et al., 1981).

2.1.4 Third-Generation Airborne Lidar Bathymetry Systems

With the technological breakthroughs that came along with second-generation system testing and data analysis, development of third-generation ALB systems were quick to follow in the 1980s.

2.1.4.1 The LARSEN-500 System

In Canada, Optech, Inc. developed the LARSEN-500, a third-generation system developed for the CCRS (Anderson et al., 1983 and Banic et al., 1986). Following successful field trials in Canada's Northern Territories, the LARSEN-500 became the first ALB system to move from experimental use only to full operational use (Casey, 1984 and Casey et al., 1985). This operational ALB system successfully completed hydrographic surveys in the Great Lakes, the St. Lawrence River, and

coastal Canada. The following summarizes operational characteristics of the LARSEN-500:

- Sounding rate = 20 Hz
- Depth penetration = 40 m
- Accuracy: meets International Hydrographic Office (IHO) standards
- Positioning: microwave
- Scanner: fixed
- Post-flight processing speed: 20 hours for each hour of in-flight data collected
- Onboard system size = 3 m^3

Depths collected in 1988 with the LARSEN-500 were the first lidar depths ever to be used in the development of a nautical chart (Sizgoric, personal communications).

Following the success of LARSEN-500 operations, in the late 1980s, the Swedish Defence Agency and the U.S. Defense Advanced Research Projects Agency each commissioned the construction of operational systems by Optech, Inc.: the FLASH and ALARMS systems, respectively. Alexsson et al. (1990) and Steinvall et al. (1992) discussed the FLASH system.

2.1.4.2 Other Efforts

Abbot (1981) and Penny (1981) reported successful design and testing of the Australian's third-generation ALB, WRELADS II. In the Soviet Union and in China, several research ALB systems were also designed and tested (Bunkin et al., 1984; Feigels and Kopilevich, 1993; and Liu, 1990).

2.1.5 Fourth-Generation Airborne Lidar Bathymetry Systems

The early 1990s saw the introduction of several fully operational ALB sensors. Among them was the USACE SHOALS system. The SHOALS program was initiated in 1988 (Pope and Lillycrop, 1988). Unlike ALB sensor development to date, which focused on small object detection and nautical charting, the SHOALS system was the first system proposed for use specifically for coastal engineering purposes. The USACE motivation for designing and acquiring an ALB system was to augment survey capabilities at USACE navigation and shore protection projects that cover the dynamic coastal zone. Optech, Inc. undertook SHOALS development and built upon lessons learned and discoveries made during the operation of the LARSEN-500 system.

Around the same time that the USACE embarked on design of the SHOALS system, the Swedish government sought to acquire an operational ALB system. They too partnered with Optech, Inc. Consequently, the SHOALS system design and the Swedish system design, HAWKEYE, merged. Steinvall et al. (1994) and Koppari et al. (1994) provided details on the Swedish HAWKEYE system's design and performance. Construction of both the SHOALS and HAWKEYE systems was completed in the middle of the 1990s. Both systems originally operated from helicopters.

The SHOALS system became the first operational ALB system in the United States in 1994. A full discussion of the SHOALS system is given in Chapter 2.3 below.

2.1.5.1 The LADS System

Shortly after the WRELADS II system was successfully tested, the Royal Australian Navy commissioned the design and construction of Australia's first operational ALB, the Laser Airborne Depth Sounder (LADS). Compton and Hudson (1988) and Penny et al. (1989) reported on LADS sensor design. LADS became the first operational ALB system in Australia in 1988 (Setter and Willis, 1994 and Nairn, 1994).

2.2 Airborne Lidar Bathymetry Principles

An ALB sensor uses lidar technology to directly measure water depths. All ALB sensors in operation today use a laser transmitter/receiver (transceiver) mounted on an aircraft (Guenther et al., 1996). The transceiver transmits a laser pulse that travels to the air-water interface where a portion of this energy reflects back to the transceiver (surface return, Figure 2.1). The remaining energy propagates through the water column and reflects off the sea bottom (bottom return). The water depth comes directly from the time lapse between the surface return and the bottom return. Typically, an ALB sensor collects through depths equal to three times the Secchi (visible) depth. In optically clear water, ALB sensors have successfully measured to depths of 70 m (Sinclair, 1999).

In addition, each sounding is appropriately corrected for water level fluctuations using either vertical aircraft positioning from GPS or by referencing the lidar measurements of water surface location with water level gage measurements. Because ALB data collection and processing is not routine and can oftentimes be complex, the following sections detail the physical concepts governing lidar bathymetry. A thorough understanding of lidar principles is necessary to accurately

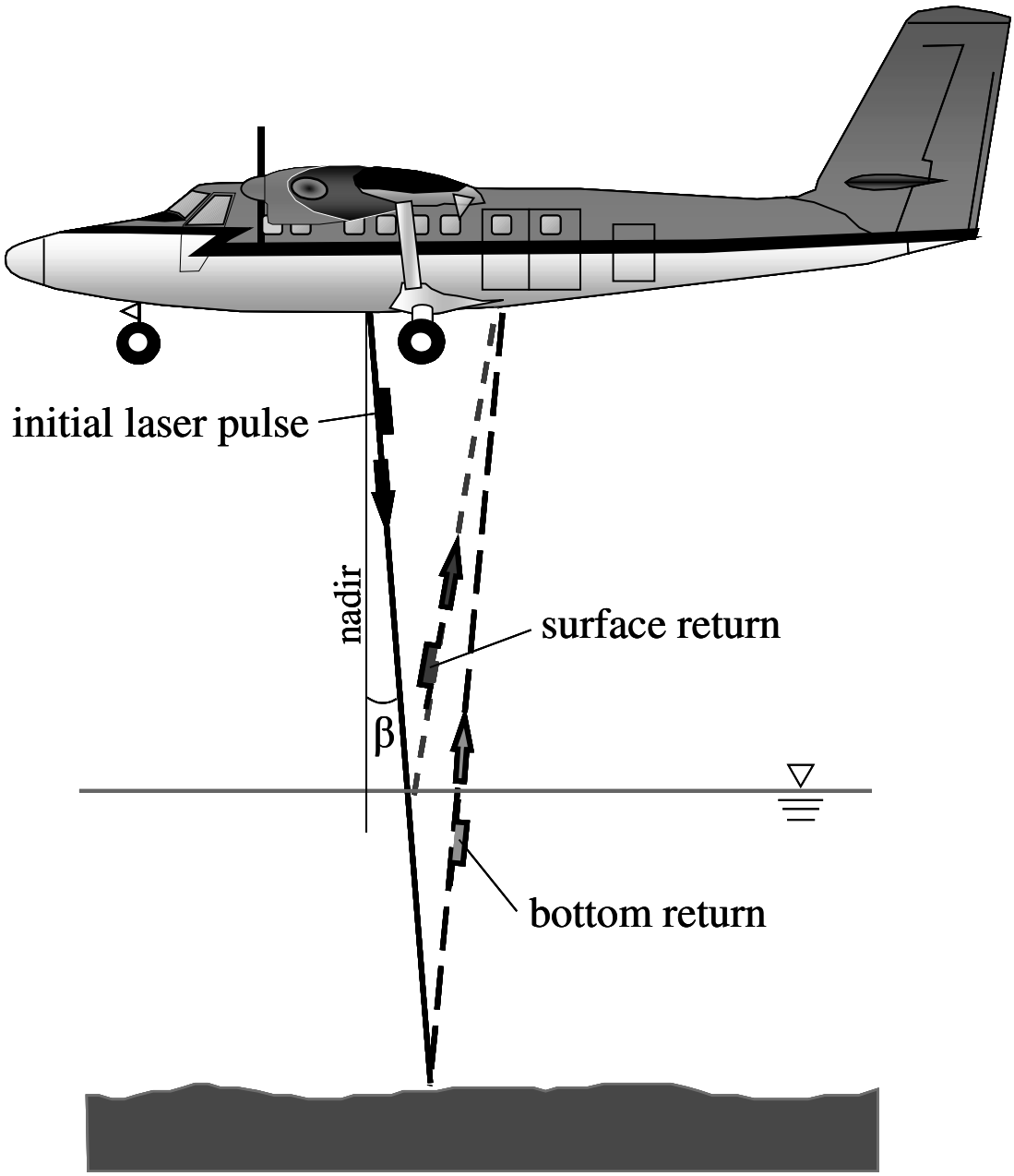

Figure 2.1 ALB operating principle (modified from Irish, 2000).

determine water depths from collected lidar signals. These principles were used extensively in this study to analyze collected lidar data to extract depths for the surveys presented in Chapters 2.4 through 2.7.

2.2.1 Lidar Ranging

Wehr and Lohr (1999) and Baltsavias (1999) provided a complete description of the principles of lidar ranging. Fundamentally, pulsed lidar measures the distance, or range (R), to an object by measuring the round-trip time required, t, for the laser pulse to travel from the lidar transceiver to the object and back (Figure 2.1):

$$R = \frac{c\ t}{2} \tag{2.1}$$

where c is the speed of light, about 3.00×10^8 m/s in air and 2.25×10^8 m/s in water. Baltsavias (1999) stated that the range resolution, ΔR, for a pulsed lidar system is:

$$\Delta R = \frac{c\ \Delta t}{2} \tag{2.2}$$

where Δt is the return signal sampling interval, or time resolution, and is typically reported in nanoseconds.

Assuming the receiver does not have a time limit for recording the returned laser power, the maximum theoretical unambiguous ranging distance, R_{max}, for a pulsed laser is determined by the laser pulse rate (Baltsavias, 1999). Wehr and Lohr (1999) provide the following definition of R_{max}:

$$R_{\max} = \frac{c\ t_{L\max}}{2} \tag{2.3}$$

where t_{Lmax} is typically taken as the laser pulse rate, that is the time between the initiation of one laser pulse and the initiation of the next laser pulse (Figure 2.2).

In practical application of lidar technology for bathymetric mapping, laser energy is lost due to refraction, scattering, and absorption at the water surface, sea bottom, and as the pulse travels through the water column (Figure 2.3). The combination of these effects limits the strength of the bottom return and therefore limits the maximum detectable depth. Optical water clarity is the most limiting factor for ALB depth detection.

2.2.2 Water Depth Measurement

Guenther et al. (2000) and Guenther (in press) present the physical basis upon which ALB sensors are based. This section provides a summary of these concepts.

In general, an ALB sensor uses a pulsed laser transmitter with two light frequencies: one in the blue-green range, around 532 nm, and one in the infrared range, around 1064 nm (Guenther, 1985; Guenther and Goodman, 1978; Hoge et al., 1980; and Guenther and Thomas, 1983). The infrared wavelength is used to determine the sea surface while the blue-green wavelength is used primarily to determine the sea bottom. In ALB system design, it is important to measure both the sea surface and sea bottom in order to accurately measure bottom depth because the speed of light in air and in water differs enough to introduce measurable errors if a uniform speed is assumed.

Infrared laser wavelengths are typical for airborne lidar topographic mapping, and these wavelengths successfully measure the ocean surface. However,

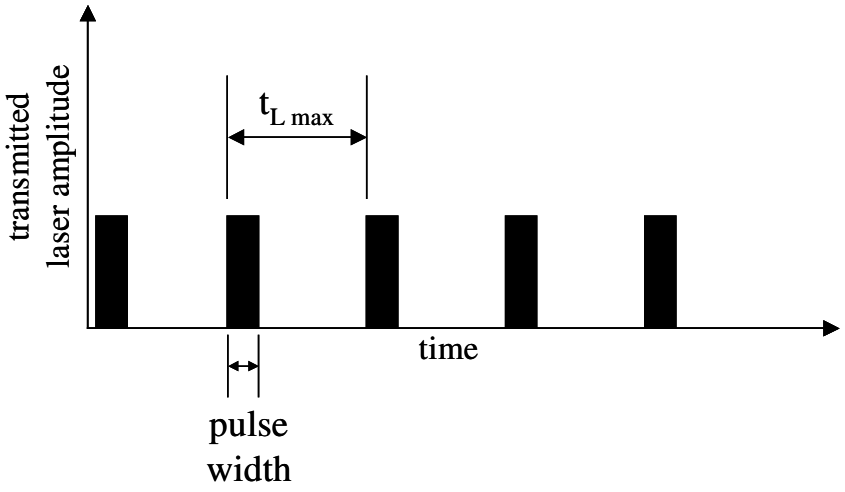

Figure 2.2 Definition of laser pulse width and maximum traveling time, $t_{L\ max}$ (modified from Wehr and Lohr, 1999).

the ability for infrared energy to penetrate the water column is limited to depths of a decimeter or so.

ALB sensors use the infrared laser to determine the distance to the water surface in two ways. The first is by directly recording the energy received at the same wavelength as the transmitted infrared wavelength. This signal return is generally strong. However, false returns are possible from the presence of sea spray, birds, low-lying mist, and any other physical obstructions between the aircraft and the water surface. As mentioned above, the infrared laser energy penetrates a small way into the water column. Once the infrared energy enters the water, it interacts with water molecules to generate Raman backscatter at a frequency of 645 nm (Walrafen, 1967). This Raman backscatter may be used as second measurement of the sea surface elevation. While the Raman energy return is generally weaker than the direct infrared

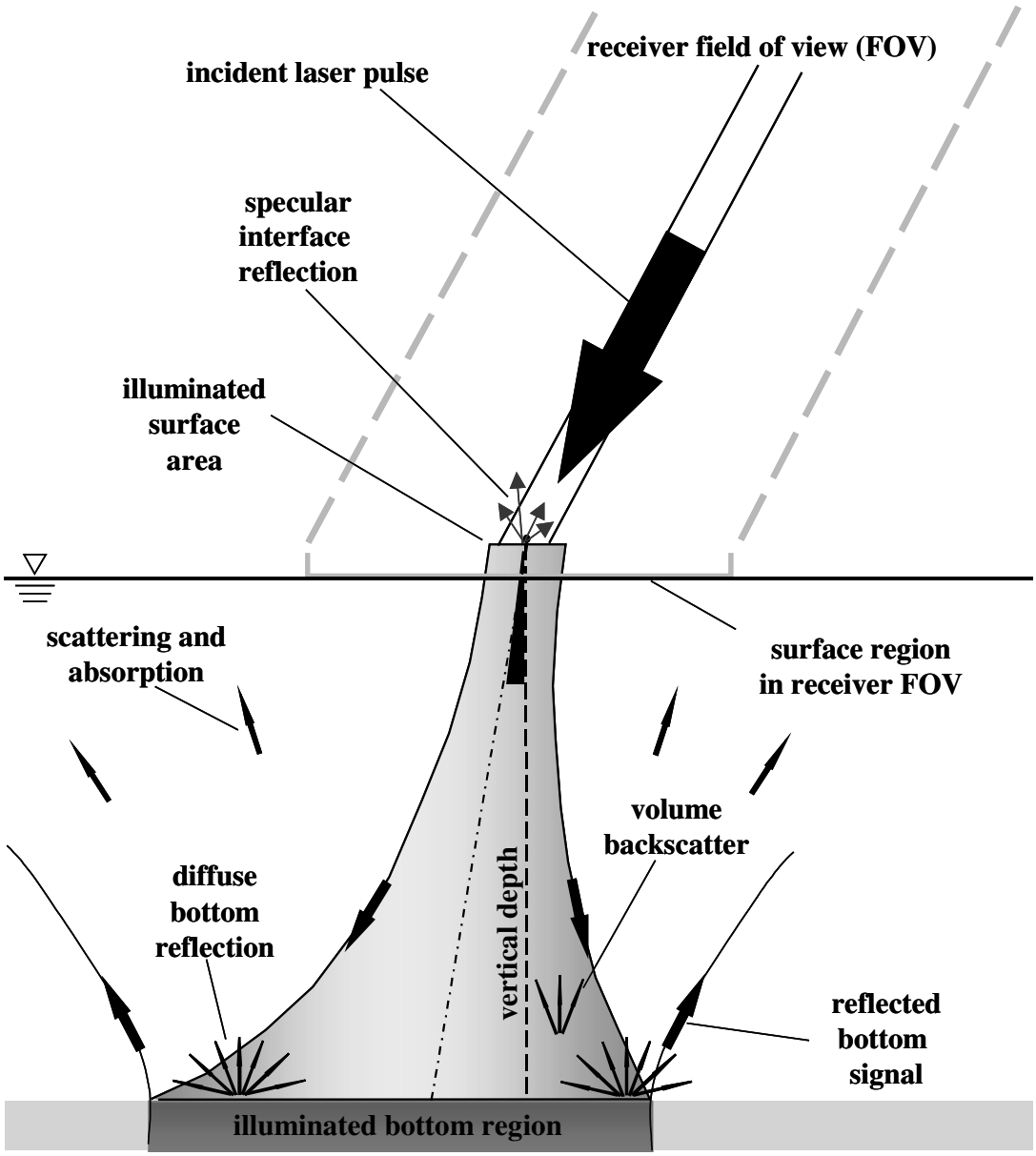

Figure 2.3 Water column and interface effects on system performance (modified from Irish, 2000).

return, it is unambiguous and is not affected by obstructions between the sea surface and the aircraft.

Jerlov (1976) determined that blue-green laser frequencies are optimum for penetrating ocean water with the least amount of energy attenuation. Bottom depth is determined from the blue-green laser return waveform, laser energy return versus time (Figure 2.4). There are three principle components in the blue-green laser waveform: sea surface return, volume backscatter return, and sea bottom return. The sea surface return marks the partial reflection of blue-green laser energy back to the receiver. The blue-green laser's sea surface return strength varies significantly, over several orders of magnitude, depending on wind and ocean wave conditions at the time of data collection.

The second principle component of the waveform is the volume backscatter return. Volume backscatter results from particulate matter in the water column. Consequently, the volume backscatter is directly related to the water clarity and the strength of the volume backscatter return is nearly constant for a particular data collection operation. The volume backscatter increases as water turbidity increases, and a high level of volume backscatter may make sea bottom detection impossible. This is the most limiting factor for lidar bathymetry detection.

Finally, the third principle waveform component is the sea bottom return. As mentioned in Chapter 2.2.1, the sea bottom return strength is strongly dependent on the sea bottom's reflective properties and optical water clarity. In simplified form, the water depth, d, is then determined by employing Equation 2.1:

$$d = \frac{c_{water}}{2} \left(t_{bottom} - t_{surface}\right) \cos\beta \qquad (2.4)$$

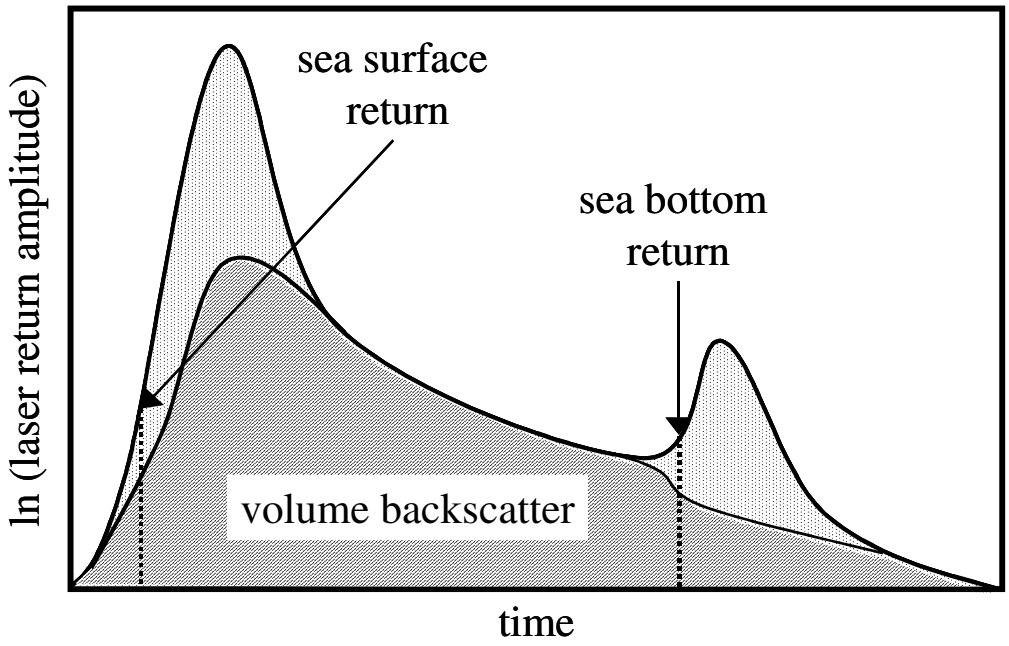

Figure 2.4 Idealized blue-green laser waveform showing the principle return signal components (modified from Guenther et al., 2000).

where:

c_{water} is the speed of light in water, based on the expected salinity in the survey area (Guenther et al., 2000)

t_{bottom} is the round-trip travel time between the aircraft and the sea bottom, calculated from the blue-green signal

$t_{surface}$ is the round-trip travel time between the aircraft and the sea surface, calculated from either the infrared or Raman signal

β is the laser beam angle (also termed nadir angle), or the angle at which the laser beam travels. Laser beam angle is measured relative to nadir, or vertical (Figure 2.1)

Guenther and Thomas (1983) have shown that the ranging times, $t_{surface}$ and t_{bottom}, should be selected at the half-peak amplitude on the waveform to achieve the most accurate depth measurement (see Figure 2.4). For ALB, the laser beam angle, β, is small, such that cos β is close to one. For example, a laser beam angle of 20 deg translates to a cosine equal to 0.94.

While detection of the sea surface is possible with a blue-green laser, it should be noted that there are limitations making it impractical to operate an ALB sensor with only a blue-green wavelength (Guenther et al., 2000). First, if the blue-green sea surface return is weaker than the volume backscatter return, the volume backscatter return may be falsely identified as the sea surface return. Secondly, Guenther et al. (2000) stated that mixing of volume backscatter and the blue-green surface return results in a measured laser travel time that represents an indeterminate distance under the water surface and is, therefore, in error. Finally, the blue-green surface return may merge with strong sea bottom returns in shallow water. Thus, it is necessary to record the sea surface elevation with either the infrared or Raman wavelengths.

2.2.3 Horizontal and Vertical Positioning

ALB systems in use today employ laser scanners to position laser footprints both across and along the flight path. The three-dimensional positioning of each footprint relative to the aircraft is found from the lidar ranging distance and the geometry related to the specific scanner's setup, including laser beam angle and the scan rate, defined as the number of scans per second. In addition, the aircraft's roll, pitch, and heading must be known and corrections made accordingly. Inertial

Navigation Systems (INS), which use gyroscopes and accelerometers to determine direction and acceleration, are used for this purpose.

All ALB systems use Global Positioning System (GPS) for horizontal positioning. In addition, nearly all systems today use Kinematic GPS (KGPS) to also provide vertical aircraft position. However, it should be noted that ALB systems typically operated with Differential GPS (DGPS), providing only horizontal positioning, through the 1990s. For surveys collected with DGPS, the vertical position was determined by relating the sea surface elevation measured by the lidar sensor with recorded tide levels. This method follows the standard methods employed during conventional hydrographic surveys.

The rate at which GPS positions are recorded is typically less than the lidar collection rate. Consequently, horizontal and vertical position must be inferred for each laser range by using the KGPS positions, aircraft altitude, and aircraft speed.

2.3 The SHOALS System

The SHOALS system was designed and tested by the USACE in the early 1990s, and since that time has been used successfully to collect bathymetry for coastal engineering and nautical charting purposes throughout the United States and abroad (Irish and Lillycrop, 1999 and Irish, 2000). The SHOALS ALB system operates from both fixed-wing and rotary-wing platforms (Figure 2.5a; Guenther et al., 2000; Guenther et al., 1996; Irish, 2000; and Irish and Lillycrop, 1999). Table 2.1 summarizes the SHOALS system specifications. Inside the aircraft are the laser transceiver, operator interface consoles, and pilot guidance system (Figure 2.5b).

ALB data for this study were collected using the SHOALS system. Specifically, the SHOALS transceiver and post-flight data processing software were

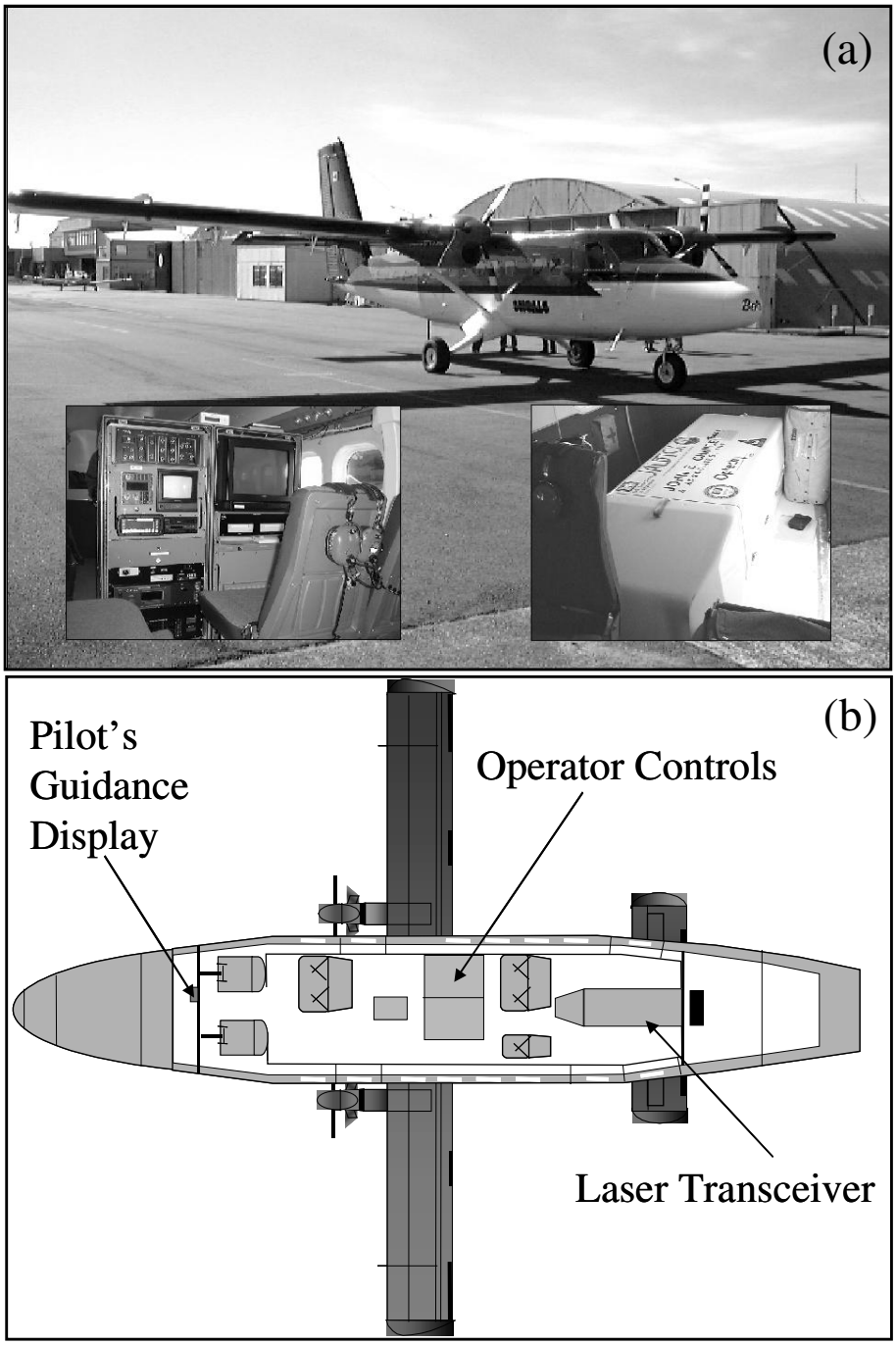

Figure 2.5 (a) SHOALS system mounted on a Twin Otter and (b) layout of SHOALS system inside Twin Otter (from Irish, 2000).

Table 2.1 Summary of SHOALS system specifications.

Laser type	Nd:YAG infrared: 15mJ at 1064 nm Blue-green: 5 mJ at 532 nm
Laser pulse rate	400 Hz
Laser pulse width	6 ns (governed by eye safety requirements and surface return optimization)
Scanner type	Flat mirror, dual axis, programmable
Scan rate	Variable
Scan pattern	Variable (nominal arc ahead of aircraft 20 deg from nadir)
Laser receiver	20-cm catadioptric Cassegrain telescope with five-way splitter
Avalanche photodiode detectors	1064 nm (2) 532 nm (1, shallow water and topography) 645 nm (1)
PMT detector	532 nm (deep water)
Return signal sampling interval	1 GHz
Post-flight processing speed	2 hours for each hour of in-flight data collected
On-board system size	2 m^3

used in this study. Since these SHOALS components are not standard and their use is complex, they are detailed in the following sections.

2.3.1 SHOALS Transceiver

The SHOALS system's laser transceiver uses a Cutting Edge Optronics diode-pumped Neodymium: Yttrium-Aluminum-Garnet (Nd:YAG) laser with a frequency doubler. It operates at two energy frequencies: a blue-green frequency (532 nm) and an infrared frequency (1064 nm). The transmitted pulse width is 6 ns and was selected to optimize surface return detection and to meet eye safety requirements. The transceiver records laser energy return time series (waveforms) with five receivers. Figure 2.6 illustrates a typical SHOALS post-processing window, displaying four lidar waveforms. Two receivers record the infrared energy reflected from the water surface (surface return) and two collect the blue-green energy reflected from the sea bottom (bottom return, Figure 2.1). A fifth receiver records Raman energy, at 645 nm. All waveforms are recorded in-flight to Exabyte tape in raw form, and depths are extracted during post-flight processing.

The two blue-green waveforms directly range the sea bottom for shallow, 0 m to 10 m, and deeper, 10 m to 60 m, depths. An avalanche photodiode detector is used to record the shallow-water waveform, while a PMT detector is used to record the deep-water waveform. An Analytex 1-GHz digitizer is used to digitize all return waveforms simultaneously.

To avoid problems associated with air-water interface detection, as discussed in Chapter 2.2.2, SHOALS uses two waveforms to determine the sea surface accurately. Prioritized by order of use, these are the Raman then infrared channels.

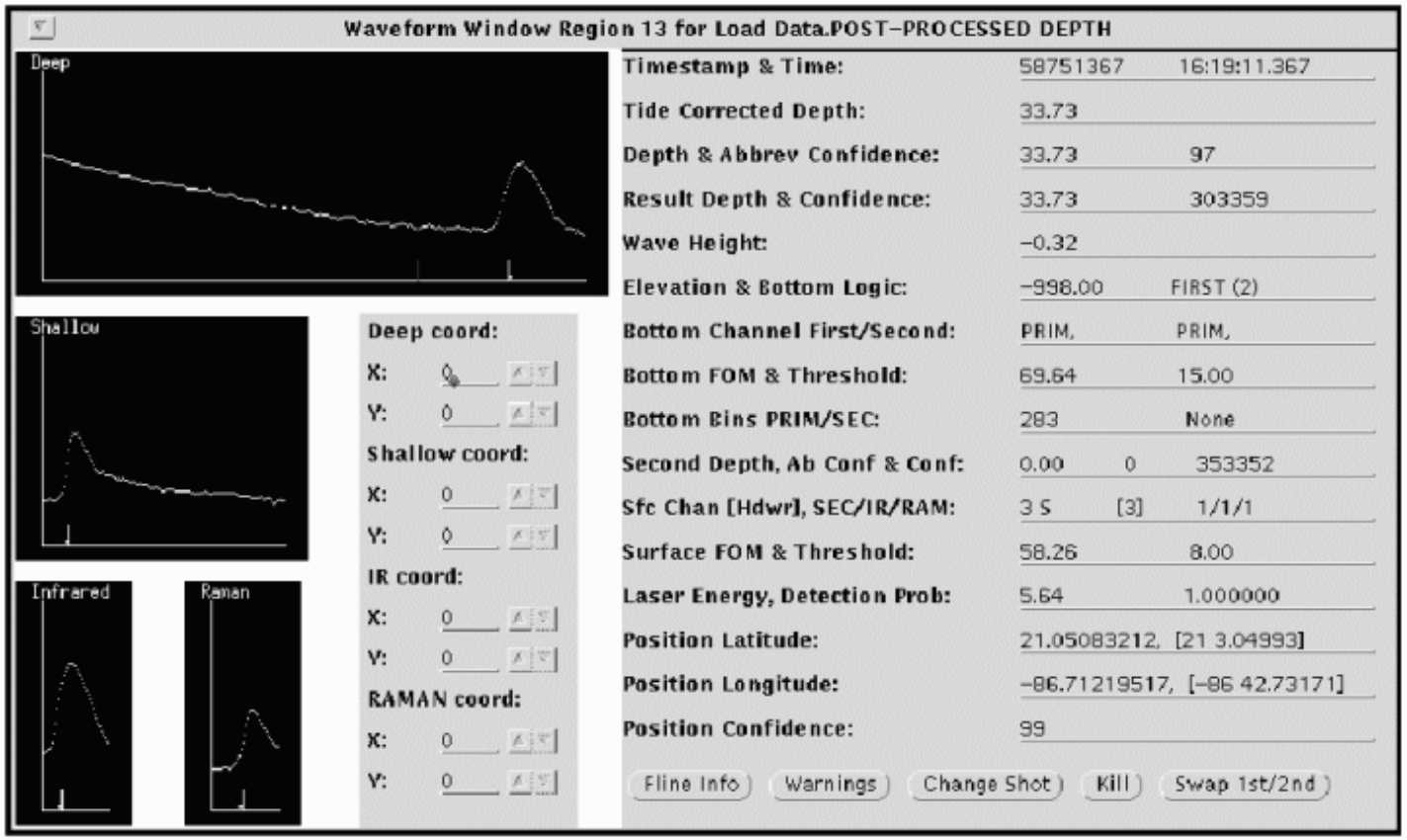

Figure 2.6 **SHOALS post-processing window showing the lidar waveforms collected for each laser pulse.**

The second infrared channel is used in conjunction with the first to discriminate between land and water returns.

During data collection for this study, the need to collect adjacent upland topography along with the ALB was identified. As such, the SHOALS system was modified in 1996 to include topographic capabilities for measurement on dry land. Consequently, the blue-green waveforms are also used to directly range topographic elevations.

The SHOALS laser pulses at a rate of 400 Hz, providing 400 individual range measurements per second. A Saab Instruments programmable scanner mounted with the transceiver positions each laser pulse to provide uniform sounding and elevation spacing on the earth's surface (Figure 2.7). The SHOALS scanner uses a gyro-stabilized mirror to actively compensate for roll and pitch. The scanner also ensures that the laser beam angle, relative to nadir, remains nearly constant at 20 degrees.

For coastal monitoring surveys, SHOALS typically collects data from an altitude of 400 m, resulting in a scanner swath width of 220 m. Along with an aircraft speed of 30 m/s, this results in an individual sounding or elevation measurement every 4 m and a survey speed of 25 km^2 per hour. Table 2.2 gives SHOALS operation and performance characteristics.

2.3.2 SHOALS Horizontal and Vertical Positioning

SHOALS receives its positioning from GPS in either differential or kinematic mode. With DGPS, U.S. Coast Guard beacons and the OMNISTAR satellite system provide horizontal positioning of the aircraft. Accurate vertical positioning for each measurement is then obtained by correlating the lidar surface

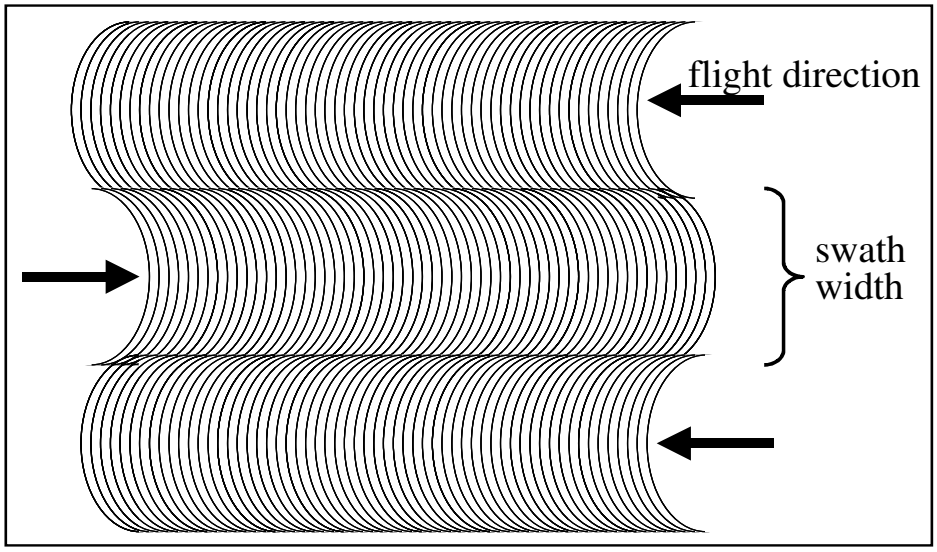

Figure 2.7 SHOALS scan and flight patterns (from Irish, 2000).

Table 2.2 SHOALS operation and performance characteristics.

Maximum depth	to 60 m
Vertical accuracy	± 15 cm
Horizontal:	
DGPS	± 3 m
KGPS	± 1 m
Sounding density	4-m grid (variable)
Operating altitude	400 m (variable)
Scan swath width	220 m (variable)
Operating speed	30 to 60 m/s

return with independent water level measurements. In contrast, KGPS provides both horizontal and vertical aircraft positioning accurately, thus the full three-dimensional positioning for each measurement is independent of supporting water level measurements. SHOALS vertical positioning accuracy is ±15 cm and horizontal positioning accuracy is ±3 m and ±1 m with DGPS and KGPS, respectively (Irish et al., 2000a; Pope et al., 1997; and Riley, 1995). A Litton LTN-90 INS mounted with the laser optics measures aircraft roll and pitch.

SHOALS typically employed DGPS through the 1990s. More recently, KGPS and DGPS were used. While KGPS is preferred for increased survey accuracy, the increased costs for using it oftentimes precludes its use.

2.3.3 Supplemental Video

The SHOALS system also collects a directly downward-looking, geo-referenced video concurrently with the lidar measurements. In addition to offering a visual record of the survey area, the video is frequently used to position coastal features such as navigation aids, piers, and other objects of interest. The video recorder also serves as an auxiliary check for anomalous data discovered during post-flight processing.

2.3.4 Post-Flight Processing

Post-flight processing uses a depth-extraction algorithm developed by the NOAA National Ocean Service (Thomas and Guenther, 1990; Lillycrop et al., 1993; and Guenther and Mesick, 1988). The system software serves two functions: automated processing and manual processing. In automated processing, each sounding's five waveforms are analyzed and a depth extracted. Automated processing

also makes surface wave and water level corrections as needed. Manual processing allows the hydrographer to interrogate data sounding by sounding. When the automated processor flags a questionable sounding, the hydrographer accesses the waveform window display (Figure 2.6). Here, four recorded waveforms are visually displayed along with other pertinent sounding information such as selected surface detection channel, selected bottom detection channel, aircraft altitude, and depth and position confidence. From this information, the hydrographer makes an informed decision about that sounding's integrity. Once post-flight processing is complete, the data are written to an ASCII text file with latitude, longitude, and depth for each qualified sounding.

2.3.5 SHOALS Performance

The SHOALS system was thoroughly field tested in the Gulf of Mexico waters near Sarasota, FL. Lillycrop et al. (1994) reported on the SHOALS system performance and accuracy during field-testing. Data collected with the SHOALS system meets USACE Class I and IHO Order 1 hydrographic survey standards. Through independent testing, both NOAA and the U.S. Navy verified again that SHOALS met these standards by comparing SHOALS depths to those collected by the acoustic fathometer aboard the NOAA Mt. Mitchell hydrographic survey vessel (Riley, 1995). Furthermore, Irish et al. (2000a) compared SHOALS measurements with highly accurate depth measurements collected with the USACE Coastal Research Amphibious Buggy (CRAB) at Duck, NC, both surveys collected in June 1996. This investigation again verified that SHOALS meets both IHO and USACE survey standards. Figure 2.8 shows both the Riley (1995) and Irish et al. (2000a) field verifications.

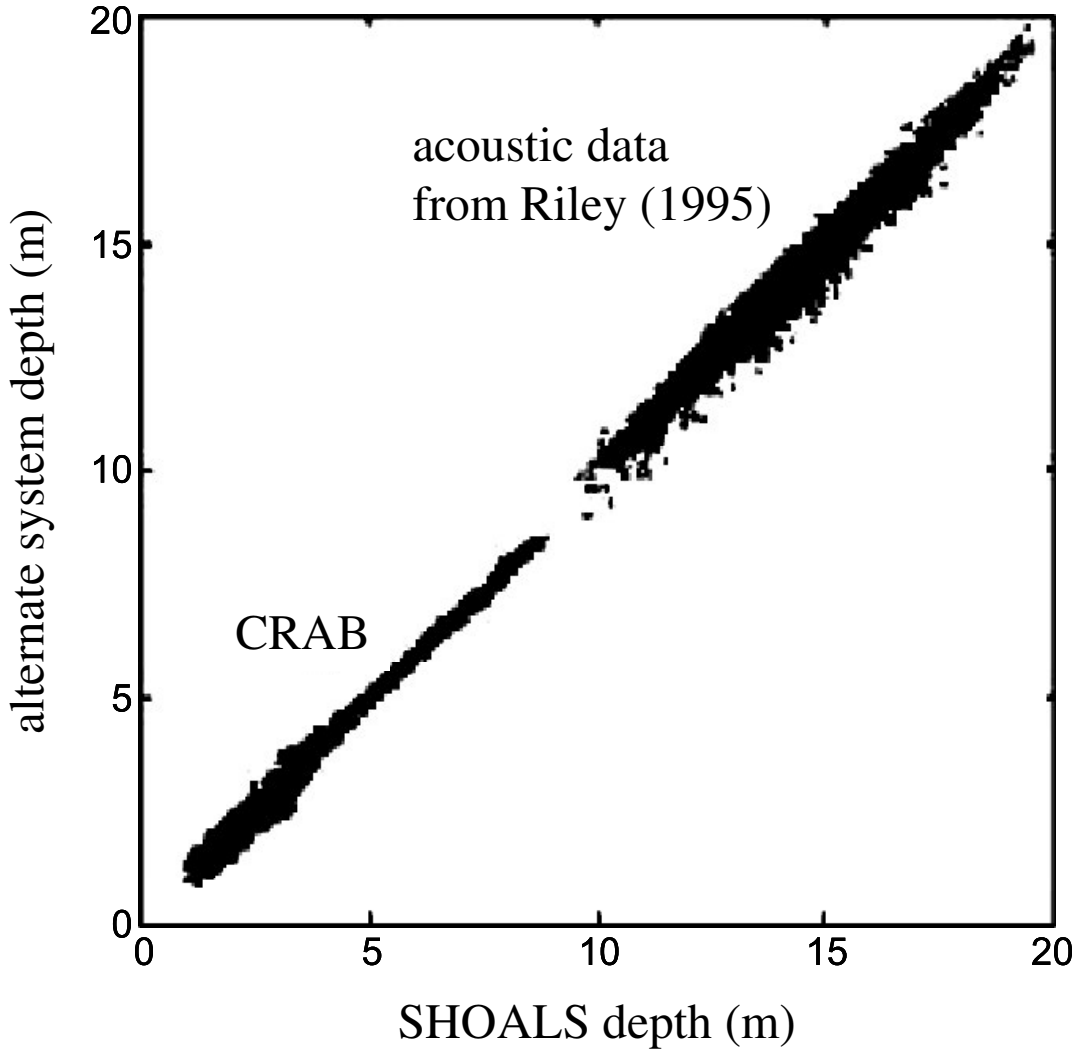

Figure 2.8 SHOALS field verification (modified from Irish et al., 2000a).

Since 1994, the SHOALS system has been used extensively to complete hydrographic survey missions for the USACE, the U.S. Naval Oceanographic Office, NOAA, USGS, and several international and state governments.

2.4 Detailed Mapping of Complex Coastal Environments: Tidal Inlets

The application of ALB for monitoring coastal inlets improves our understanding of these highly complex environments. Tidal inlets are dynamic environments where changing conditions continually affect inlet stability, and a firm understanding of a particular tidal inlet's geomorphology and sediment patterns is critical for quality coastal navigation management and engineering design.

Typically, navigation channels maintained at these inlets are designed and maintained by analyzing surveys that are limited to the extent of the maintained channel (Figure 1.1). This limited amount of data in such a complex environment makes it difficult to design a navigation channel that maintains safe navigable conditions, optimizes channel-dredging requirements, and effectively manages sediment bypassing. While supplemental aerial photography is oftentimes available to provide information on the aerial extent and location of key inlet features such as the ebb shoal, natural channel position, and adjacent beaches, they do not provide a means for reliably quantifying sediment volumes of these features.

ALB allows for near-synoptic, hydrographic surveying of the complete tidal inlet system allowing quantification of important sediment volumes. Furthermore, these lidar data sets highly resolve complex features, like the ebb shoal, to allow quantification of complex morphological processes. Additionally, the highly resolved bathymetry resulting from ALB surveys allows for improved numerical

model grid development, thus greatly improving the performance of hydrodynamic, wave, and morphological models.

For this study, consecutive ALB data sets were collected at two tidal inlets using the SHOALS system. These data sets were the first such near-synoptic data sets to be repeatedly collected in such complex, dynamic coastal environments. For this study, these data sets were analyzed to determine sediment changes at the inlets. Such quantification of morphologic evolution cannot practically be measured with other technologies.

2.4.1 Moriches Inlet, NY

Moriches Inlet is on Long Island, NY between Fire Island National Seashore, to the west, and Westhampton Beach, to the east (Figure 2.9). The inlet is jettied on both its east and west sides and provides access between the Atlantic Ocean and Moriches Bay. Periodic dredging by the USACE maintains a navigation channel 3.1 m deep and 61 m wide. SHOALS surveys were collected a number of times at the inlet, with the first in June 1994 (Irish and White, 1998). A second survey, just prior to maintenance dredging, was collected in June 1996. The 1994 and 1996 surveys covered a 2-km^2 area providing complete coverage of the ebb shoal, inlet throat, and the adjacent beach to the east. The 1994 and 1996 ALB surveys each provided 200,000 individual depth measurements.

The 1994 bathymetry mapped the ebb shoal and natural channel position (Figure 2.10). The 1994 channel position was west of the maintained alignment and runs southeast from the inlet throat through the ebb shoal. The nearshore bathymetry of Westhampton Beach immediately adjacent to the inlet is somewhat irregular; however, the contours are nearly shore parallel further away from the inlet. For this

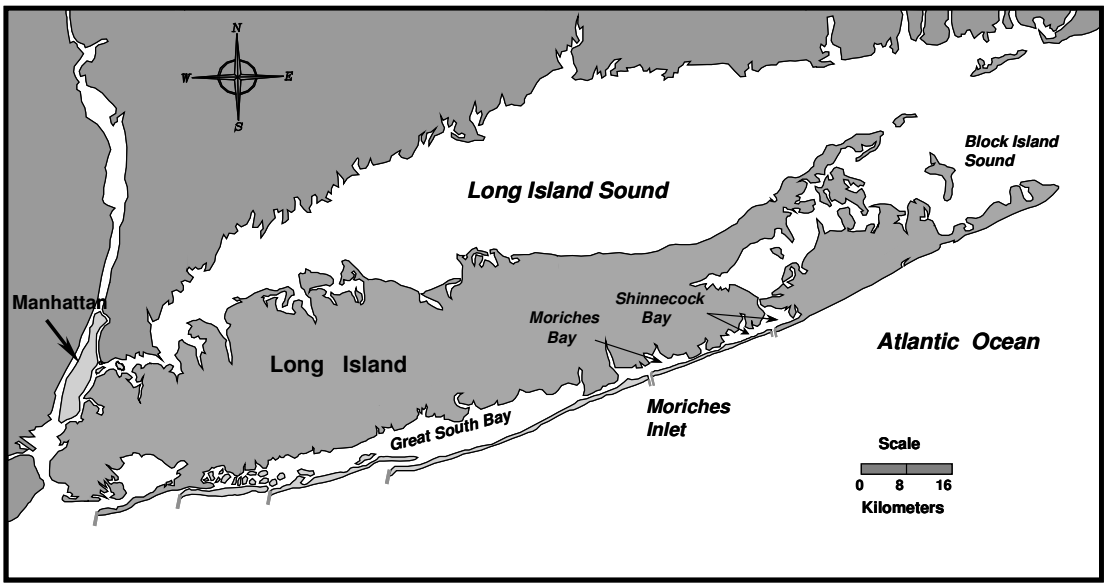

Figure 2.9 Location map for Moriches Inlet, NY.

study, the consecutive SHOALS data sets were compared to assess natural morphological changes. Between 1994 and 1996, several natural changes occurred in the inlet system (Figure 2.11). The channel migrated eastward over its entire length toward a position more in line with the maintained channel alignment (Irish, 1997). This is illustrated by an area of erosion paralleled by an area of accretion on the figure. Additionally, the ebb shoal retreated shoreward as indicated by an area of erosion along its offshore edge. However, volume difference computations of the ebb shoal indicate that material was conserved and Figure 2.11 shows accretion on the westward portion of the ebb shoal. Between 1994 and 1996, the adjacent beach to the east accreted. The 1996 survey included topographic elevations in addition to depths providing the current shoreline position of the inlet and adjacent beach.

Figure 2.10 SHOALS survey in 1994 at Moriches Inlet, NY (from Irish and White, 1998).

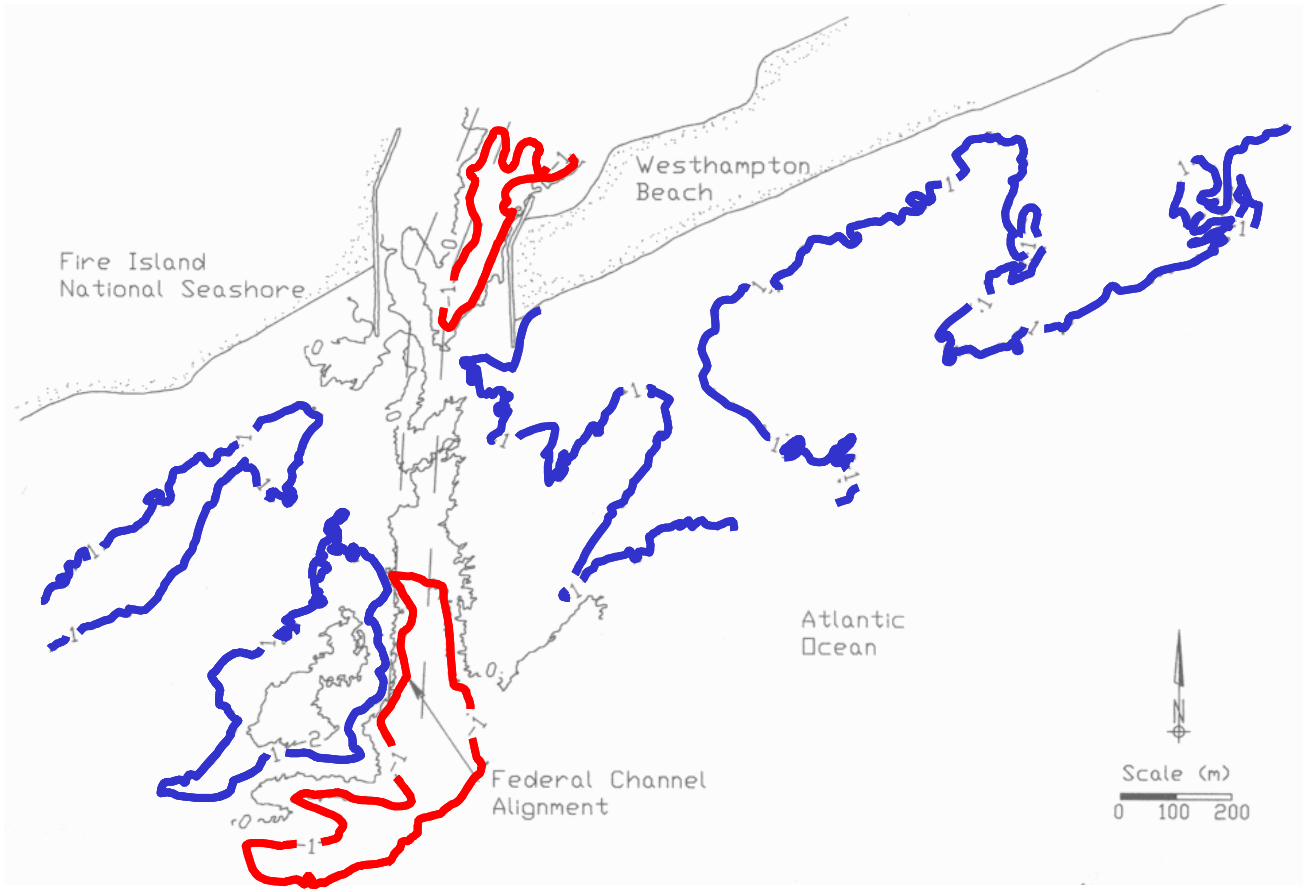

Figure 2.11 **Bathymetric difference plot between 1994 and 1996 SHOALS surveys at Moriches Inlet, NY. The 1-m erosion contours are highlighted in red and the 1-m accretion contours are highlighted in blue (modified from Irish and White, 1998).**

Since Irish and White (1998) presented the ALB surveys for Moriches Inlet, several numerical modeling investigations have benefited from these data sets. Several numerical modeling efforts are presently ongoing at Moriches Inlet (Irish et al., in press; Cañizares et al., in press; and Irish et al., 2004). Use of lidar bathymetry to define model grids at the inlet has improved model performance for predicting astronomical tides, storm water levels, and morphological change. Because multiple data sets exist for this inlet, they provide a means to verify morphological model performance (Cañizares, personal communications).

2.4.2 New Pass, FL: A Study of Morphologic Evolution

Data collected with an ALB system can improve our understanding of and our ability to quantify sediment losses and sediment gains at tidal inlets. Irish and Lillycrop (1997) investigated morphological evolution at New Pass, FL by using consecutive ALB surveys to quantify and characterize morphological changes at the inlet.

New Pass, Figure 2.12, is located on the west coast of Florida, across Sarasota Bay from Sarasota. The barrier island of Longboat Key is to the north and Lido Key to the immediate south. The pass is approximately 200 m wide at the inlet throat and includes a federal shallow-draft navigation project. The channel, authorized in 1964, is 45.7 m wide and dredged to 3.4 m and 3.8 m depths, depending on location along the channel. Since initial construction, the channel was dredged approximately once every four years to maintain the authorized channel depth and alignment, as the channel tends to migrate southward between dredging intervals. Prior to construction of the federal project, the natural pass shoaled frequently and experienced infrequent dredging by local concerns. Engineering activities at the inlet included the initial

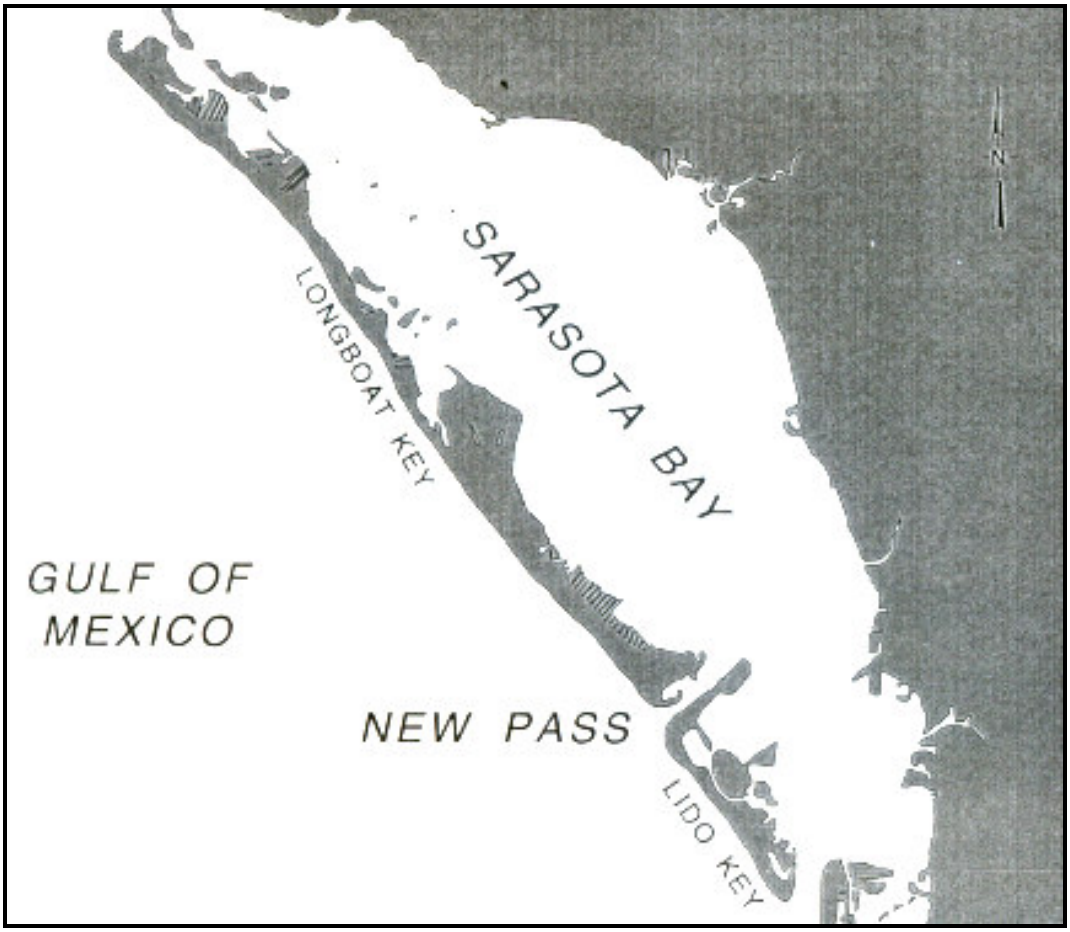

Figure 2.12 Location map for New Pass, FL (from Irish and Lillycrop, 1997).

construction and subsequent maintenance dredging in 1977, 1978, 1982, 1985, and 1990. As part of the 1982 dredging, the channel was realigned approximately 107 m to the south. The ebb shoal at New Pass was mined in 1993 and over 2 million m^3 of sand placed on Longboat Key.

2.4.2.1 Field Measurement Summary

Bathymetric data were collected, with the SHOALS system, at New Pass between March and December 1994. In addition, wave and tide data were also collected over this interval.

2.4.2.1.1 SHOALS Bathymetry

For this study, high-density bathymetry was collected with the SHOALS system for the first time at this tidal inlet in March 1994. Two additional lidar surveys of the pass were collected for this study in September 1994 and in December 1994. The New Pass survey area is about 4 km^2 and includes the navigation channel through the inlet throat and over the ebb shoal, as well as the mined borrow site along the seaward edge of the north side of the ebb shoal. The lidar survey depths range from 1.5 m to 8.0 m. The March 1994 data set includes over 170,000 individual soundings and was collected in less than one hour. This survey covers the ebb shoal and the navigation channel through the inlet throat and ebb shoal. However, this survey does not extend along Longboat or Lido Keys.

The September 1994 survey extends through the inlet throat, over the ebb shoal mined area, and along Longboat and Lido Keys. During this survey, “red tide”, a toxic algae, moved into the area and persisted for several weeks. The “red tide” impacts optical water clarity, and consequently, had adverse impacts on lidar data

collection. As a result, the September 1994 survey mission was abandoned before completion. Consequently, this data set is incomplete in that no depths were collected along a 500-m wide swath running parallel to the adjacent beaches, just seaward of the shoreline.

Working toward obtaining complete coverage of New Pass, the survey area became larger with each successive survey. The December 1994 survey includes over 875,000 individual soundings. This survey fully covers the ebb shoal and extends north onto Longboat Key, south onto Lido Key, and into the inlet throat. A contour plot of the lidar bathymetry at New Pass for December 1994 is given in Figure 2.13, and a three-dimensional relief plot of this same survey is given in Figure 2.14. The mined area, dredged to the 7-m depth contour, begins at the natural 5-m depth contour and extends seaward along the ebb shoal. Figure 2.13 and Figure 2.14 display the straight and distinct markings left by the dustpan dredge and indicate the steep gradient between the 5-m and 7-m contours. The current navigation channel alignment is also illustrated in both figures, and Figure 2.13 illustrates the authorized federal channel alignment. The actual navigation channel location is south of the authorized channel alignment indicating a southward migration of the channel. Through the inlet throat, the channel maintains a scoured depth at 4 m or deeper; however, as the channel extends seaward through the ebb shoal, the depth is shallower than the authorized channel depth.

2.4.2.1.2 Hydraulic Conditions

A USACE Directional Wave Gage (DWG) is located offshore of Lido Key, just south of New Pass, in 7 m of water. The gage has measured the significant wave height, water level, and mean wave direction (at the peak frequency) at 4-hour

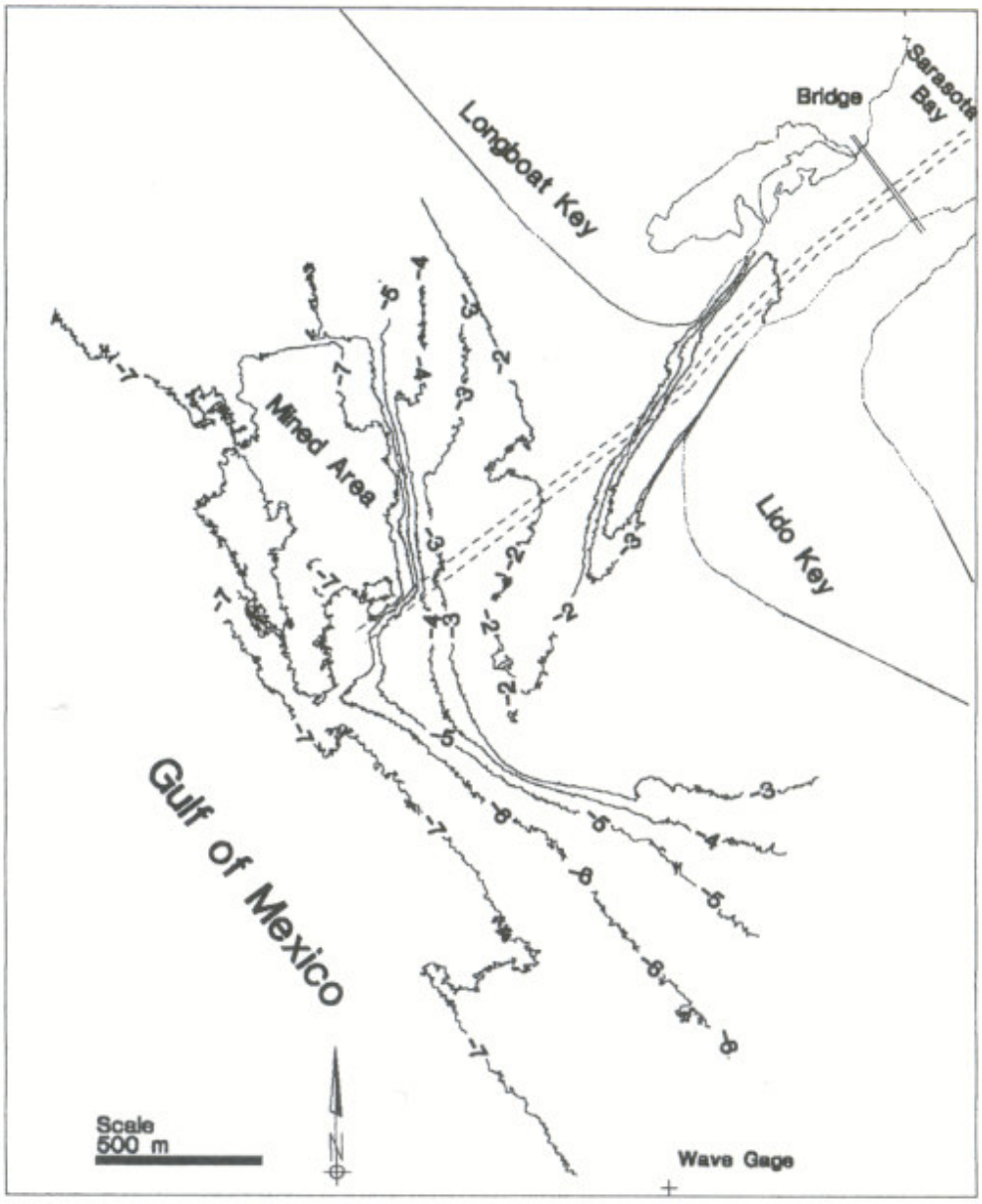

Figure 2.13 New Pass, FL lidar bathymetry, December 1994 (from Irish and Lillycrop, 1997).

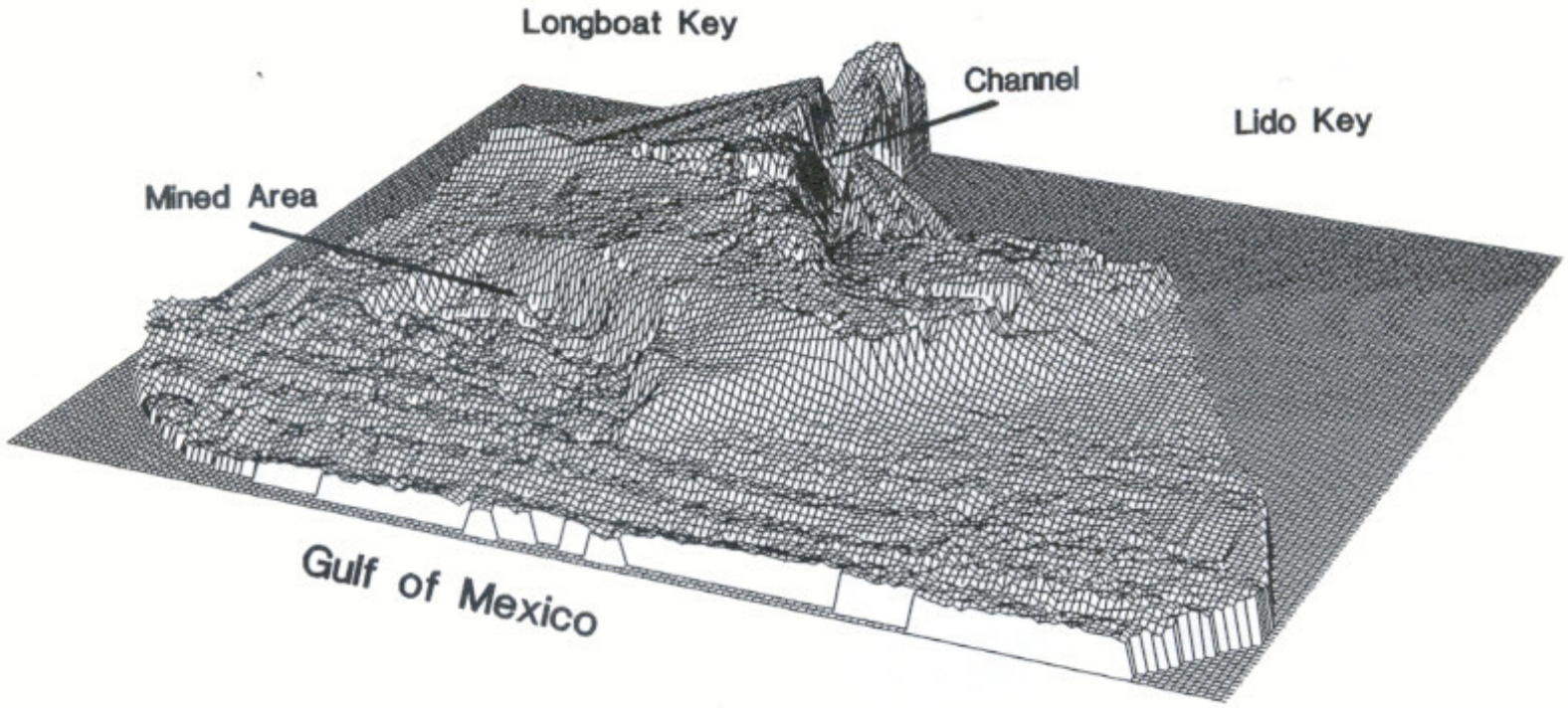

Figure 2.14 **Three-dimensional view of New Pass, FL lidar bathymetry, December 1994. North is to the left, and the area shown is 1.5 km cross-shore by 3.0 km alongshore (from Irish and Lillycrop, 1997).**

intervals since June 1993 (Figure 2.15, (a, b, and c, respectively) and Table 2.3). These data were analyzed for this study to assess the nearshore hydrodynamic climate. Figure 2.15a indicates several storm events occurring during the monitoring period, with the most significant storms occurring in March and October. During these storm events, the wave height peaked near 1.8 m.

Figure 2.15b indicates an elevated offshore water level during September and October (days 240 through 310); however, the cause of this elevated water level is not clear. During this time, the measured mean water level is above the Mean Low Water (MLW) datum.[1] Over the monitoring period, the mean tidal range inside Sarasota Bay at New Pass and at the offshore wave gage is approximately 0.46 m.

The wave direction time series, in Figure 2.15c, shows the direction from which the waves are approaching as measured from north. The inlet faces southwest and is oriented such that a wave approach direction of 236 degrees is directly onshore. The average wave direction between March and September is 190 degrees, or from the south-southwest, while the average wave direction between September and December is 249 degrees, or from the west-southwest. Figure 2.15c indicates an obvious shift in wave direction during September (near day 250). Before September, waves approached the inlet obliquely at approximately 45 degrees; however, after the shift, waves approached nearly normal to the inlet.

2.4.2.2 Data Analysis

For this study, the SHOALS data were analyzed to quantify morphological changes. To analyze these changes at New Pass, the survey area was divided into four

[1] MLW is equal to –0.1 m NGVD29.

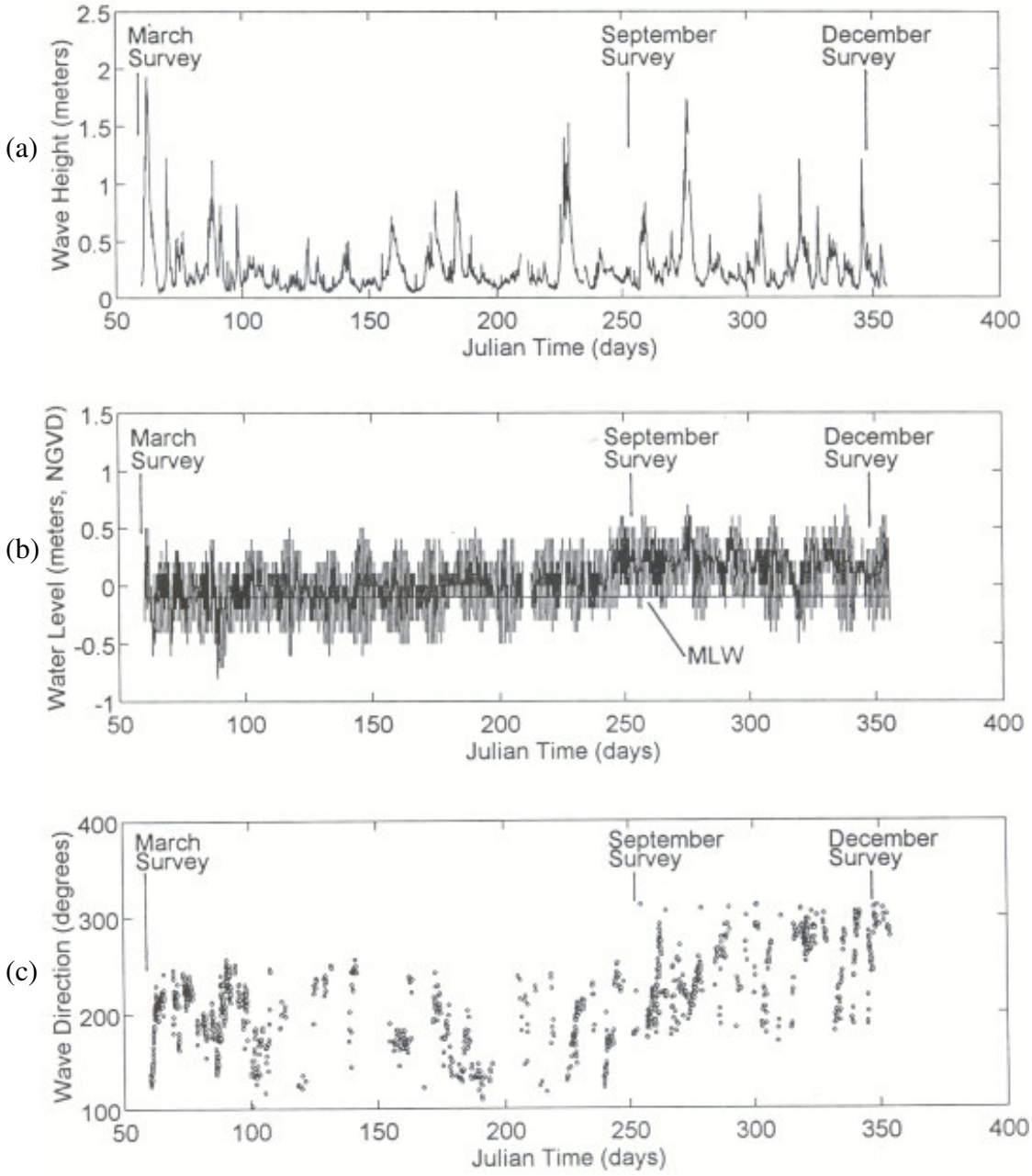

Figure 2.15 (a) wave height, (b) water level, and (c) wave direction from USACE wave gage near New Pass between March and December 1994. Julian day 60 is 1 March 1994 (from Irish and Lillycrop, 1997).

Table 2.3 Mean wave conditions near New Pass, FL in 1994.

Case Number	Time Interval	Mean Wave Height (m)	Mean Wave Period (m)	Mean Wave Direction (deg)
1	March to September	0.26	5.3	190 (SSW)
2	September to December	0.25	5.6	249 (WSW)

control areas: the navigation channel, the ebb shoal, the southern end of Longboat Key, and the northern end of Lido Key (Figure 2.16). Delineation of control areas is somewhat arbitrary, and for this study, they were selected to delineate between the ebb shoal and natural channel and to accommodate differences in the aerial extents of the three SHOALS survey sets, as discussed below.

For each control area, a volume change between each survey set was computed using the high-density lidar bathymetry sets. The volume computation results for the monitoring period are tabulated in Table 2.4. Because the March survey did not extend north onto Longboat Key nor south onto Lido Key, volume change computations between March and September were limited to the navigation channel and the ebb shoal. In addition, all volume computations are limited by the September data set that does not extend completely over the ebb shoal. Volume changes were computed only where overlapping data were available and no extrapolations were made where data did not exist.

The computations presented in Table 2.4 indicate considerable loss of material from the ebb shoal control area between March and September. While a loss of 84,500 m^3 of sediment from the ebb shoal is improbable given the wave climate, it

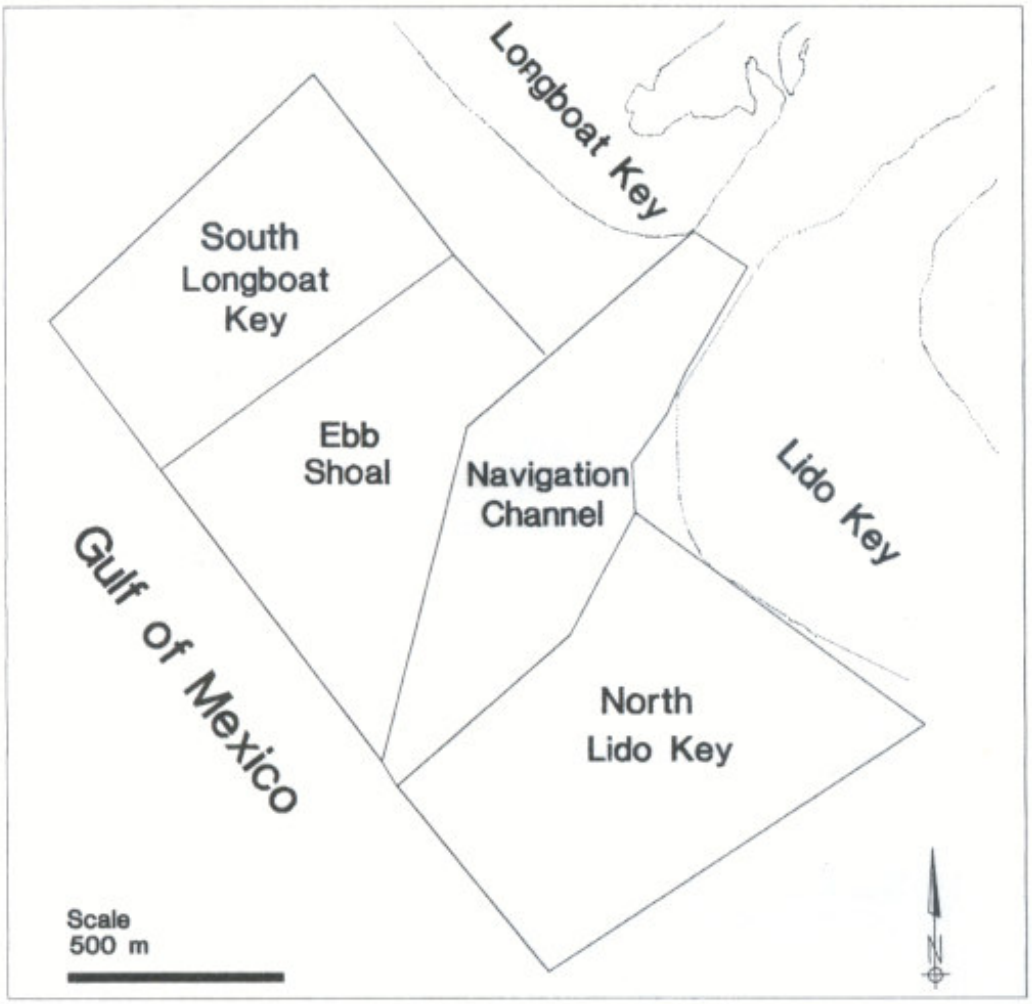

Figure 2.16 New Pass, FL control areas for volume computations (from Irish and Lillycrop, 1997).

Table 2.4 Volume changes at New Pass, FL.

Survey Period	Volume Change (m^3)				
	Navigation Channel	Ebb Shoal	Longboat Key	Lido Key	Total
March to September	+16,500	-84,500	N/A	N/A	-68,000*
September to December	+30,400	-4,800	+18,300	+13,200	+57,100
March to December	+46,900	-89,300	N/A	N/A	-42,400*

*Summation of navigation channel and ebb shoal control areas only.

is possible that the defined control area has lost this material. The data indicates that material has moved out of the ebb shoal control area; however, it is probably not lost from the ebb shoal system. This material has likely migrated into other control areas and other areas of the ebb shoal not surveyed. Figure 2.17 shows erosion and accretion in the survey area between March and September. The figure indicates that erosion has occurred along the outer boundary of the ebb shoal, specifically in the vicinity of the dredge cut at the shoal mine location. Shoaling has occurred inside the navigation channel control area adjacent to the ebb shoal control area, suggesting that sediment has shifted out of one area and into the other. There are additional areas of erosion along the ebb shoal, indicating a loss of sediment to the ebb shoal control area. Because the volume comparisons are limited by the September survey, the area shoreward of the ebb shoal control area was not evaluated; however, it is likely that this area has experienced accretion between March and September. Furthermore, the

Figure 2.17 Accretion (grey) and erosion (black) at New Pass, FL between March and September 1994 (from Irish and Lillycrop, 1997).

wave direction time series from the wave gage implies northerly longshore transport between March and September and a probable loss of sediment from the ebb shoal onto Longboat Key.

In contrast to the first portion of the monitoring period, the ebb shoal control area shows little volumetric change between September and December (Figure 2.18). This figure indicates that there is no significant movement of material over the ebb shoal.

Profiles through the three data sets taken perpendicular to the dredge cut indicate that some slope adjustment has taken place during the 9-month monitoring period (Figure 2.19). The profile cross-section is indicated by the line A-A' on Figure 2.18. The figure indicates that the slope is becoming less steep over time and that there was little change in depth seaward of the ebb shoal cut.

Between March and September, the navigation channel control area gained material, indicating that some channel shoaling occurred. Furthermore, the area continued to accumulate sediment between September and December. Figure 2.17 and Figure 2.18 both show areas of accretion to the north of the channel section through the ebb shoal. However, the most considerable shoaling occurred between March and September, where depths are nearly 1 m shallower in September than in March.

Between March and September, there was also some erosion along the entire surveyed length of channel extending from the inlet throat through the ebb shoal. This loss of sediment from the control area may be a result of transport by tidal currents.

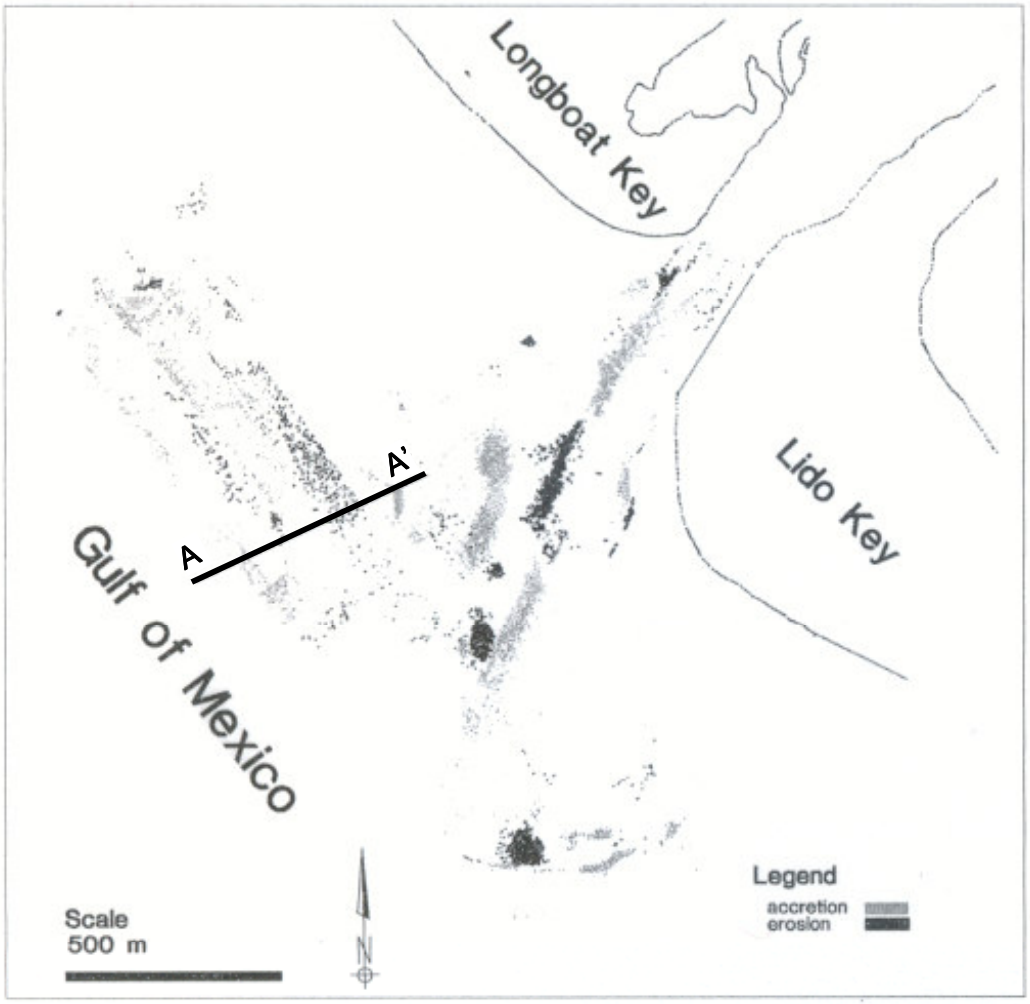

Figure 2.18 Accretion (grey) and erosion (black) at New Pass, FL between September and December 1994 (from Irish and Lillycrop, 1997).

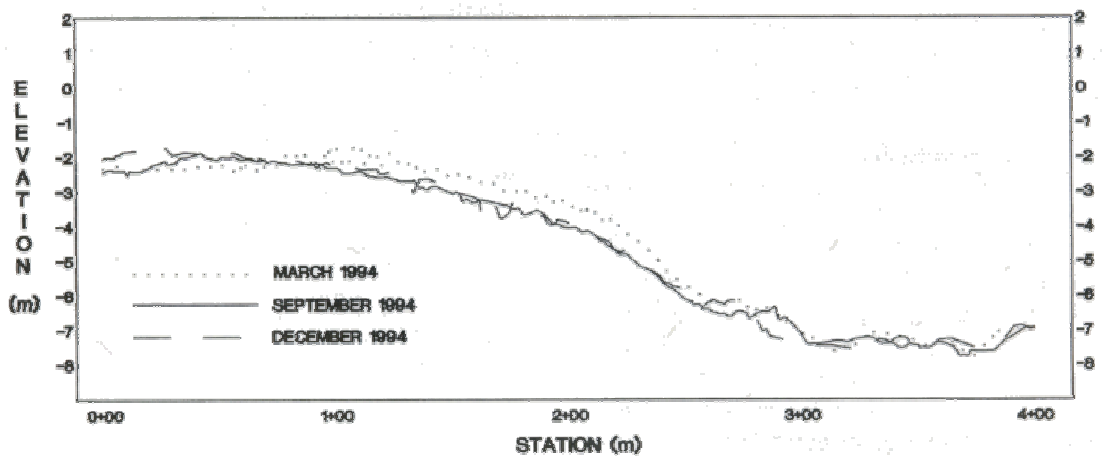

Figure 2.19 Cross-sections through the ebb shoal perpendicular to the dredge cut. The cross-sections are taken along A-A' shown on Figure 2.18. In this figure, the original dredge cut is indicated by the steep slope between stations 2+00 and 3+00 (from Irish and Lillycrop, 1997).

The navigation channel thalweg, or centerline, positions during each of the three surveys are illustrated in Figure 2.20. During the 9-month monitoring period, the channel position through the inlet throat appeared stable. However, there is southward migration of the seaward channel section through the ebb shoal. The channel migrated at an average rate of 17 m per month, moving southward about 150 m over the monitoring period.

While the March lidar survey does not include depth information along the southern end of Longboat Key nor the northern end of Lido Key, there is data in these areas for the September and December surveys. Volumetric computations show uniform accretion on the southern end of Longboat Key, just north of the inlet.

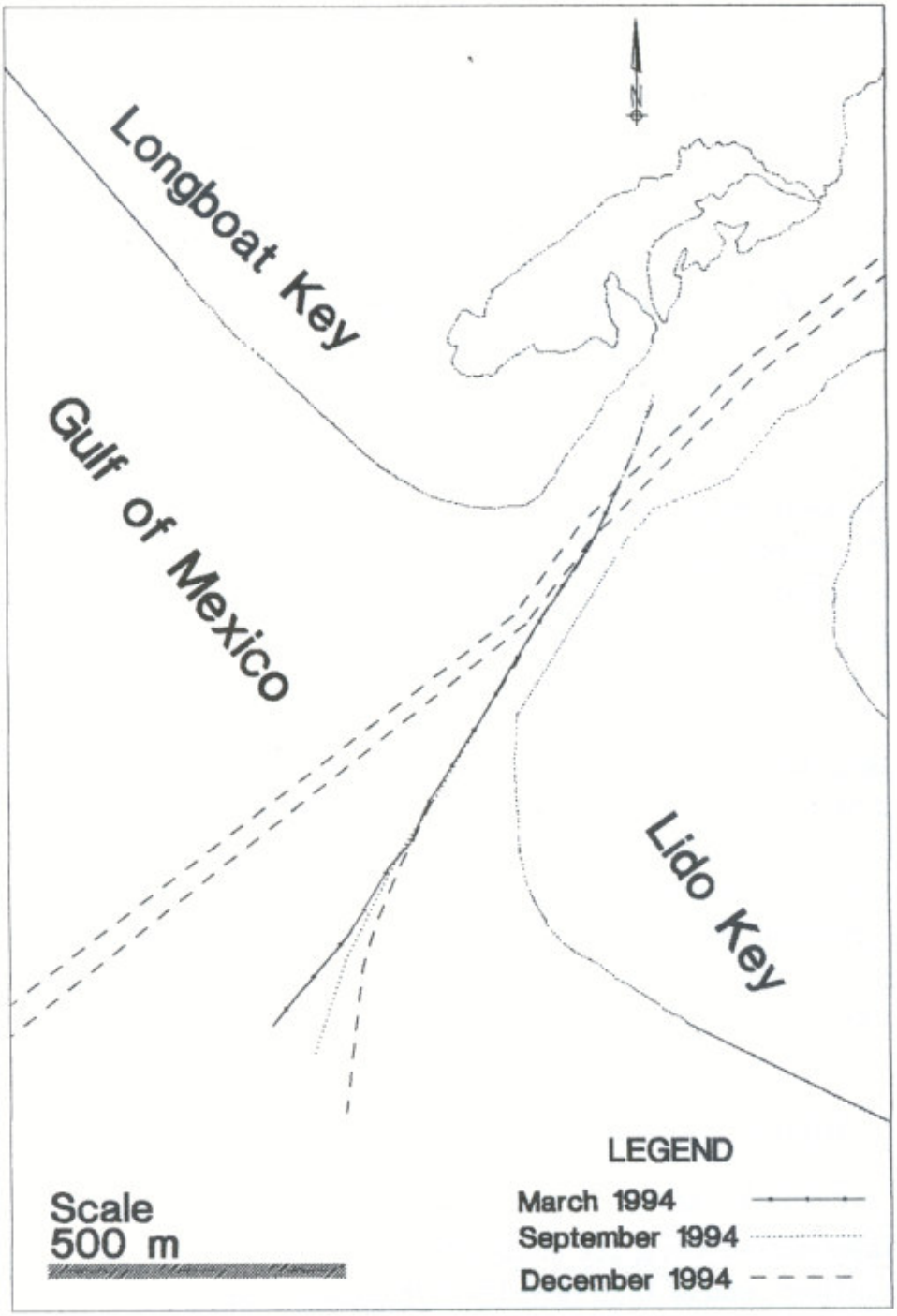

Figure 2.20 Navigation channel thalweg positions at New Pass, FL (from Irish and Lillycrop, 1997).

Furthermore, volume computations show that the north Lido Key control area has accreted as well, but Figure 2.18 illustrates that this accretion is localized as a shoal formation.

2.4.2.3 Results

The SHOALS data provide quantitative estimates of control volume change over two short time periods, and wave gage measurements suggest that longshore transport direction differs for these two time periods. However, the SHOALS bathymetry and wave gage information do not provide quantitative measurement of control-volume sediment flux. Further field investigations may be required to fully understand the complexities of this inlet system.

Since Irish and Lillycrop (1997) reported on the three SHOALS surveys collected at New Pass in 1994, several additional ALB surveys have been collected. McClung (2000) provided a comprehensive analysis of morphological processes at New Pass based on these additional ALB surveys and hydrodynamic analyses.

2.5 Beach Nourishment Project Design

Costs per cubic meter of sand placed on a beach ranges from $5 to $30, and beach nourishment projects vary from several thousands of cubic meters, such as the project at St. Joseph, MI of 39,000 m^3, to millions of cubic meters, such as the project at Miami Beach, FL of 12 million m^3. Underestimating project design volumes can result in cost overruns or a reduced amount of sand being placed on the beach. Conversely, overestimated project design volumes can result in excessive budgeting and planning.

Hydrographic surveys are the primary tool for calculating beach nourishment project volumes. Conventional survey techniques use shore-normal wading depth surveys matched with offshore acoustic surveys, spaced at intervals along the beach ranging from 30 m to 300 m.

Calculation of project volumes relies on the assumption that there is little topographic or bathymetric variability from one profile line to the next, or that if there is variability, it averages out over the project limits. However, beach and nearshore topography are highly three dimensional as a result of sub-aerial sand dunes, nearshore bars, hard-bottom outcrops, seawalls, and groins. At profile spacings typically on the order of 300 m, these assumptions are often violated. Now that ALB surveys are available and are economically viable, high-resolution beach and nearshore surveys may be used instead. ALB surveys provide a means for more accurate beach volume calculations.

The following sections, based on Irish et al. (1997), illustrate the value of ALB surveys for beach fill volume calculations by presenting ALB surveys at four locations: Longboat Key, FL on the Gulf of Mexico; Island Beach State Park, NJ on the Atlantic Ocean; and St. Joseph, MI and Presque Isle, PA on the Great Lakes (Figure 2.21). The ALB data collected for this study were the first such high-resolution data sets to be used to evaluate beach nourishment projects.

2.5.1 Longboat Key, FL

Longboat Key, FL is on the east shore of the Gulf of Mexico and is situated between Longboat Pass, to the north, and New Pass, to the south (Figure 2.12). Over two million cubic meters of beach-quality sand were placed on the southern-most 8.5 km of the key in 1993 to protect the shoreline from further erosion.

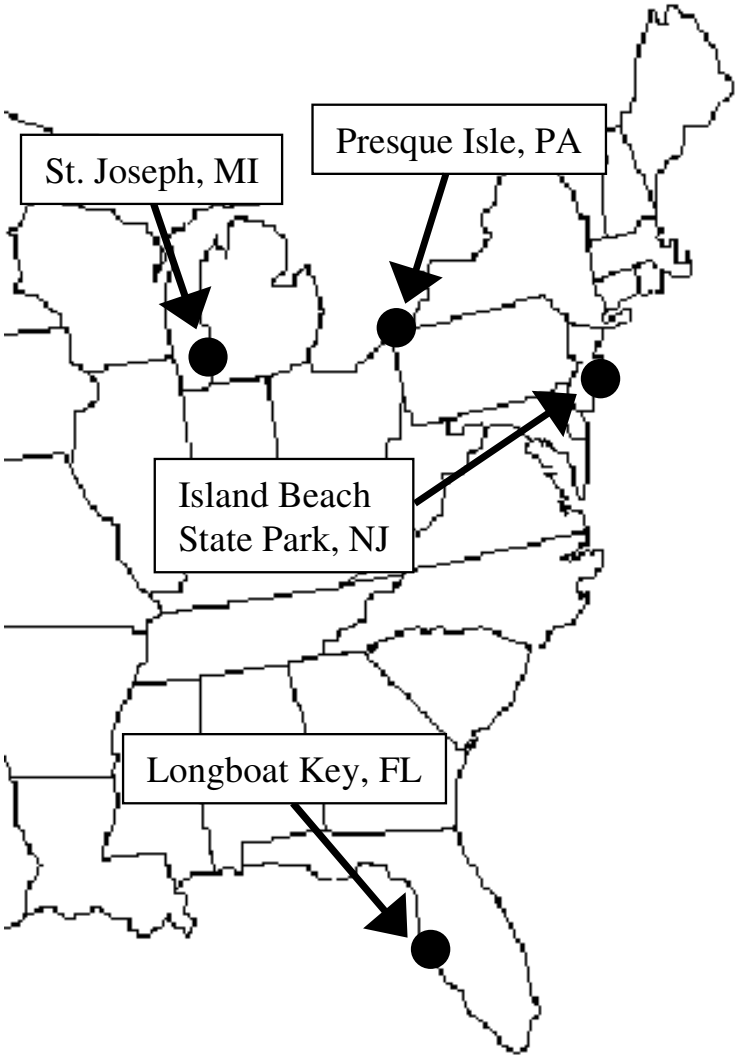

Figure 2.21 Location map for four beach nourishment projects.

SHOALS surveyed the area 5 times since March 1994 to monitor the nourishment project (Irish and Truitt, 1995). The high-resolution SHOALS bathymetry collected in November 1995 reveal a complex sandbar system in the nearshore (Figure 2.22a). The dual bar system merges together and separates as it parallels the shoreline. At the southern end of the key, the seaward bar diverges into the ebb shoal of New Pass. Conventional profile data are regularly collected along profiles spaced 300 m apart and outline the dual bar system. However, these data sets do not reflect local complexities in the nearshore, as shown in Figure 2.22b. The simulated profile bathymetry will be discussed in Chapter 2.5.5.

2.5.2 Island Beach State Park, NJ

A 2.5-km stretch of Island Beach State Park, NJ, just north of Barnegat Inlet, was surveyed with SHOALS in 1994. The park is directly exposed to the Atlantic Ocean and is characterized by shore-perpendicular sand ridges stretching from the dry beach through the nearshore. Because the area is a state park, no manmade alterations are permitted. However, Barnegat Inlet, jettied on both its north and south sides, does impact Island Beach. SHOALS surveyed the southernmost 2.5 km of the park in June 1994 (Figure 2.23a). The survey details the beach's three dimensionality quantifying the sand formations and the shoaled areas formed by inlet processes.

2.5.3 St. Joseph, MI

St. Joseph, on the southeastern shore of Lake Michigan, was authorized as a beach nourishment project in 1976. In 1903, two jetties were constructed to stabilize the St. Joseph River entrance. These jetties interrupt the natural southerly longshore

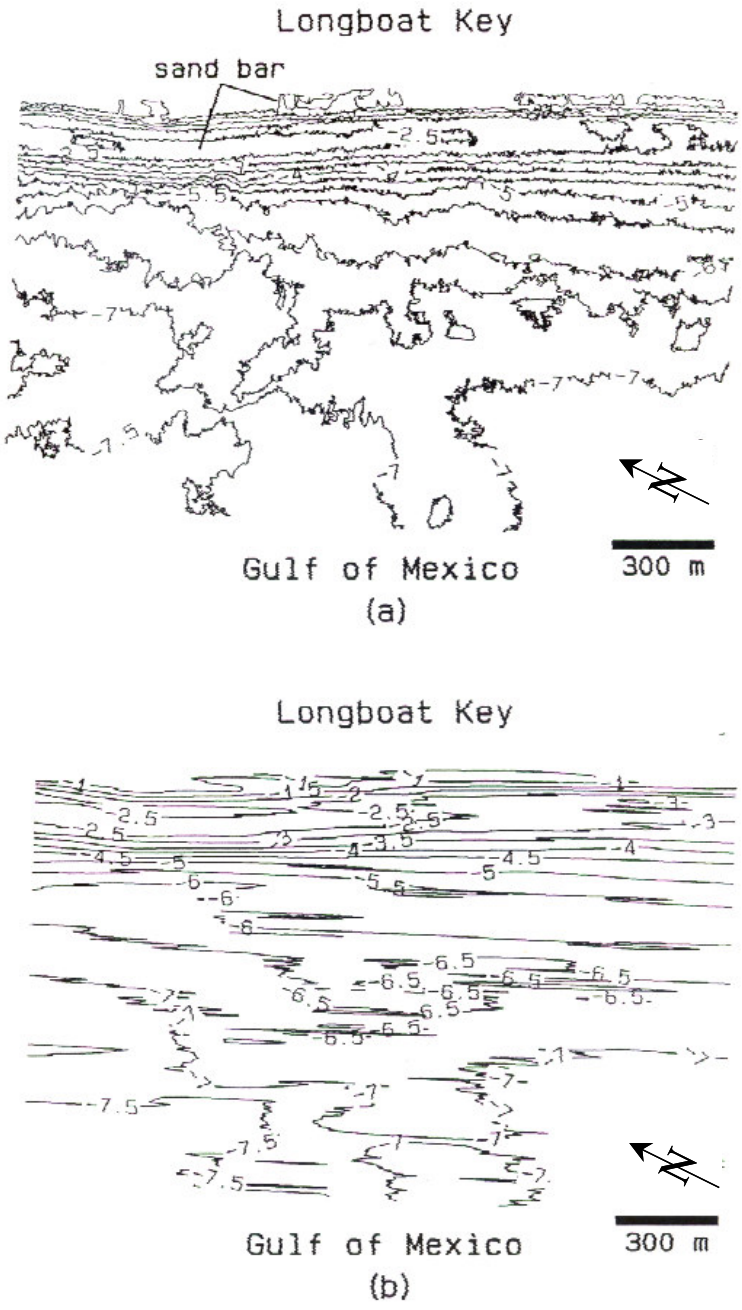

Figure 2.22 Longboat Key, FL, November 1995: (a) representative section of SHOALS bathymetry and (b) simulated profile bathymetry at 300-m spacing. All depths are in meters referenced to NGVD29 (from Irish et al., 1997).

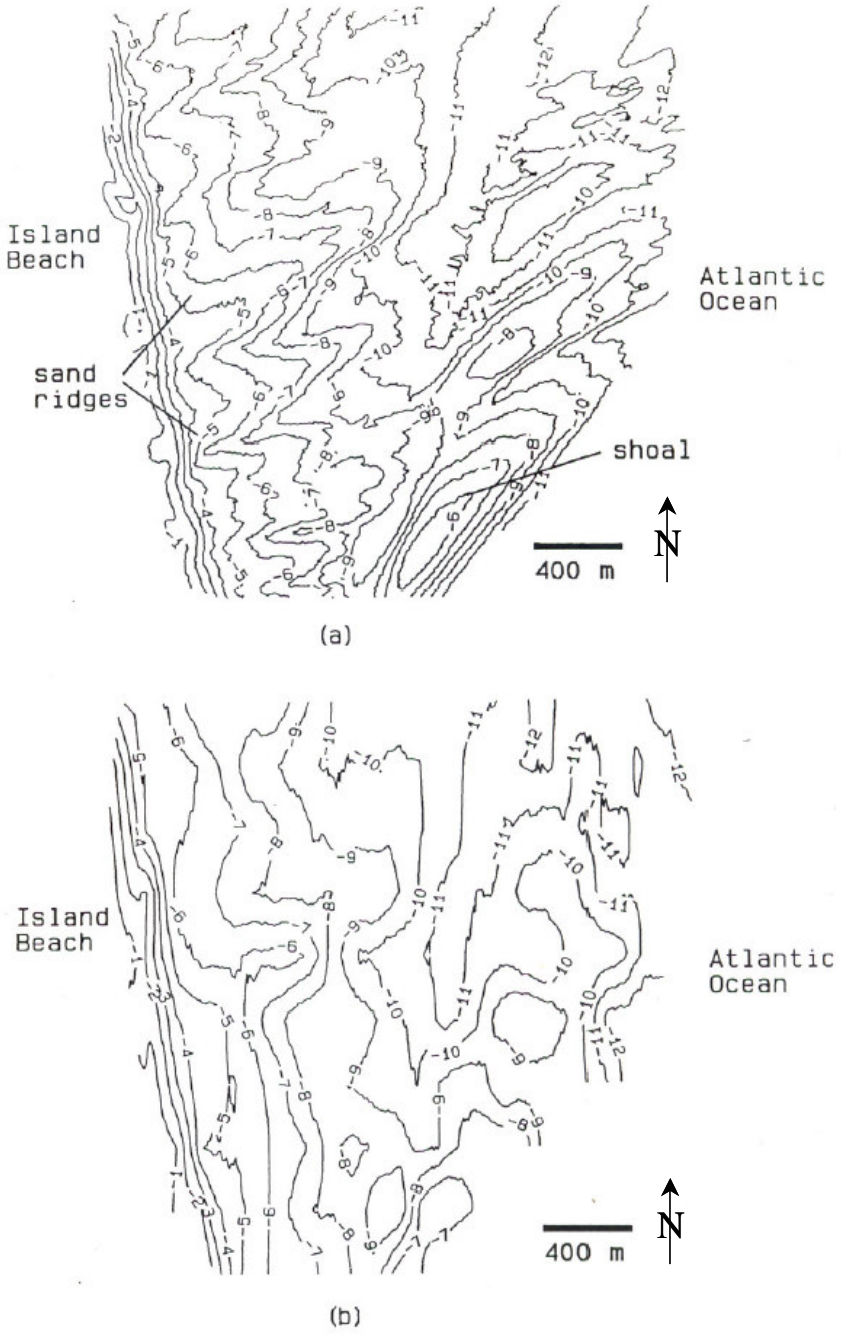

Figure 2.23 Island Beach State Park, NJ, June 1994: (a) SHOALS bathymetry and (b) simulated profile bathymetry at 300-m spacing. All depths are in meters referenced to NGVD29 (from Irish et al., 1997).

transport of 84,000 m^3 per year, and as a consequence, the downdrift beach experienced erosion and the lakebed suffered down cutting (Parson and Smith, 1995).

Since 1976, the USACE annually placed dredged material from the maintenance dredging of St. Joseph Harbor south of the entrance to form a feeder beach to replenish 6 km of shoreline. Additionally, coarser material from an upland source is periodically placed. Typically, bathymetric and topographic data are collected along survey lines spaced 152 m apart through the fill area and 800 m apart south of the fill area. In August 1995, SHOALS surveyed the project collecting nearly 400,000 soundings (Figure 2.24a). The SHOALS data quantified areas of severe lakebed down cutting and identified a previously undiscovered submerged headland-like feature with a 2-m relief.

2.5.4 Presque Isle, PA

The Presque Isle peninsula is on the south shore of Lake Erie at Erie, PA. The peninsula historically tends to migrate eastward causing erosion of the lakeside beach. Occasionally, the area breaches and causes dangerous navigation conditions in Erie Harbor, situated between the peninsula and the mainland. The USACE has taken several measures to prevent erosion, including beach nourishment and the construction of groins (Grace, 1989). In 1992, the USACE installed 55 detached breakwaters offshore of Presque Isle over a 10-km alongshore distance. Each breakwater is 47.5 m long and is separated by a 106.7 m gap. Additionally, 285,000 m^3 of beach fill material were placed initially and renourishment occurs annually (Mohr, 1994). Ongoing project monitoring of the performance of the breakwater system includes bathymetry and topography collected annually along cross-shore profiles spaced 300 m to 600 m apart. In August 1995, the SHOALS system was used to survey this

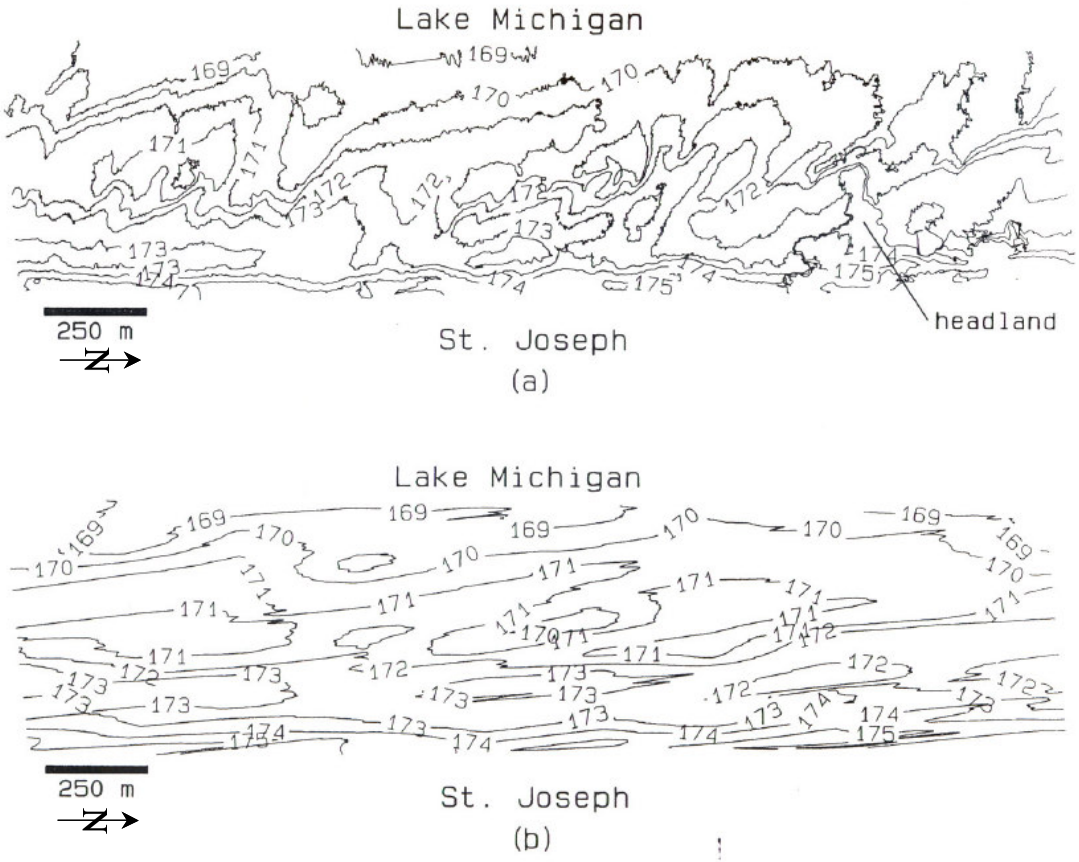

Figure 2.24 **St. Joseph, MI, August 1995: (a) representative section of SHOALS bathymetry and (b) simulated profile bathymetry at 300-m spacing. All depths are in meters referenced to IGLD (from Irish et al., 1997).**

breakwater system detailing the salient and tombolo formations shoreward of the structure and the fairly uniform bottom seaward of the structures (Figure 2.25a).

2.5.5 Data Analysis

For this study, the benefit of high-resolution lidar bathymetry for beach nourishment design was evaluated by simulating alongshore profile data from the SHOALS surveys at spacings varying from 5 m to 300 m. The resulting bathymetric contours for the simulated profiles at 300 m spacing are shown in Figure 2.22b through Figure 2.25b, illustrating the loss of detail with such a wide spacing. For this study, these bathymetric contours were approximated by developing a Triangulated Irregular Network (TIN) from the simulated profiles. Depth contours were then drawn based on lines of equal elevation along the TIN.

To simplify calculations for this study, volumes were computed between the horizontal plane representing the mean water vertical datum and the bottom topography presented by the simulated profiles. This in effect gives the volume of water above the profile, rather than sand volume. However, the magnitude of volume differences between the volume computed with one profile spacing and the volume computed with another does represent the sediment volume difference between the profiles. Throughout this section, the term volume will indicate the volume of water between the bottom and the mean water vertical datum while the term volume difference will indicate the difference in sediment volume between one profile spacing and another.

Volumes were computed using the well-known area-end method for each profile spacing. When employing the area end method, the cross-sectional area between the bathymetry and mean water at each profile location was first calculated.

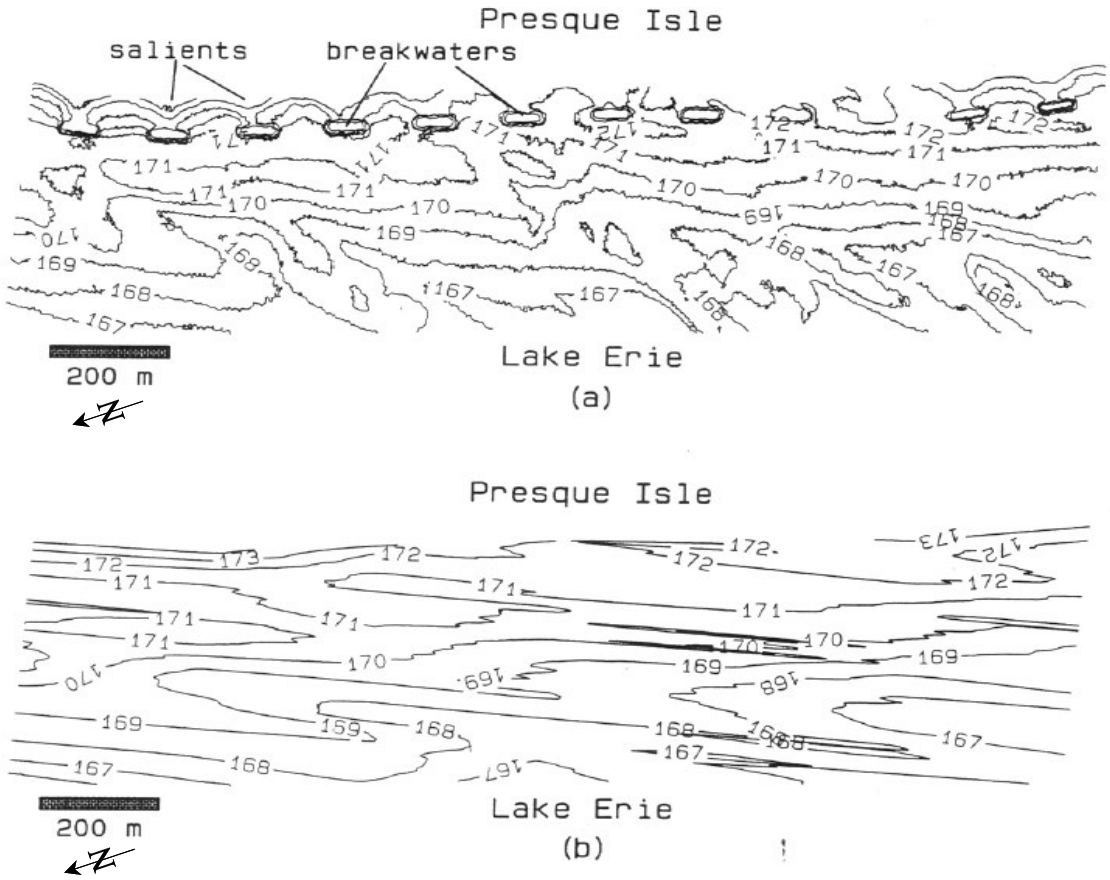

Figure 2.25 **Presque Isle, PA, August 1995: (a) representative section of SHOALS bathymetry and (b) simulated profile bathymetry at 300-m spacing. All depths are in meters referenced to IGLD (from Irish et al., 1997).**

The calculated area at one profile location (A_1) was then averaged with that of the next consecutive profile (A_2). The product of this averaged area and the length between the two consecutive profiles (L) gives the volume between the profiles:

$$V = L\left(\frac{A_1 + A_2}{2}\right) \tag{2.5}$$

The total volume for the entire project is then equal to the summation of the volumes. The computed results for all four locations are presented in Table 2.5 as the volume difference between the highest resolution set, 5 m spacing, and the stated spacing, in cubic meters per meter length of beach. Positive differences indicate that the stated spacing resulted in a sediment volume larger than the 5 m spacing while negative differences indicate a smaller sediment volume.

2.5.6 Results

The resulting volume calculations, in general, show that as the spacing between profiles increases, so too does the error in computed volumes. Figure 2.26 gives a plot of absolute deviation from the 5-m volume (volume error) versus profile spacing for the four sites. In general, the volume error becomes more random and larger in magnitude as profiles spacing increases. This trend might be related to the true horizontal length scale of bathymetric features. This is consistent with the findings of Saville and Caldwell (1952). In their investigation, the use of average profiles at spacings varying from 120 m to 2,800 m to represent lengths of a fairly uniform beach were analyzed for accuracy in evaluating engineering volumes. The spacing error, defined as the accuracy measurement of a particular profile in representing a section of beach, was evaluated by comparing the selected profile with

Table 2.5 Computed sediment volume differences.

Profile Spacing (m)	Volume Difference (m^3/m)			
	Longboat Key	Island Beach	St. Joseph	Presque Isle
5	0.0	0.0	0.0	0.0
10	+0.4	-0.1	0.0	-1.2
25	0.0	+0.1	+0.4	-1.9
30	+1.8	-0.1	-0.2	-0.8
50	-0.2	+0.3	+1.7	-3.3
60	+3.1	-0.2	-2.3	-0.9
100	+1.6	+1.9	+3.3	-6.1
150	+0.7	+0.3	+6.5	+10.4
200	-2.2	-5.3	+18.5	-0.8
250	+6.6	+15.9	-8.4	-4.2
300	-12.3	+19.8	+5.3	+9.8

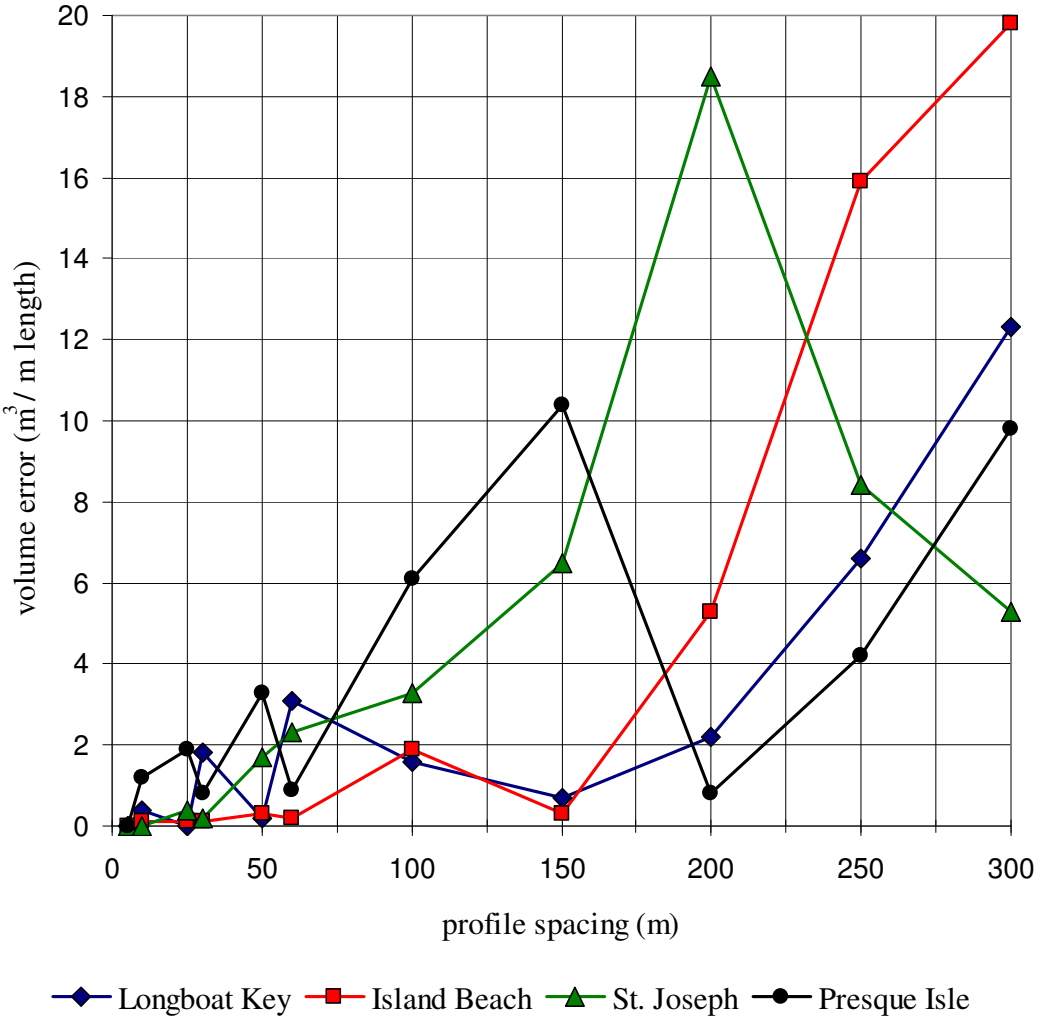

Figure 2.26 Measured beach fill volume error versus alongshore profile spacing (modified from Irish et al., 1997).

the average profile for that section. The spacing error was then translated into a volume error, defined as the total volume difference over the project length. Their conclusions stated that the volume error increases nearly linearly as profile spacing increases. Saville and Caldwell's (1952) results do not indicate randomness in volume error; however, the results from this investigation do. This is most probably attributed to the irregularities in the bathymetry evaluated herein, as discussed below.

Of the four sites, the bathymetry at Longboat Key shows the least alongshore variation. This is reflected in the results where the volume error at Longboat Key is within 5 m^3/m for profile spacings as great as 200 m. However, the area is still highly three dimensional, and the volume error when using 200-m, 250-m, and 300-m spacings continually increases and is as much as 12.3 m^3/m. The calculations for Island Beach State Park indicated similar findings. Here, the volume error is small for profile spacings less than 200 m, and as the spacing increases beyond 200 m, the measured volume error increases. In contrast to Longboat Key, the bathymetry at Island Beach State Park is highly variable alongshore with shore-normal sand ridges occurring every 400 to 500 m. This investigation indicates that bathymetric variations associated with these large features do not impact volume computations until the profile spacing exceeds 200 m.

The analysis at St. Joseph shows that profiles spacings larger than 100 m result in significant volume error. Differing from Longboat Key and Island Beach State Park, as the profile spacing is increased at St. Joseph, the volume error does not continually increase. The measured volume error at St. Joseph when a 250-m spacing is used is significantly lower than that measured when a 200-m spacing is used. However, all spacings greater than 100 m result in volume errors larger than 5 m^3/m.

Of the four projects, volume calculation at Presque Isle is most impacted by survey spacing changes between 5 and 50 m. Further, volume calculations deviate significantly with spacings greater than 50 m. Of the spacings evaluated at Presque Isle, the volumes computed using 150-m spacing yielded the largest error, 10.4 m^3/m. When spacing is increased to 200 m, the volume error dramatically decreases. Because of the uniform repetition of salient formations every 155 m, corresponding with the breakwater field, it is probable this decrease in volume error is a result of these features. By chance, the profile locations at the 200-m spacing were such that volume error between consecutive profiles averaged out over the project length.

The economic impact of profile spacing is evident in Figure 2.27 where the cost error, or absolute cost difference per cubic meter per unit length of beach, for the Presque Isle project is displayed. The lower and upper cost error boundaries were calculated using a cost per cubic meter of beach-quality sand equal to $5 and $30, respectively. Even at profile spacings as small as 50-m, the cost error is as great as $100/m. As the profile spacing increase to 100 m or greater, the cost error becomes as great as $325/m, translating to a total project cost difference well over $3 million. With renourishment at $22 to $26 per cubic meter occurring annually at Presque Isle, higher density surveys are certainly warranted. Typical monitoring at profile spacings of 300 m or greater may result in costs differentials around $2.5 millions over the project length.

This investigation indicates the economic and planning benefits of high-resolution ALB for beach nourishment along irregular beaches. Low-density data may result in gross miscalculation of fill volumes, ultimately impacting project performance and financial management. Prior to ALB, no other survey method could

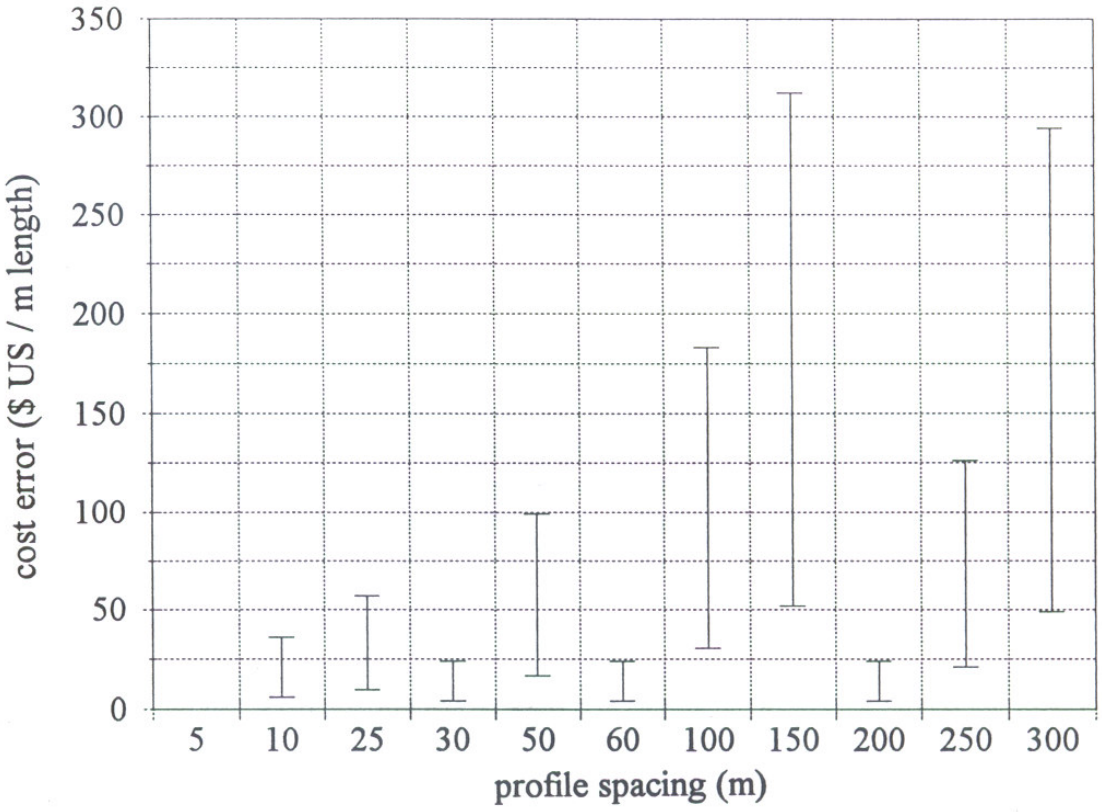

Figure 2.27 Cost error at Presque Isle, PA (from Irish et al., 1997).

be practically used to collect such survey sets. As such, ALB provides coastal engineers with a unique tool to improve beach nourishment practices.

2.6 Storm Response: Hurricane Opal

ALB systems are an ideal technology for quickly assessing and quantifying storm impacts in coastal areas. This section describes the use of the SHOALS system to assess impacts following landfall of Hurricane Opal along the Florida panhandle (Irish et al., 1996).

While this part of Florida has been subjected to tropical storms in the past, Hurricane Opal appeared to be more destructive than most. Initial reports stated that tremendous overwash occurred causing extensive dune and property damage throughout the panhandle. Because of the estimated damage in the area, there was a need to quickly assess bathymetric changes resulting from Opal in two critical areas, Panama City Beach and East Pass (Figure 2.28).

In light of the magnitude of Hurricane Opal and the initial reports of extensive damage, ALB surveys were requested to assess post-storm geological impacts at Panama City Beach and East Pass. Of particular concern were the identification of hazardous shoal formations in the federally maintained navigation channels of East Pass and the extent of beach erosion at Panama City Beach. Chapter 2.6 presents two ALB post-storm surveys, one at Panama City Beach and one at East Pass, and summarizes the impacts of Hurricane Opal on these sites.

The ALB post-storm surveys collected for this study were the first ALB surveys collected for emergency response. These surveys demonstrate the unique capability of ALB for rapid response following natural disasters. There is no other survey technology that is capable of rapid and accurate bathymetric survey collection.

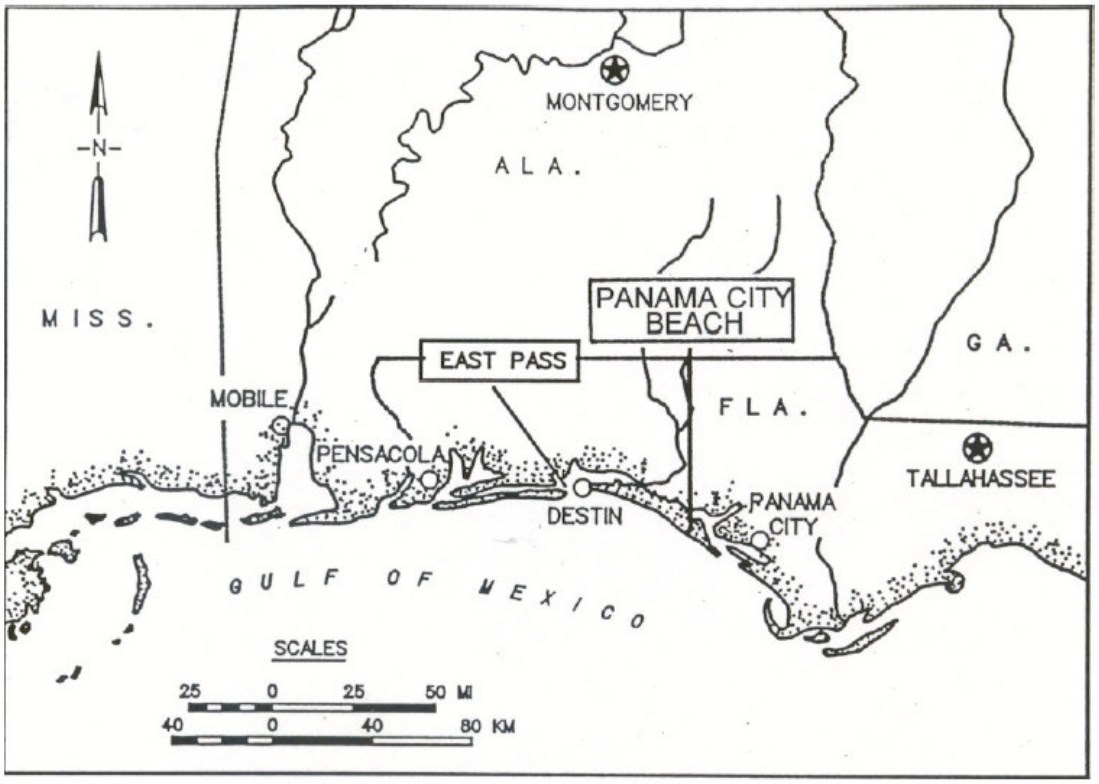

Figure 2.28 Florida panhandle indicating Panama City Beach and East Pass (from Irish et al., 1996).

2.6.1 Hurricane Opal

At 1700 CDT on 4 October 1995, Hurricane Opal made landfall on the western Florida panhandle. The eye passed west of East Pass making direct landfall on Santa Rosa Island near the town of Mary Ester (Figure 2.29). Hurricane Opal generated winds up to 67 m/s, classifying it as a Category III storm. The following statistics summarize the storm:

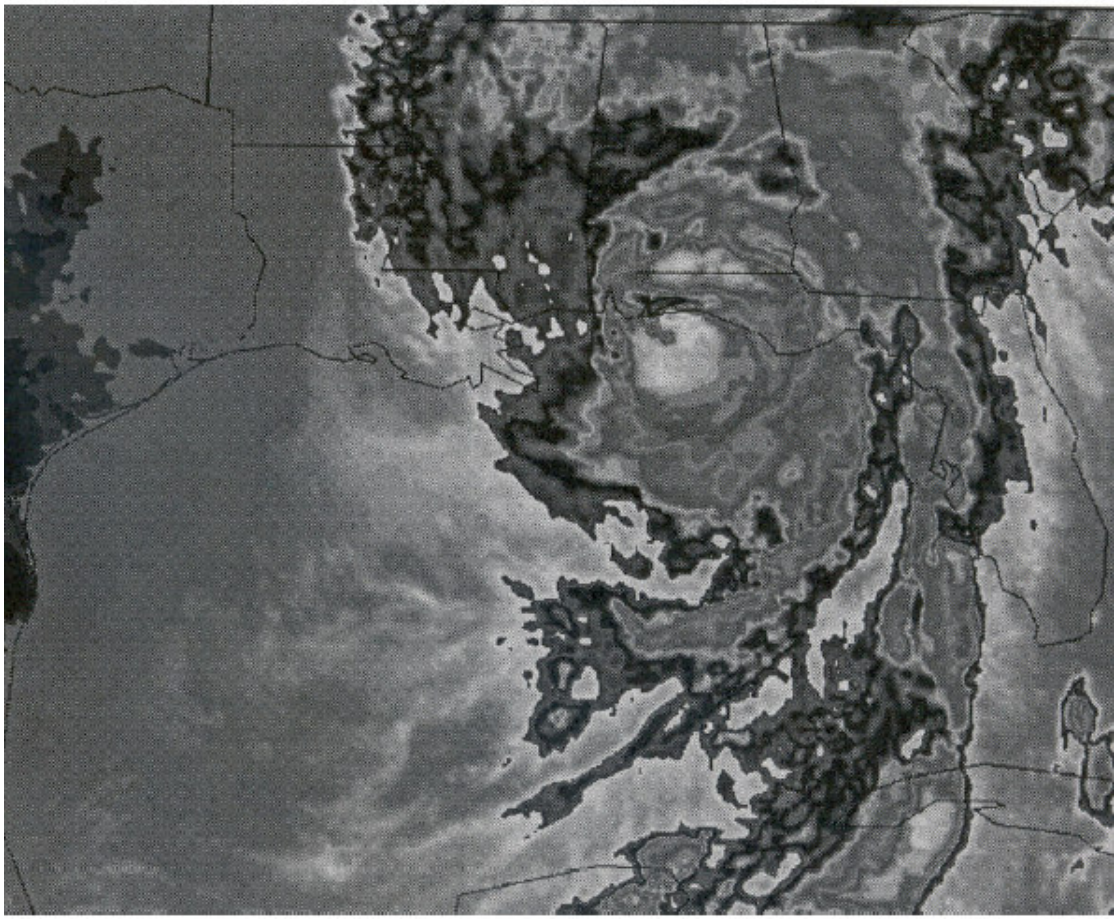

Figure 2.29 Infrared satellite image of Hurricane Opal at 1300 CDT, 4 October 1995 (from Irish et al., 1996).

Minimum Barometric Pressure	916 mb
Maximum Wind Speed	67 m/s
Maximum Storm Water Level	4.5 m (14.8 ft) NGVD29

During the storm, a 4.5-m (14.8-ft) storm water level pushed a tremendous amount of water through East Pass and across Panama City Beach. As a result, most of the coastal damage from Opal was caused by storm surge rather than from winds.

2.6.2 Panama City Beach, FL

Panama City Beach, located on the Gulf of Mexico, extends eastward 29 km from Philips Inlet to the Panama City Harbor entrance (Figure 2.28). The beach consists of fore-dunes, subject to erosion, fronting another line of dunes stabilized by vegetation. Panama City Beach has been predominantly erosive with the eastern most 5 km eroding at approximately 0.6 m/yr, and the entire stretch of beach is heavily developed both with commercial and private structures. Because the area is at risk for storm-induced damages, the USACE developed a beach fill plan in 1994; however, the fill project had yet to be initiated prior to October 1995.

Historic data exists for Panama City Beach, most of which was collected by conventional beach profiling methods. Prior to Hurricane Opal, the most recent and complete survey of Panama City Beach was performed in early April 1995. Conventional profile data were collected at 300-m intervals along the shoreline in depths from 0 m (0 ft) to 14.5 m (47.6 ft). A two-dimensional representation of the western-central 7 km of this data set along with the profile locations are given in

Figure 2.30a. As the figure shows, the pre-storm profiles indicate this area is uniform alongshore with shore-parallel depth contours. The most prominent feature is the nearshore bar formation with a 1.8-m (6.0-ft) rise located at the 3.7-m (12.0-ft) depth contour. Seaward of this feature, the nearshore slope is 1:45.

For this study, bathymetric data immediately following the storm were collected and analyzed to assess nearshore morphological storm response. The SHOALS system arrived in Florida five days after Hurricane Opal made landfall, and a survey of the 29 km of Panama City Beach was performed on 14 October. The survey, completed in less than 3 hours, included over one million individual depth soundings and covered an 18-km^2 area extending to the 11-m (36-ft) depth contour. Figure 2.30b gives a two-dimensional contour representation of a 7-km section located in the western-central part of the survey area.

The SHOALS bathymetry indicates that, after the storm event, the area is still uniform alongshore in most areas. However, just east of Profile 42, there is a scour hole running in the cross-shore direction (Figure 2.30b). A 60-cm diameter drainage pipe outflows directly onto the beach in this location resulting in this scoured area. This feature is not evident in the April profile survey; however, it is unclear whether this feature is solely a consequence of Hurricane Opal or if the feature pre-existed but was not represented by the widely spaced profile data collected in April. Since SHOALS is capable of collecting data at a 4-m spatial resolution, the details of this feature are clear, as illustrated in the three-dimensional view of the area given in Figure 2.31. It is probable that this scour feature existed prior to the storm event, but it is likely to have spread and deepened because of the amount of precipitation and overwash associated with this storm.

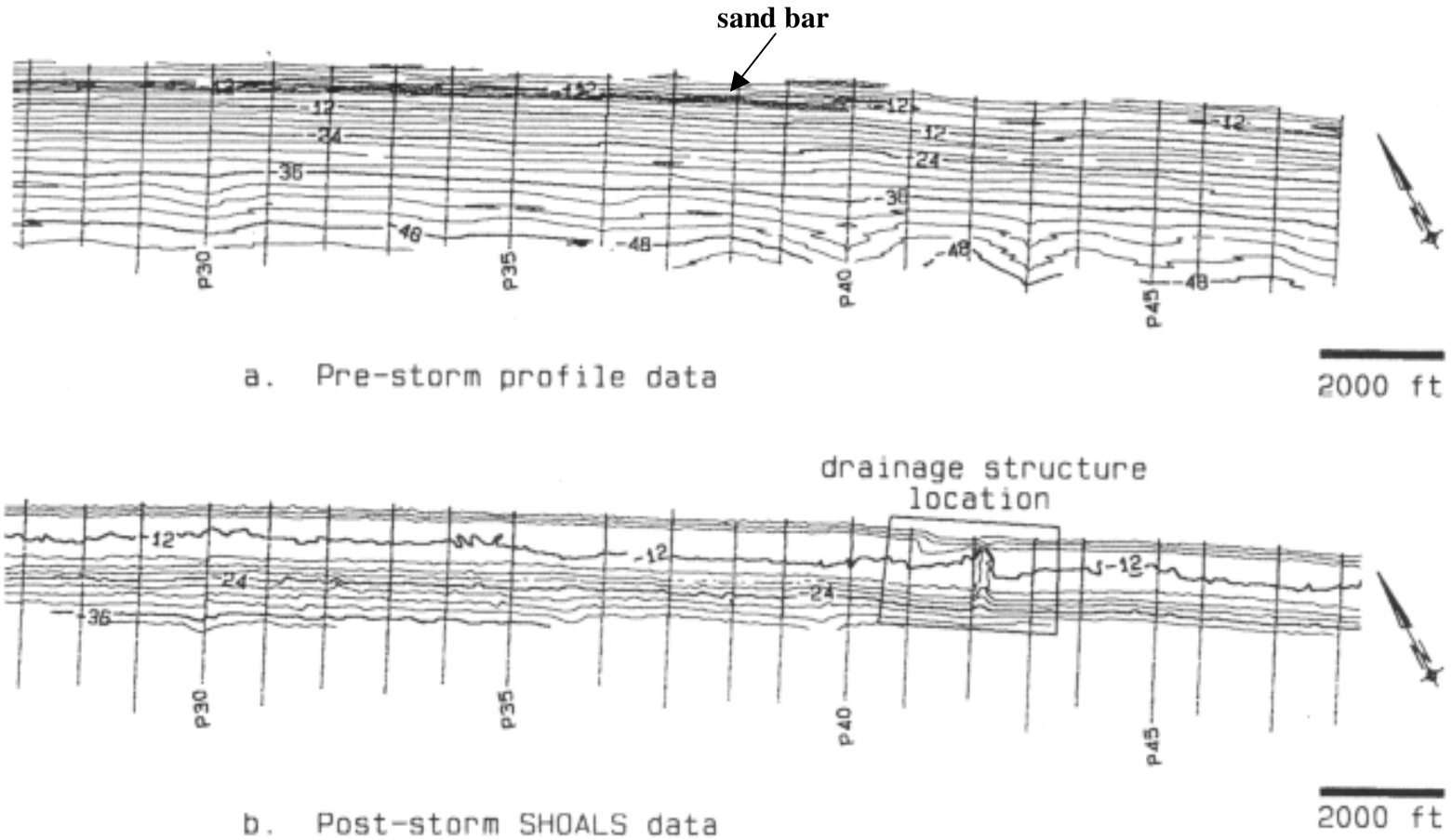

Figure 2.30 **Pre-storm and post-storm bathymetry at Panama City Beach, FL (7 km along-shore; depths are in feet referenced to NGVD29; 1 ft = 0.3048 m; from Irish et al., 1996).**

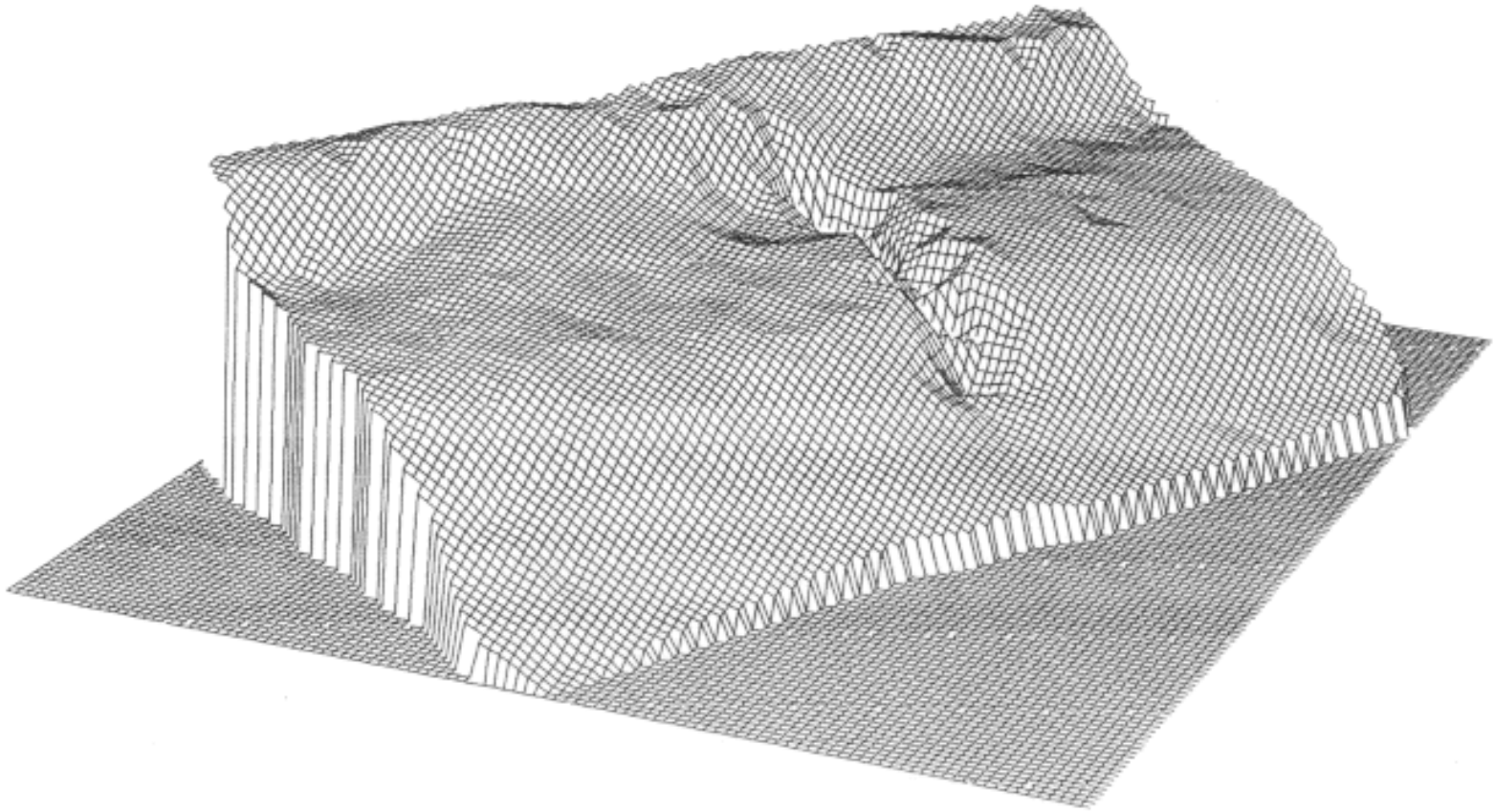

Figure 2.31 Three-dimensional view of scour formation at Panama City Beach, FL (location is shown in Figure 2.30b; east is to the right; from Irish et al., 1996).

Several changes in the cross-shore shape of the nearshore resulting from Opal are evident from the SHOALS bathymetry. For this study, the SHOALS data were compared with the April profile data. Representative cross-sections through both the April profile data and the SHOALS bathymetry at the location of Profile 32 is given in Figure 2.32 to further illustrate these changes. The profile cross-sections through the two data sets show that the nearshore bar formation present in the April survey has been flattened by the hurricane and that sediment moved mostly offshore. As a result of the storm, the nearshore slope became steeper, 1:40, signifying the large wave conditions associated with a major storm event such as Hurricane Opal. The profiles throughout the survey indicate that depth of closure for this storm event was at the 11.6-m (38.1-ft) depth contour, past which little bathymetric change occurred. The figures also show some accumulation of sediment in depths shallower than 3 m (10 ft). This accumulation may be an indication of profile, or nearshore, recovery during the ten days between landfall of Hurricane Opal and the SHOALS survey.

Elevation differences between April 1995 and the post-storm ALB survey in October 1995 are given in Figure 2.33, where black indicates negative depth change (erosion) and light grey indicates positive depth change (accretion). The flattening of the nearshore bar as a result of the storm is again illustrated by the erosive (black) strip seen in Figure 2.33; this erosive strip also indicates the previous location of the bar. Similarly, the movement of material onto the offshore portion of the beach profile is indicated by the accumulative (light grey) area adjacent to the previous bar location.

Volumetric change over the entire survey area, below the waterline, was calculated as a net accumulation of 4.6 million m^3, or 159 m^3/m along shore. Visual observations immediately after Hurricane Opal indicated extensive erosion to the

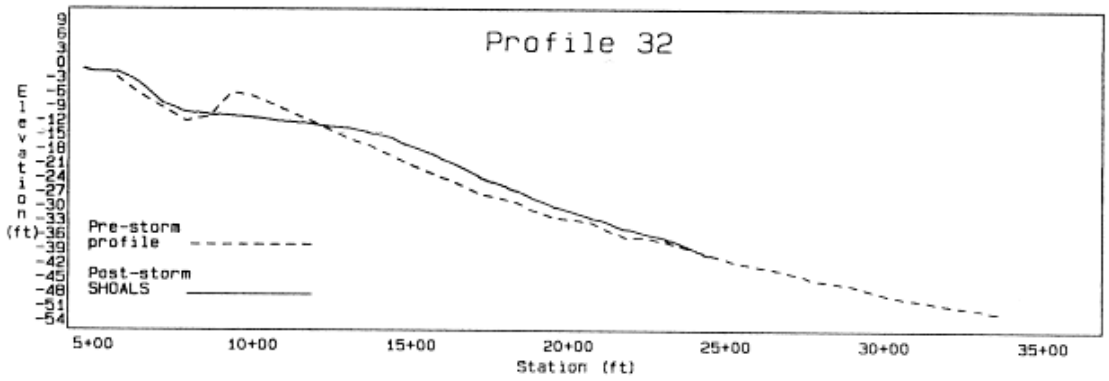

Figure 2.32 Representative pre-storm and post-storm profiles (Profile 32 as seen on in Figure 2.30; depths are in feet relative to NGVD29; 1 ft = 0.3048 m; from Irish et al., 1996).

upland beach and dune system throughout the survey area. While some of this material was undoubtedly moved further onto land or into the back bay, it is probable that a large proportion of this material was moved offshore, but shoreward of the 11.6-m (38.1-ft) depth contour.

2.6.3 East Pass, FL

East Pass, the only direct entrance from the Gulf of Mexico into Choctawhatchee Bay, is located on the northwest coast of Florida 72 km east of Pensacola and 80 km northwest of Panama City (Figure 2.28). The inlet is jettied on both the east and west sides. In addition, the east side has a spur jetty added to its landward end to divert tidal currents. The pass lies between Santa Rosa Island to the west and Moreno Point to the east. The 6.5 km of beach to the west of the pass is part

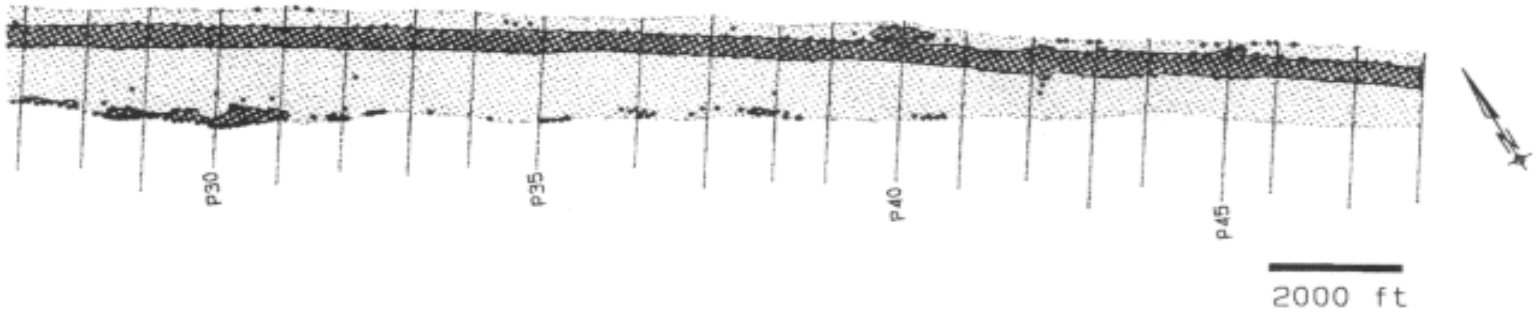

Figure 2.33 **Depth change between pre-storm and post-storm surveys at Panama City Beach, FL. Light grey indicates accretion and black indicates erosion (7 km along-shore; depths are in feet referenced to NGVD29; 1 ft = 0.3048 m; from Irish et al., 1996).**

of Eglin Air Force Base and is mostly undeveloped. On the east side of the pass near the jetties is a sand spit, known as Norriego Point, which formed in 1935. This spit and the low beach immediately to the east have been developed with condominiums, roads, and canals since the 1970s (Morang, 1993).

Prior to Hurricane Opal, the most recent hydrographic survey of East Pass was conducted in February 1990 by conventional multibeam acoustic methods. Morang (1993) presents a summary of the morphological conditions at this time based on this survey as well as historical information:

- The channel hugged the inlet's east shore (Norriego Point).
- Significant scour had occurred at the tip of the west and the spur jetties.
- The primary navigation channel crossed the ebb shoal in a southwest orientation; however, in the early 1990s its orientation became more north-south.
- The east jetty was in danger of being flanked due to persistent erosion in the area immediately north of the spur jetty.

On 10 October 1995, SHOALS performed an ALB survey of East Pass for this study. The SHOALS mission was completed in less than one hour and included nearly 300,000 individual depth soundings over a 2.6-km^2 area (Figure 2.34). The SHOALS bathymetry ranges in depth from land to 9.1 m (29.9 ft) and covers the area near Norriego Point, the inlet throat, and the ebb shoal.

In this study, the morphological changes resulting from this storm were assessed by analyzing the SHOALS data and comparing it with the 1990 conventional survey. From the SHOALS bathymetry, several morphological changes due to

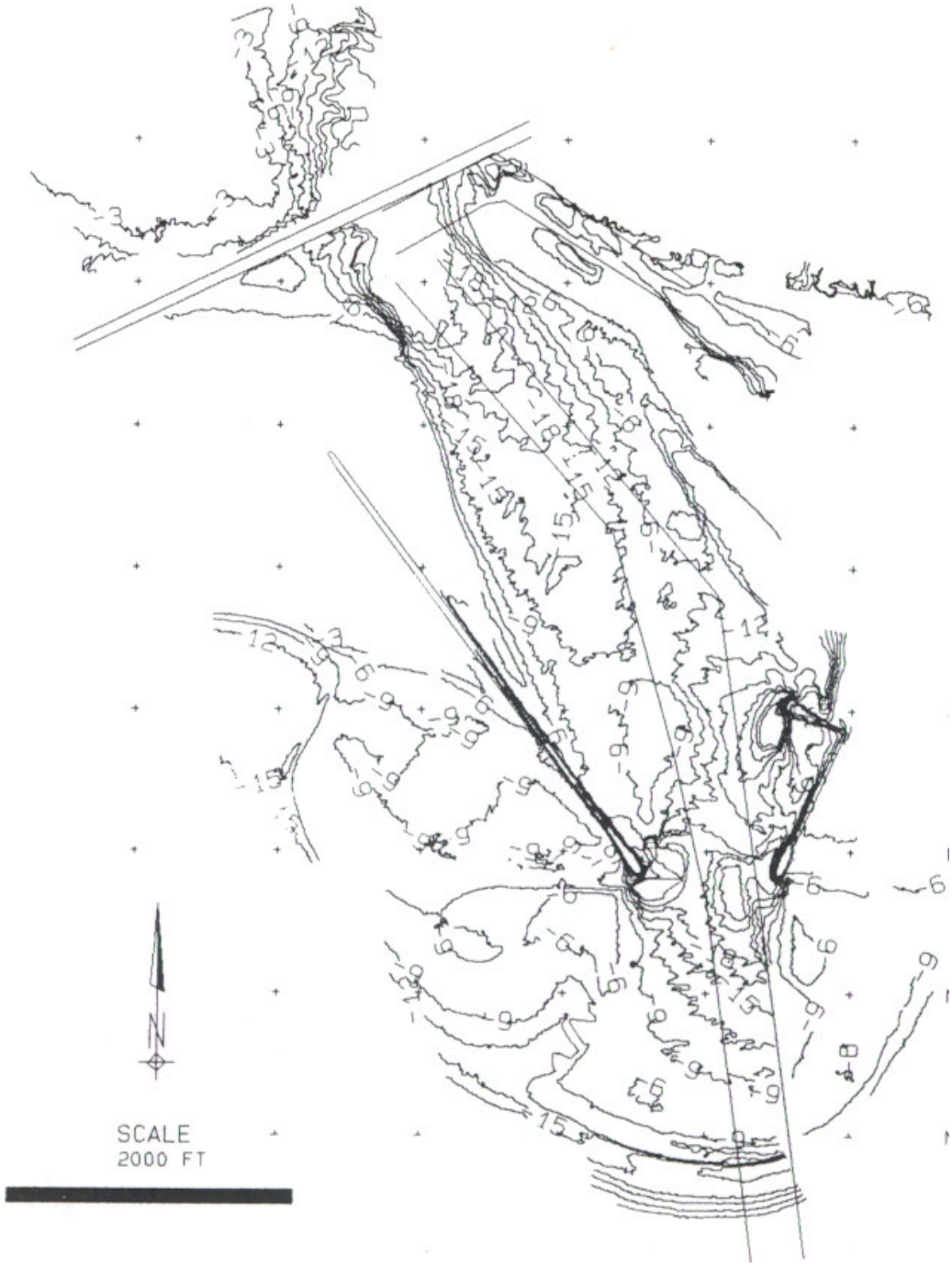

Figure 2.34 Post-storm SHOALS bathymetry at East Pass, FL. Depths are in feet referenced to NGVD29 where 1 ft = 0.3048 m (from Irish et al., 1996).

Hurricane Opal were apparent. The aerial photograph taken of East Pass immediately after Hurricane Opal helps in illustrating these changes (Figure 2.35). There are three obvious changes resulting from the storm surge associated with Hurricane Opal. First, a narrow overwash fan projects into East Pass near the west end of the highway bridge where the barrier island was low and provided little resistance to overwash. Second, almost half of the west jetty was overwashed, with sand being carried from Santa Rosa Island into the navigation channel. Third, Norriego Point was breached just northwest of the condominiums. The USACE, after conducting a post-Opal reconnaissance, estimated that about 80 percent of the above-water portion of the point was removed (Robinson, 1995). This breach is particularly clear in Figure 2.35.

The conventional acoustic survey data collected in 1990 was compared with the SHOALS data to assess overall changes to the inlet. Figure 2.36, representing depth changes at East Pass between February 1990 and October 1995, reveals a number of changes that have occurred. First, a zone of erosion cuts through the ebb shoal from between the jetties. However, it is difficult to distinguish the effects Hurricane Opal had on this area from the effects caused by the natural channel realignment occurring over this 5-year period where there is a lack of hydrographic surveys.

Within the inlet, up to 3 m of erosion occurred in the zone east of the west jetty, while the east half of the inlet accreted, and further north, just south of the highway bridge, the primary navigation channel scoured to over 1.5 m in places. A large amount of sand accumulated just north of the spur jetty causing infilling of the primary navigation channel (Morang et al., 1996). Using the SHOALS bathymetry, it was determined that nearly 46,000 m^3 of material required removal from this section

Figure 2.35 Aerial photograph of East Pass, FL after Hurricane Opal (north is to top; from Irish et al., 1996).

Figure 2.36 Depth change between pre- and post-storm surveys at East Pass, FL. Depth changes are in feet where 1 ft = 0.3048 m. Areas of accretion are in grey and areas of erosion are in black (from Irish et al., 1996).

of the channel to maintain safe navigation. Further, accumulation occurred in the secondary navigation channel section just south of the highway bridge in the northeastern most portion of the survey area. From the SHOALS data, it was determined that over 23,000 m^3 of material required removal from this channel section to maintain navigable depths.

In November 1995, the SHOALS system returned to East Pass and conducted a second survey. By early November, 76,000 m^3 of material had been dredged from the navigation channels and disposed of at Norriego Point. Due to manmade action, the Norriego Point breach is repaired and the federally maintained channels are again navigable (Morang et al., 1996). The use of SHOALS at East Pass allowed for rapid data collection, quick assessment of overall conditions at the inlet, and engineering computations such as required dredge volumes, all within one day. At Panama City Beach, SHOALS rapidly assessed nearshore bathymetric changes resulting from Hurricane Opal. With the high-density coverage provided by SHOALS, irregular features such as the scour formation near the drainage outfall were identified. ALB provides a unique capability for quickly assessing major coastal storm damage making it an ideal tool for emergency management.

2.7 Regional-Scale Mapping

Because ALB systems can rapidly cover large coastal areas, regional-scale surveys along the coastline are now feasible. These surveys can fully map the nearshore to depths of 60 m, depending on water clarity, as well as the adjacent subaerial beaches. The following section illustrates two such regional surveys collected for this study. These two surveys were the first regional high-resolution

bathymetric data sets to characterize the coastal zone. No other survey technology can practically collect these types of detailed regional surveys.

2.7.1 The Hawaiian Islands

Between February and April 1999, the SHOALS system was deployed to the Hawaiian Islands to conduct bathymetric and topographic surveys in support of the State of Hawaii and USACE Hurricane Evacuation Study (HES) and the USGS coral reef mapping and monitoring initiatives (Wozencraft et al., 2000). During the 2-month deployment, SHOALS conducted 60 survey flights totaling 215 operational in-flight hours and resulting in more than 25 million soundings and elevations. The surveyed coastlines are shown in Figure 2.37 (Irish, 2000).

SHOALS mapped the entire Maui and Kauai coastlines, 200-km and 150-km respectively, specifically to generate a detailed digital terrain model (DTM). The SHOALS data, collected with an 8-m horizontal spot density, extended from the upland terrain through the 30-m depth contour. Because of the highly complex nearshore and upland topography characteristic of the Hawaiian Islands, an accurate DTM is essential for successful numerical model predictions.

Along the Maui coastline are numerous natural headlands and coves (Figure 2.38). In addition, areas of rock outcropping and coral reef systems are prevalent in the nearshore. These irregular features impact the spatial variation in hydrodynamic properties like wave refraction and setup and sediment transport. Along with the SHOALS data collected in Kauai, the USACE and State of Hawaii are presently using the SHOALS data collected in Maui to generate baseline regional-scale

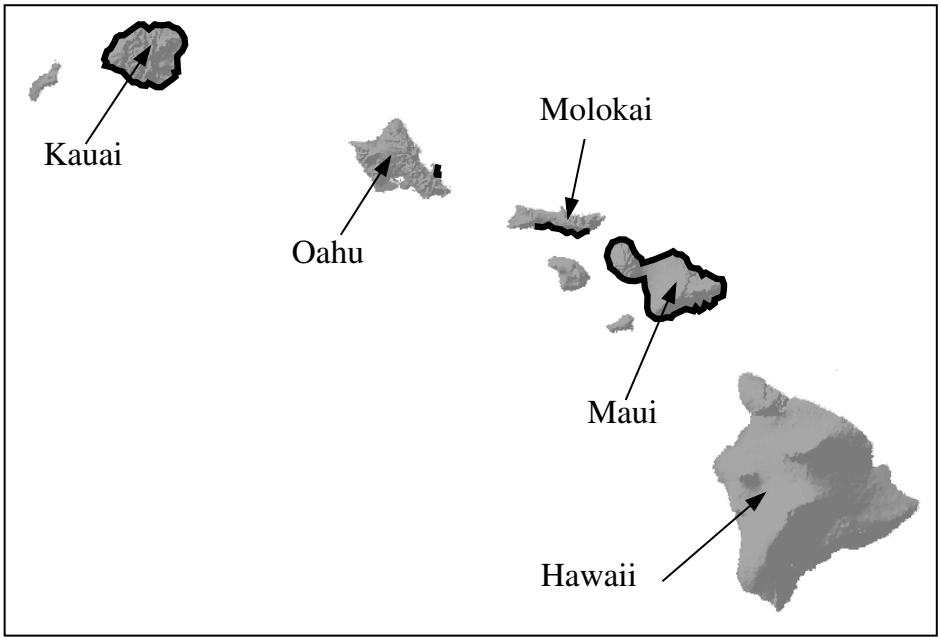

Figure 2.37 Hawaiian Islands coastlines surveyed with SHOALS (shown in black) in 1999 (from Irish, 2000).

DTMs for numerical model simulations of hurricane and tsunami flood inundation to support the HES (Wozencraft et al., 2000).

In 1993, the USGS began using airborne remote sensing to map and study the coral reefs of Molokai, Hawaii. The USGS is using both digital aerial photography from 1993 and 2000 and SHOALS bathymetry from 1999 to map and track changes of coral reef features like short-term seasonal and long-term changes in elevation and elevation features (Chavez et al., 2000). Figure shows SHOALS bathymetry collected in Molokai. These data extend from the shoreline through the shallow waters of the nearshore to depths greater than 7 m.

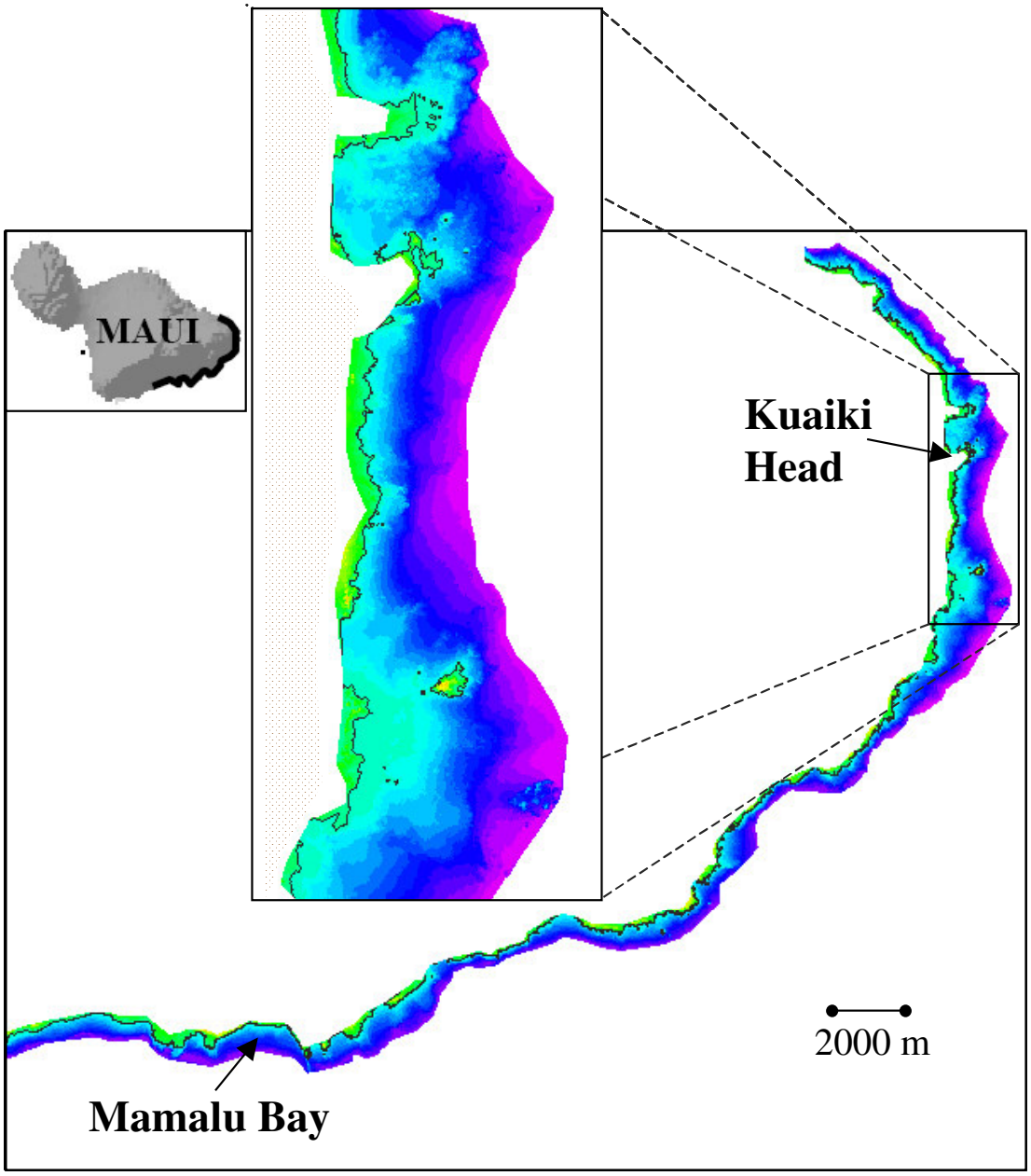

Figure 2.38 SHOALS data at Maui, HI. Shoreline is black line. Depth contours are every 3 m. North is to top (from Irish, 2000).

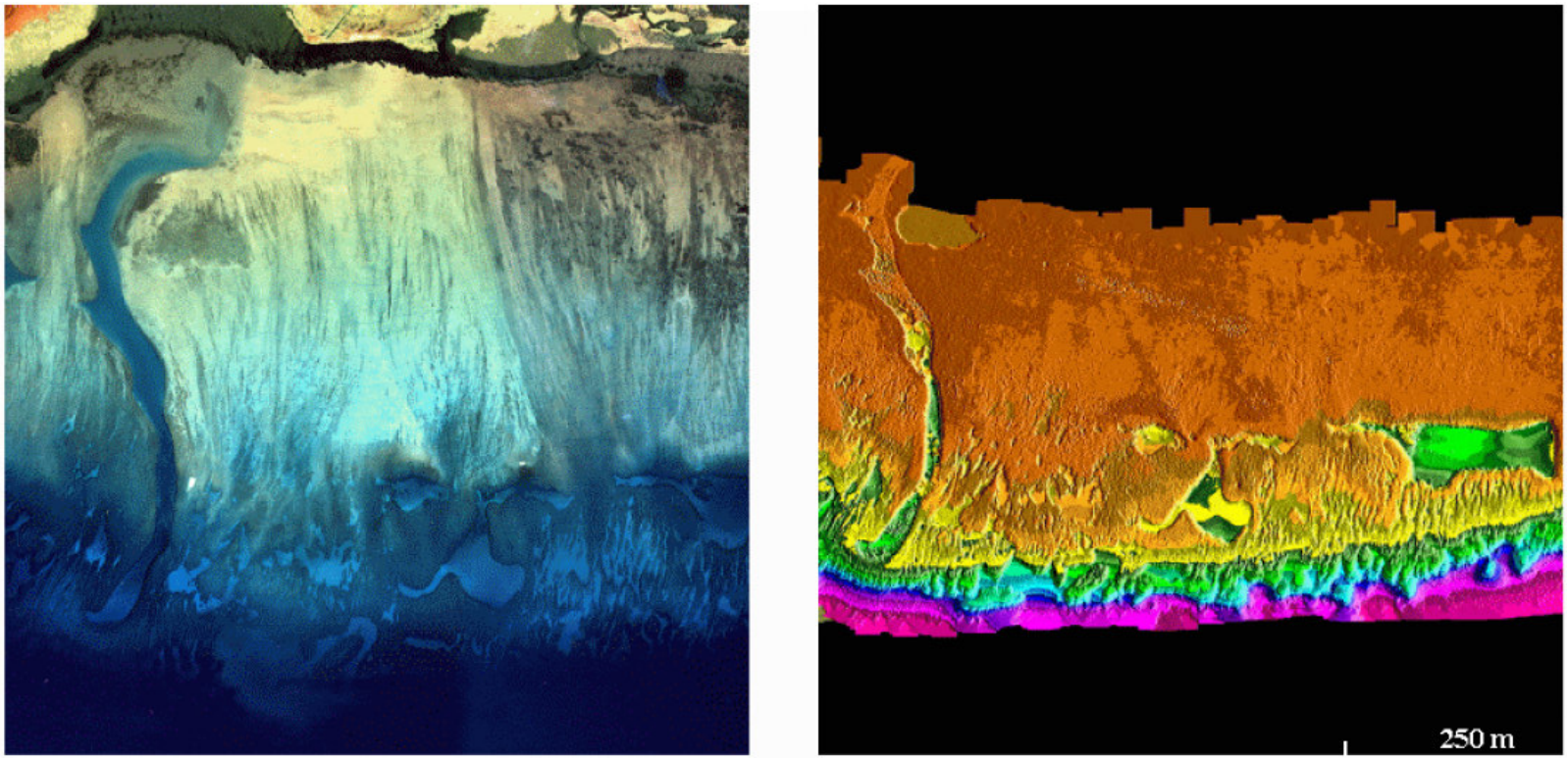

Figure 2.39 **Image of SHOALS data (right) and aerial photograph (left) at Molokai, HI created by USGS (modified from Wozencraft et al., 2000). Shoreline is to top and offshore to bottom.**

2.7.2 The Gulf of Mexico: Surveys to Support Regional Sediment Management

In the late 1990s, the USACE initiated a Regional Sediment Management Demonstration Program (RSMDP) (Wozencraft and Irish, 2000). The RSMDP encompasses 360 km of Gulf of Mexico shoreline stretching from the west end of Dauphin Island, AL east to Apalachicola Bay, FL (Figure 2.40a). The demonstration region encompasses nine federal navigation projects and one federal beach nourishment project. Reliable and effective sand management and engineering requires DTMs that fully represent the study region. In complex coastal areas, high-resolution bathymetric and topographic coverage is essential for reliable calculation of sand volumes, as demonstrated in Chapter 2.5. The SHOALS system surveyed the entire Florida panhandle to support this RSMDP program in 1999. Figure 2.40b shows the extent and detail provided by this survey.

Subsequent SHOALS surveys were collected in the RSMDP region since 1999. The 1999 data set along with the more recent data sets have been used in developing hydrodynamic model grids and in quantifying morphological processes along the panhandle (Wozencraft, personal communications and Lillycrop, personal communications).

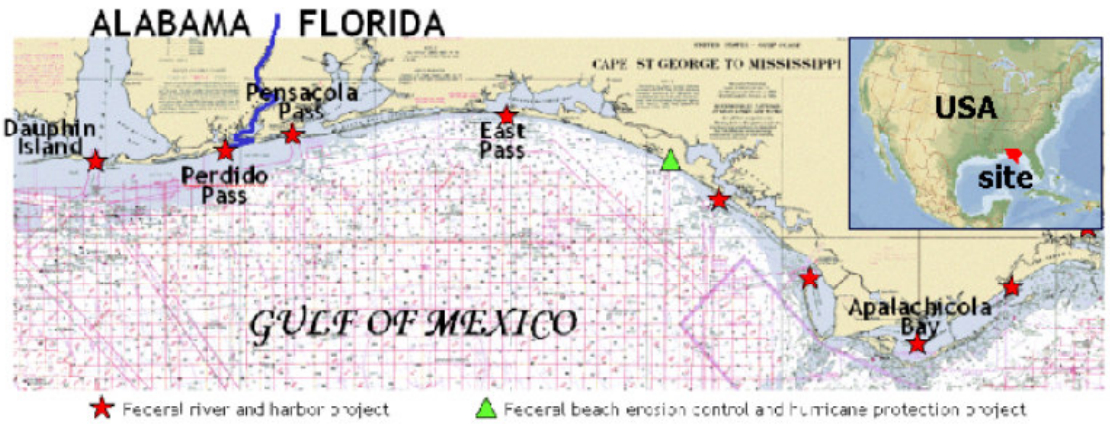

(a)

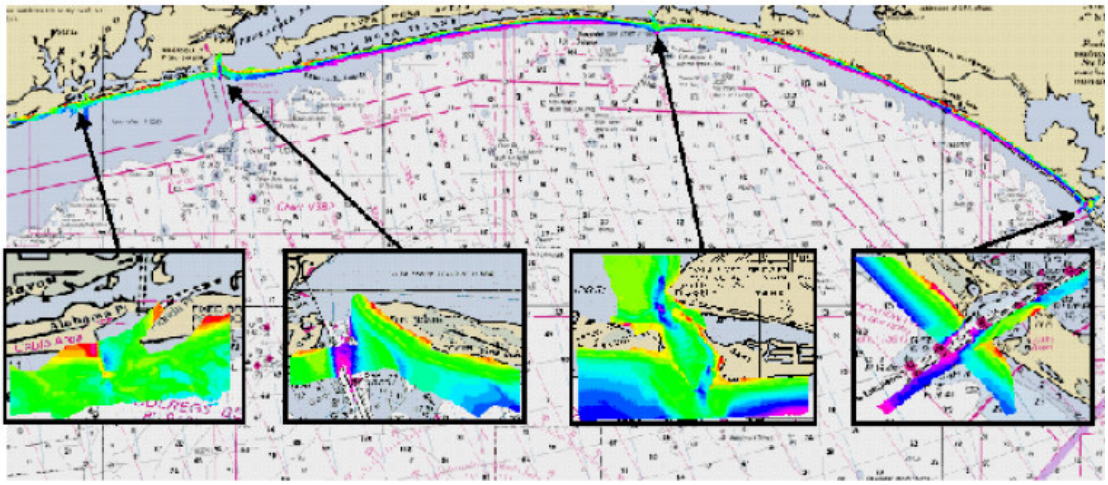

(b)

Figure 2.40 RSMDP (a) area and (b) DTM generated from SHOALS data collected in 1999 (north is to the top; from Wozencraft and Irish, 2000).

Chapter 3

FIXED-PLATFORM LIDAR FOR WAVE MEASUREMENT

The intent of the investigation presented in this chapter is to further expand the application of lidar for long-term measurement of water waves from fixed platforms in coastal environments. Work by Ross et al. (1970) and Hwang et al. (1998) have demonstrated that lidar may be used successfully to monitor ocean waves from an aircraft. Moreover, Ross et al. (1968) demonstrated that non-directional wave spectra could be successfully measured with a nadir-looking fixed lidar. However, lidar technology for measuring directional wave spectra from a single fixed platform has yet to be attempted.

In December 1999, a non-intrusive directional Lidar Wave Gage (LWG) was field tested at USACE Field Research Facility (FRF, Figure 3.1) in North Carolina (Irish et al., submitted; Irish et al., 2000b; and Irish et al., 2001). The prototype LWG consists of four rangefinders. Each rangefinder collects water surface elevation time series at a rate of 10 Hz. During the field experiment, ground truth data were collected concurrently with the LWG data using a biaxial current and pressure gage (PUV) mounted directly beneath the LWG. In addition, existing wave measurement infrastructure at the FRF provided other ground truth measurements. Directional-spectral wave characteristics determined from the LWG time series using slope array analysis procedures match well with ground truth results.

The LWG design and field testing are fully described in this chapter. The following section describes the history and status of remote sensing technologies for

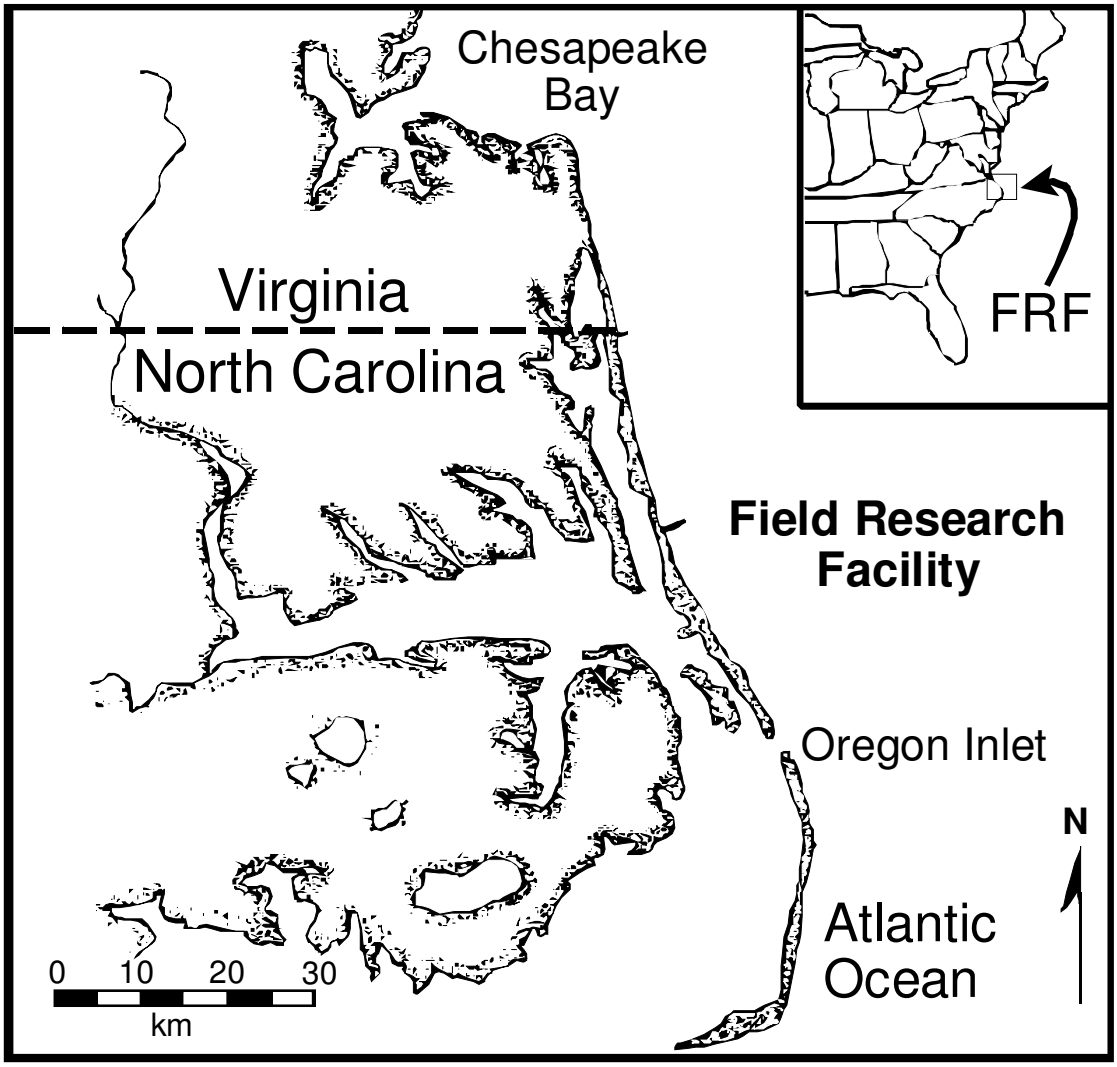

Figure 3.1 Location of FRF, Duck, NC.

measuring ocean waves. Subsequent sections then detail the sensor design, field testing, and findings from the current LWG investigation.

3.1 History of Non-Intrusive Wave Measurement–A Literature Review

Field measurement of ocean waves with remote sensing methods has evolved over the last 50 years. These methods include such technologies as photogrammetry, radar, video, and lidar. The following sections provide a summary of each of these technologies.

3.1.1 Radar Methods

The bulk of remote ocean wave measurement investigations and applications over the last several decades have been with the use of radar methods. The following sections describe the theory upon which radar is used to measure the ocean surface as well as methods used to extract wave characteristics.

3.1.1.1 Radar Theory

Dean (1982) and Driver (1985) detail radar theory, and this section provides a summary of these papers. Following pioneering work by Rice (1951) and Crombie (1955) showing the means by which electromagnetic energy is backscattered by rough surfaces like the sea surface, fixed, airborne, and space-borne radar systems have been developed to monitor wave characteristics. These radar systems measure wave characteristics including wave height, frequency, and direction by measuring electromagnetic backscatter by Bragg scattering and specular reflection (Figure 3.2).

Specular reflection is the process by which energy is reflected back to the system's receiver via direct reflection from surfaces perpendicular to the energy source. Consequently, energy returned by specular reflection is measured

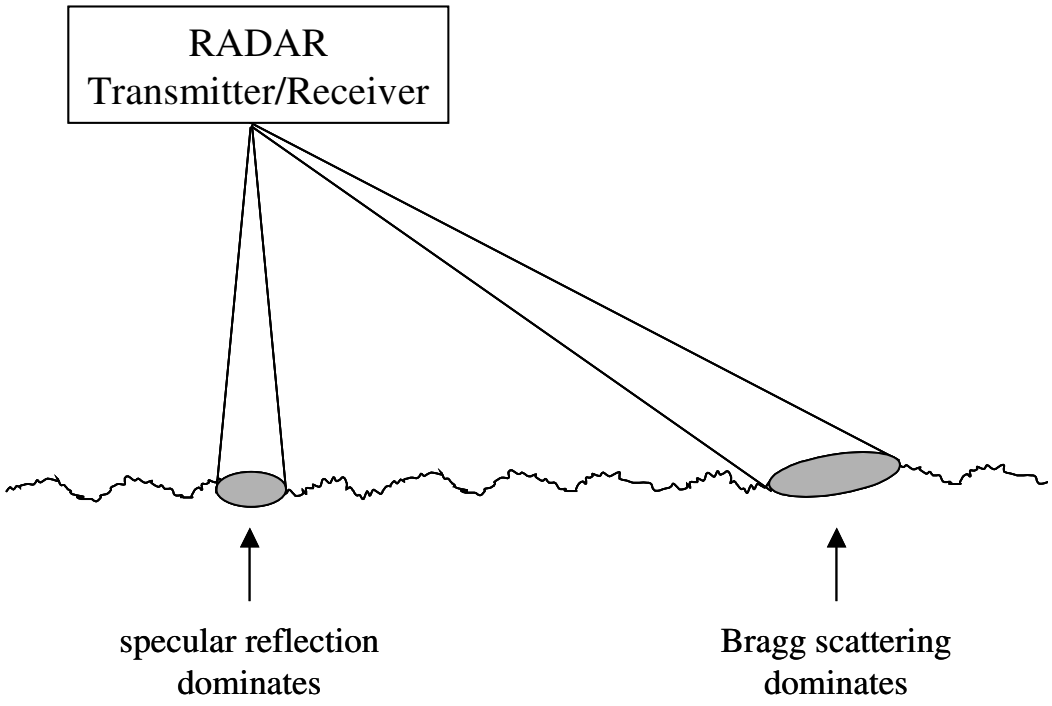

Figure 3.2 Electromagnetic backscattering (modified from Driver, 1985).

by directly downward-looking, or nadir, radar systems. In practice, specular reflection is seldom used to measure ocean wave characteristics because hardware constraints result in radar footprint sizes too large for meaningful direct ranging of sea surface waves.

Since the ability to detect specular reflection dramatically diminishes as incident angle is increased, radar systems that operate at angles significantly off of nadir must rely on Bragg scattering. Bragg scattering is produced by surface waves. Specifically, Bragg scattering from the ocean results in energy reflected back to the source that is amplified by the presence of surface wind waves. Strongest Bragg

scattering returns coincide with ocean waves that propagate in the direction of the radar source and are characterized by resonant wavelengths equal to one-half the transmitted radar wavelength (Driver, 1986).

Backscattered energy signals received by radar systems may be analyzed to extract ranging ocean surface distances and velocities. Distance between the radar source and the sea surface is directly related to the time required for the radar signal to travel from the transmitter to the sea surface and back. The ranging distance is directly proportional to the travel time and follows the same relationship given for lidar in Equation 2.1.

The radar backscatter will exhibit Doppler shift as a result of the relative difference in velocities between the ocean surface and the radar sensor. This Doppler shift provides a means for extracting water surface velocity. Therefore, the velocity of the ocean surface relative to the radar sensor, $V_{relative}$, is:

$$V_{relative} = \frac{\lambda f_{Doppler}}{2} \tag{3.1}$$

where:

λ is the radar wavelength

$f_{Doppler}$ is the Doppler frequency shift

3.1.1.2 Determination of Wave Characteristics

Most radar systems rely on receiving Bragg scattering to extract wave characteristics, and, as such, the discussion below focuses on Bragg scattering analysis

methods. By inverting the measured Doppler frequency spectrum, directional energy spectra may be computed. Derivation of ocean wave spectra from radar Doppler spectra was first introduced by Hasselmann (1971) and Barrick (1972a and 1972b) with advancements and improvements shortly thereafter by Barrick (1977), Lipa (1977), Alpers and Hasselmann (1982), Young et al. (1985), and Lipa and Barrick (1986). In general, the inversion to an ocean wave spectrum is a function of the ratio between the Doppler spectrum's second- and first-order energy bands (Figure 3.3).

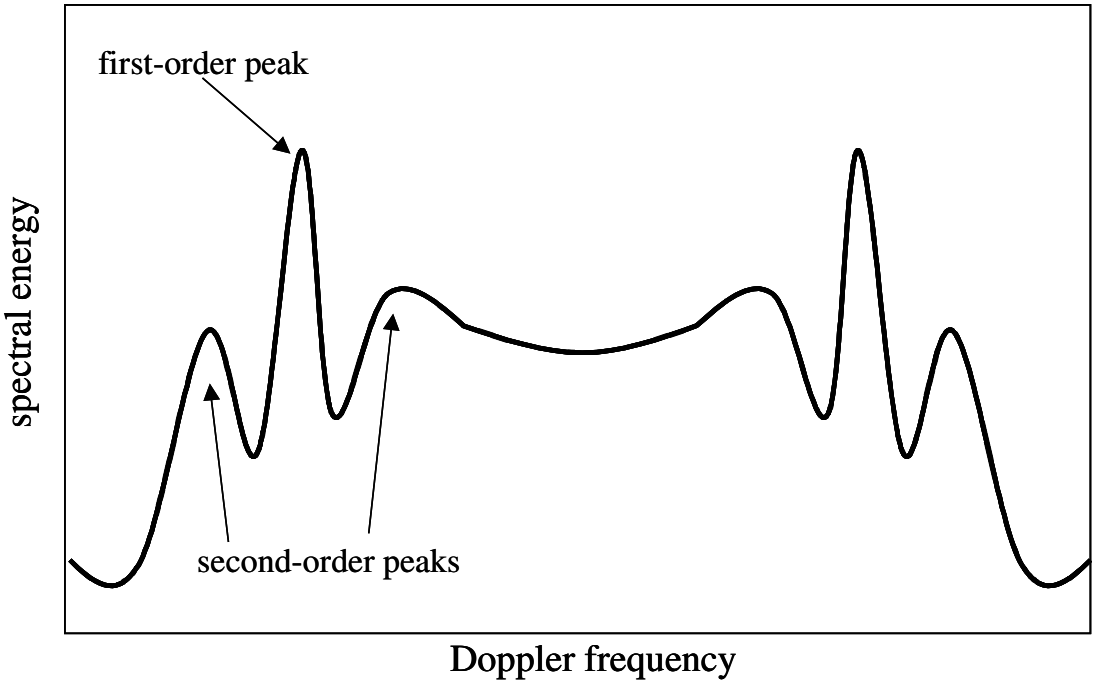

Figure 3.3 Idealized Doppler spectrum.

From the calculated ocean spectrum, wave characteristics such as spectral wave height, peak period, and peak direction may be extracted. In addition, Alpers and Hasselmann (1982) estimate significant wave height directly from the radar data's signal-to-noise ratio (SNR):

$$H_s = A + B\sqrt{SNR} \tag{3.2}$$

The calibration coefficients A and B are computed via linear regression on the collected radar data and are specific to the sensor's spatial resolution.

Considerable work in developing and improving numerical methods for extracting directional spectra and wave characteristics from radar Bragg scattering has occurred over the last couple of decades. These developments and improvements have been published extensively. Some of the more recent advancements are summarized below.

Forget and Broche (1996) presented a method for removing noise from the radar energy spectra so that inversion to ocean wave spectra provides improved results. The authors identified noise properties in radar data in an experiment in 1990. Finding that the radar image noise was confined in a narrow spectral band, the authors developed a method for removing this noise. Following application of this noise-reduction method, radar energy spectral estimates were altered by as much as 19%.

Lyzenga and Ericson (1998) investigated the influence of sharply peaked ocean waves, such as near-breaking waves, on radar backscatter. Because Melville et al. (1988) and Loewen and Melville (1991) showed a measurable increase in backscattering for near-breaking waves, Lyzenga and Ericson (1998) proposed edge diffraction effects as an explanation. The authors demonstrated that backscatter

contributions from edge diffraction are correlated with wave steepness but are not strongly correlated with wave height. The authors also noted that the influence of edge diffraction on backscatter is linked to radar operating frequency and may be significant only for radar systems operating below 10 GHz.

Bao et al. (1999) derived a new imaging model for the relationship between radar phase information and wave orbital velocity. Based on their imaging model, they developed a nonlinear integral transform relating the radar phase spectra with ocean wavenumber spectra. Their approach provides a direct relationship that eliminates the need for spatial-domain Monte Carlo simulations.

Hisaki and Tokuda (2001) expanded the radar energy Doppler spectra theory developed by Barrick (1972a) to include the effects of Bragg scattering by bound waves and of double Bragg scattering. Their numerical method, that assumes a generalized Stokes wave model, improves spectral prediction from the radar sensor relative to spectra computed from wave data collected with a sonic wave recorder measuring three-dimensional orbital velocity. While the spectral prediction is improved, the authors noted that the numerical method is computationally intensive.

Hashimoto et al. (2003) applied a Bayesian approach for extracting directional wave spectra from radar backscatter, following a similar approach applied successfully to in situ wave gage data in the 1980s (Hashimoto et al., 1987). Directional wave spectra computed from radar backscatter using this new method were compared to spectra computed using other, more widely employed, methods and to spectra derived from wave buoy data. The authors concluded that their approach is valid and applicable to radar backscatter data and that it is more robust than other analysis approaches currently in use.

3.1.1.3 Radar Sensors for Ocean and Coastal Applications

Several operational radar sensors for monitoring ocean and coastal wave characteristics are summarized in this section. Side-Looking Airborne Radar (SLAR) are real-aperture imaging microwave radars that operate from aircraft. SLAR sensors collect ocean surface images by recording Bragg backscatter (Driver, 1985). SLAR sensors collect these wave-pattern images at specific times, and the images are analyzed to determine directional wavenumber spectra without information on wave height.

Synthetic Aperture Radar (SAR) is also an imaging microwave radar, but it uses the technique of synthetic aperturing to improve spatial resolution (Driver, 1985). These sensors operate from aircraft and spacecraft and collect ocean surface images at specific times. Analysis of SAR images provides both directional wavenumber spectra and wave height information.

Interferometric Synthetic Aperture Radar (INSAR) is an improvement on the SAR systems that has evolved since the late 1980s (Goldstein and Zebker, 1987; Goldstein et al., 1989; and Marom et al., 1990). INSAR uses two spatially separated antennas to record radar backscatter. The two images are combined and provide a component of the ocean surface velocity in addition to the radar reflectivity image.

X-Band marine radar images may also be used to extract wave characteristics. The Coastal Wave Imaging Radar, WAMOS, and FOPAIR are three such systems (Driver, 1985; Reichert et al., 1999; Nieto Borge et al., 1999; Hessner et al., 2003; Frasier and McIntosh, 1996; and Frasier et al., 1998). These systems collect ocean surface images of radar backscatter, and may be operated onboard a ship or from a fixed ground-based platform. Because these systems can operate from a stationary platform, images taken through time may be analyzed to determine directional wave

spectra, wave height, wave frequency, wavenumber, and wave direction. Nieto Borge and Soares (2000) reported good agreement between the WAMOS sensor and offshore buoy measurements for wave frequency and direction. In the comparisons presented, WAMOS peak frequency and mean wave direction measurements were within 0.014 Hz and 13 deg, respectively, of those measured by the buoy. The RMS error of the measurements presented is 0.008 Hz and 8 deg in peak frequency and mean direction, respectively.

Doppler radar systems are non-imaging systems that record Doppler shift (Driver, 1985). These sensors may be deployed from fixed and airborne platforms. Coastal Ocean Dynamics Application Radar (CODAR) is one such sensor in use today. Such systems have been used to successfully measure directional wave spectra, wave height, wavenumber, and wave direction.

3.1.2 Photogrammetric Methods

Suhayda and Pettigrew (1977) used photogrammetric methods to measure wave characteristics in the surf zone. In their experiment a set of pre-positioned poles, with incremental vertical markings, were placed in the surf zone. A camera was then used, from a fixed location, to record wave field evolution 18 times per second. From each photograph, wave crest and wave trough elevations were extracted. From these data sets both wave height and wave speed were derived.

3.1.3 Video Methods

Video methods for measuring wave characteristics have been reported by Lippmann and Holman (1991) and Stockdon and Holman (2000). Both present a method by which nearshore wave phase speed is extracted from video intensity data

using an Argus sensor (Aarninkhof and Holman, 1999). The video sensor recognizes individual waves by the video signature from specular reflection of downwelling sky irradiance, for waves seaward of the breaker zone, and by the video signature from diffuse reflection from the white foam generated during wave breaking. Time lapse between video images captures wave evolution.

Lippmann and Holman (1991) performed the first tests of this technique by comparing video signature time series with a pressure gage time series. The authors showed good comparisons between the video imaging method and the pressure gage and concluded that video imaging methods for determining wave characteristics is particularly viable for surf zone waves. Stockdon and Holman (2000) extended the methods employed by Lippmann and Holman (1991) to determine wave phase speed to allow continuous measurement across shore.

Curtis et al. (2002) reported on application of video techniques for measuring wave direction during laboratory experiments. In a very controlled environment, the authors reported good agreement between mean wave direction measured with video techniques and those measured with acoustic Doppler velocimeter probes. Curtis et al. (2002) reported a 4.46-deg RMS error in mean direction measurement for these laboratory experiments.

3.1.4 Lidar Methods

Laser ranging of the ocean surface is a viable way to measure ocean wave characteristics. Lidar has been used successfully to directly range the ocean surface from airborne and fixed platforms since the late 1960s (Ross et al, 1968; Ross et al., 1970; Wu, 1971; and Wu, 1972).

3.1.4.1 Lidar Theory

Water surface elevation is measured directly with lidar by recording the travel time from the transceiver to the ocean surface and back. The distance between the surface elevation and the transceiver is then computed via the relationship given by Equation 2.1. Direct lidar ranging of the sea surface for wave characterization is identical to that used to directly range the sea surface for lidar bathymetric mapping, as presented in Chapter 2.

3.1.4.2 Lidar Sensors for Wave Measurement

The first successful attempts to measure ocean waves with lasers were achieved in the late 1960s by Ross et al. (1968). Ross et al. (1968) deployed a laser wave profilometer, using a red laser, on an offshore tower to directly range the sea surface. This laser wave profilometer employed a Spectra Physics Geodolite laser altimeter. The lidar water surface elevation time series were analyzed in the same manner as in situ water surface elevation time series, using Fourier analysis techniques, to extract non-directional ocean wave spectra. Coincident water surface measurements were made with a resistance wire wave staff, and good agreement between the laser and wire staff time series and non-directional frequency spectra were observed.

Ross et al. (1970) were the first to attempt active remote sensing of ocean waves from an airborne platform with lidar. Their pioneering efforts employed the same laser profilometer used by Ross et al. (1968) to measure ocean waves from a fixed platform. Airborne tests were conducted onboard a NASA research aircraft traveling at an altitude of 200 m. The first data sets were collected in the Atlantic Ocean at 60-m water depths nearby a U.S. Navy research tower from which in situ

measurements were collected using a resistance wire wave staff. Lidar data collected during three 2-minute aircraft tracks nearby the tower were analyzed and compared with data from the fixed wire wave staff. The comparison showed good agreement with spectral wave height within 6% and comparable non-directional spectral shape.

Schule et al. (1971) used an airborne laser profilometer to measure wavenumber spectra. These measurements were collected from flights at a 92-m altitude approximately 175 km offshore of coastal Delaware, creating laser footprints approximately 0.9 m by 4.5 m on the ocean's surface. These lidar data were analyzed to determine wavenumber spectra for wavenumbers ranging from 0.05 m^{-1} to 0.35 m^{-1}.

Liu and Ross (1980) reported successful field deployment of the airborne laser profilometer of Ross et al. (1970). In their investigation, they collected water surface profiles along the entire length of Lake Michigan and along several cross-tracks. The authors demonstrated good comparisons between the wave spectra computed from the laser profilometer data and wave spectra computed from a Waverider buoy. Specifically, the peak wave energy and frequency computed from the laser and Waverider buoy data were very similar.

Tsai and Gardener (1982) investigated the use of laser altimeter return signals for extracting significant wave height. Specifically, the authors presented a method for inferring significant wave height from the received laser waveform shape. The authors noted that the relationship between laser waveform shape and significant wave height is strongly dependent on the laser beam angle, relative to nadir.

In 1998, airborne remote sensing using an airborne topographic lidar mapping system (Krabill et al., 1995) was introduced in several publications (Hwang et al., 1998; Hwang and Walsh, 1998; Hwang et al., 2000a; Hwang et al., 2000b; and

Hwang et al., 2000c). This sensor uses a scanner such that swaths of measurements are collected in the across-track direction. In addition, the elliptical scan pattern used allows collection of two time-lagged sea surface maps. The sensor, onboard a Twin Otter airplane, collects data from altitudes between 400 m and 600 m, and laser spot footprints on the sea surface measure about 0.5 m in both the along-track and cross-track directions. The operating aircraft speed, aircraft altitude, laser pulse rate, and scanner rate result in a lidar footprint spacing of approximately 1.5 m in both the along-track and cross-track directions.

Field testing of this lidar sensor for wave characterization was conducted during the Duck94 and SandyDuck97 field experiments, in the coastal waters of North Carolina. The lidar ocean topography were processed to extract two-dimensional wavenumber spectra using two-dimensional Fourier transform methods. Spectral wave height, peak wavenumber, and wave direction were also extracted from the lidar data. The wave spectral characteristics computed from the lidar data were compared with deepwater buoy measurements and showed good agreement. Since this topographic lidar system's elliptical scanning pattern allows each part of the ocean surface to be measured twice, the two time-lagged ocean topography maps may be analyzed to study the evolution of wave patterns over small time increments. The time lag between the two consecutive maps is about 2 s at the center of the lidar swath. Correlation and coherence were calculated from these time-lagged maps, and the results were used to discern direction of ocean wave movement.

Hwang et al. (2002a) applied the Hilbert-Huang Transformation (HHT) method of Huang et al. (1999) to post-processing of airborne lidar ocean surface topography collected with the lidar system. The intent in using this method was to

account for nonlinear characteristics in the measured nearshore wave fields. The authors examined the lidar data with both the HHT method and the Fourier-based wavelet method to evaluate the cross-shore evolution and energy flux of shoaling waves. The authors concluded that spectra derived from the HHT analyses show potential for revealing nonlinear properties in the measured ocean surface topography.

Hwang et al. (2002b) demonstrated the capability of airborne topographic lidar mapping systems to measure breaking wave characteristics. In this investigation, the authors combined the active lidar ocean topography measurements with coincident passive measurements of surface brightness. By combining these data sets, the phase distribution during wave breaking may be measured.

3.2 Prototype Design

The prototype LWG was designed to meet two objectives: 1) to test the ability of lidar technology, from a fixed platform, to measure directional wave properties and 2) to assess environmental operating limitations. As such, the prototype sensor was designed to measure directional spectra in a manner similar to the USACE Directional Wave Gage (DWG) which uses three bottom-mounted pressure sensors, spaced 1.8 m apart, to measure sea surface elevation (Earle et al., 1995 and Howell, 1998). This study was the first to apply lidar for measurement of directional energy spectra at a fixed location.

The LWG sensor platform was designed to allow testing from various heights above the water surface as well as from various beam angles, relative to vertical. The latter design requirement allowed testing of maximum angles at which water surface elevations could be measured. This was an important parameter to quantify as capabilities for measuring the sea surface with larger laser beam angles

could lead to future scanning sensor designs. Such a scanning laser sensor would have the capability to fully map the sea surface over an entire region, rather than at only one specific location.

The prototype LWG consists of two main segments: a sensor platform and a data acquisition suite (Figure 3.4). The instrument allows for easy manual adjustment of laser footprint (laser spot) positions and spacing on the water surface.

3.2.1 Sensor Platform

The sensor platform contains four model SLX-3A infrared rangefinders that are programmed for the purpose of recording and transmitting remote range measurements to a personal computer (PC) at a rate of 2 kHz (Optech Inc., 1999). Each rangefinder field of view (FOV) is folded 90 deg by a steering mirror, and each steering mirror is adjustable to allow translation of the laser FOV on the target surface over an approximate ±12 deg range relative to the sensor platform. The rangefinders transmit and receive through glass windows so that the enclosure can be sealed to moderate weather. Access to the mirror adjustments is provided through a removable weather-sealed cover.

The sensor platform has an electronic compass with direction (heading) and inclinometer (attitude) outputs. This provides accurate positioning information on the laser footprint pattern. The entire sensor platform may be rotated about its longitudinal axis more than 45 deg forward and back. The compass module provides the final attitude of the platform once it is in place.

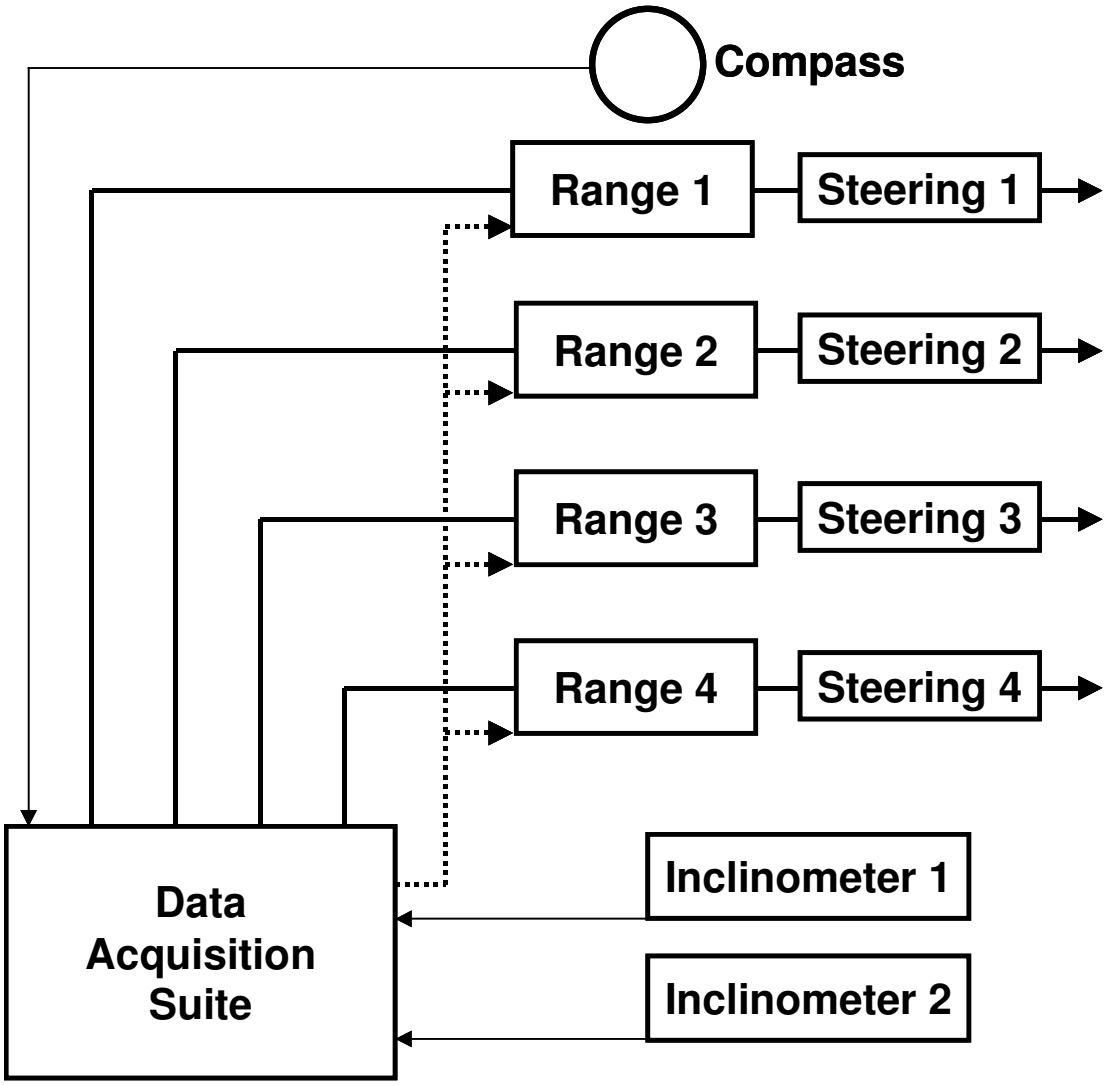

Figure 3.4 Prototype LWG diagram.

3.2.2 Data Acquisition Suite

The data acquisition suite consists of a PC and a 24-V DC power supply to provide the sensor platform with power. Installed in the PC is a multi-port adapter card that adds four additional serial ports. The rangefinder microprocessors communicate with the PC through this card. A timer/counter card, installed in the PC, provides timing and simultaneous trigger signals for the four rangefinders.

The sensor software is configured for a sampling rate of 10 Hz. For each of the four rangefinders, one reported measurement is the average of 80 laser pulses fired in a 40-ms burst.

3.3 Field Experiment

The LWG field experiment was conducted at the FRF, Figure 3.1, in December 1999 (Leffler et al., 1996). The FRF was selected because of its existing infrastructure and experienced personnel for supporting coastal field experiments. Specifically, the field experiment utilized the FRF's Sensor Insertion System (SIS) and existing 8-m array: a pressure gage network for wave measurement (Miller et al., 1999). Figure 3.5 illustrates the experiment layout at the FRF.

3.3.1 Experimental Setup

The lidar sensor platform is designed to mount directly onto the SIS upper boom as shown in Figure 3.6 (Miller et al., 1999). A PUV was positioned on the SIS lower boom to provide co-located ground truth measurements. The ability of the SIS to traverse the length of the FRF pier allowed for testing of the LWG from a range of elevations above the water surface. Additionally, the LWG and its mounting system allowed for testing of a range of nadir angles. During the experiment, sensor elevation

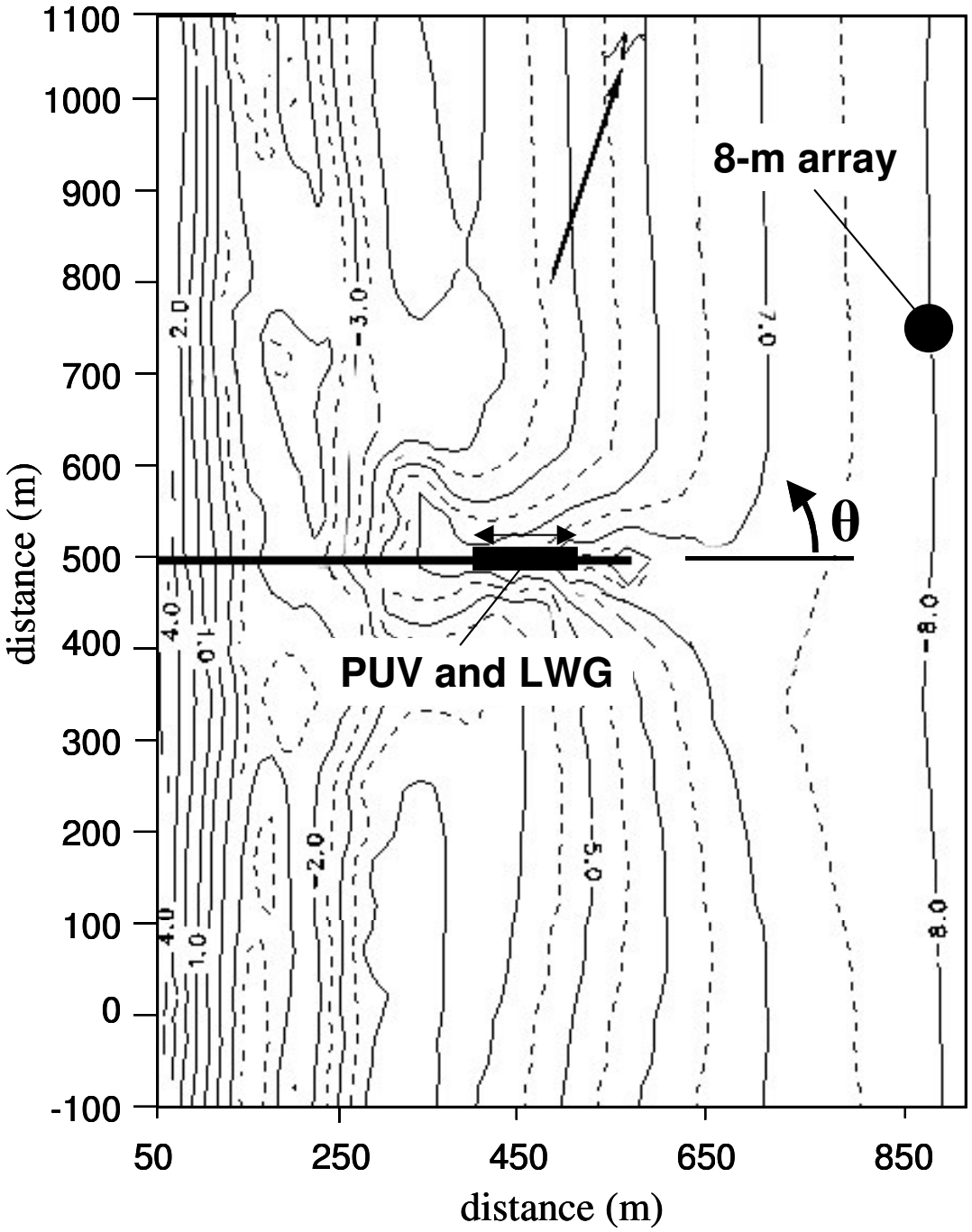

Figure 3.5 **LWG, PUV, and 8-m linear array locations at the FRF and December 1999 bathymetry. Depth contours are in meters and position is relative to local FRF horizontal coordinate system.**

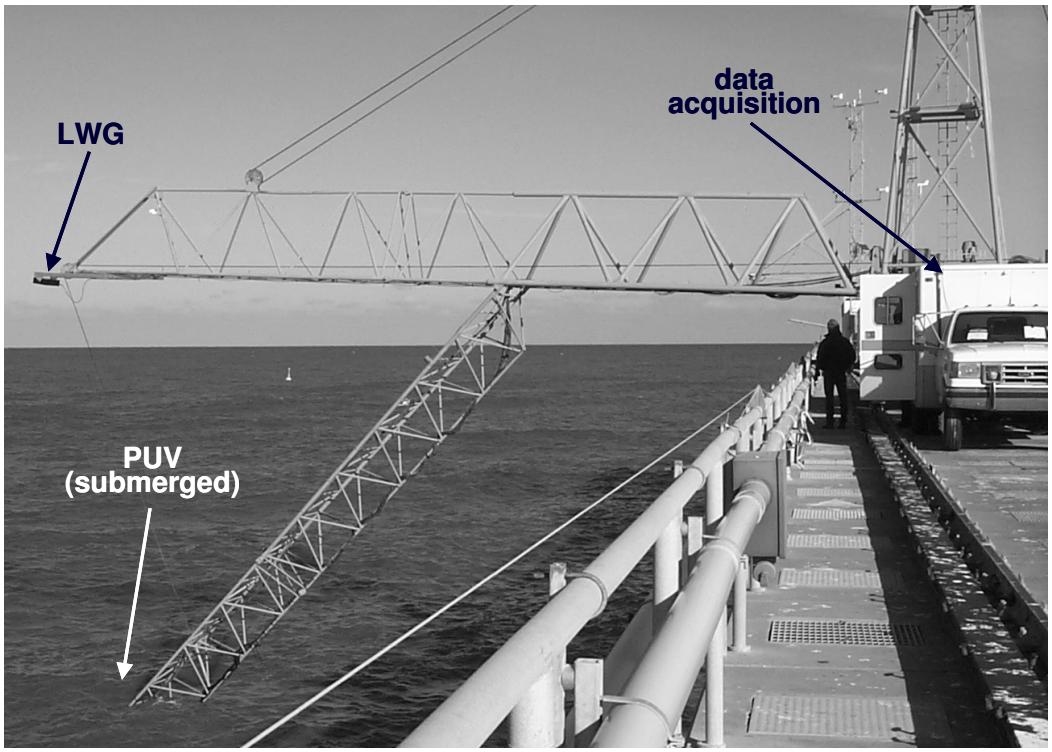

Figure 3.6 LWG and PUV mounted on SIS.

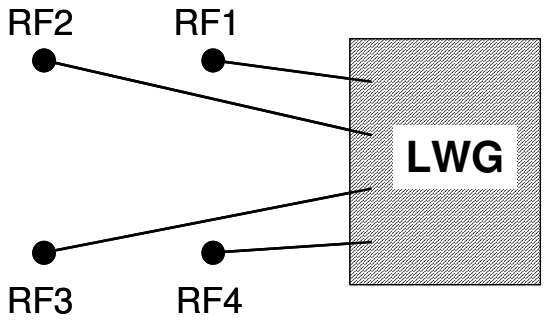

Figure 3.7 Footprint locations on water surface for rangefinders RF1, RF2, RF3, and RF4.

above the water surface varied from 6 m to 16 m while nadir angles varied from 0 deg to 30 deg. The ability to prescribe LWG elevation and rangefinder nadir angles allowed the four individual laser footprints to be positioned to form a rectangle with spacing varying from 0.6 m to 2.0 m on the water surface (Figure 3.7). Over this range of sensor elevations, the rangefinder footprints on the water surface were between 7 cm and 12 cm in diameter.

3.3.2 Data Collection

Data sets were collected for two purposes: to quantify LWG sensitivity to environmental and sensor parameters and to quantify LWG ability to accurately measure directional spectral wave characteristics (Irish, et al., submitted; Irish et al., 2000b; and Irish et al., 2001). In all cases, each LWG data set consisted of an 83-minute time series (50,000 time records at a sample frequency of 10 Hz) of three-dimensional position at four locations on the water surface. Figure 3.8 shows a sample time series of water surface elevation (η) for one rangefinder.

Data sets collected to test the LWG ability to accurately measure directional spectral wave characteristics were collected with co-located ground truth via the PUV. The PUV was configured to collect 17-minute data sets at a collection rate of 16 Hz. PUV data collection was not always possible for data sets collected to test the LWG sensitivity to environmental and sensor parameters. This was partially a result of problems with the SIS positioning unit and the PUV during the field experiment.

PUV data were processes by assuming linear wave theory to describe dynamic pressure and horizontal velocity to determine surface elevation and wave direction (Kirby, 1998 and Dean and Dalrymple, 1991). Directional spectra, including

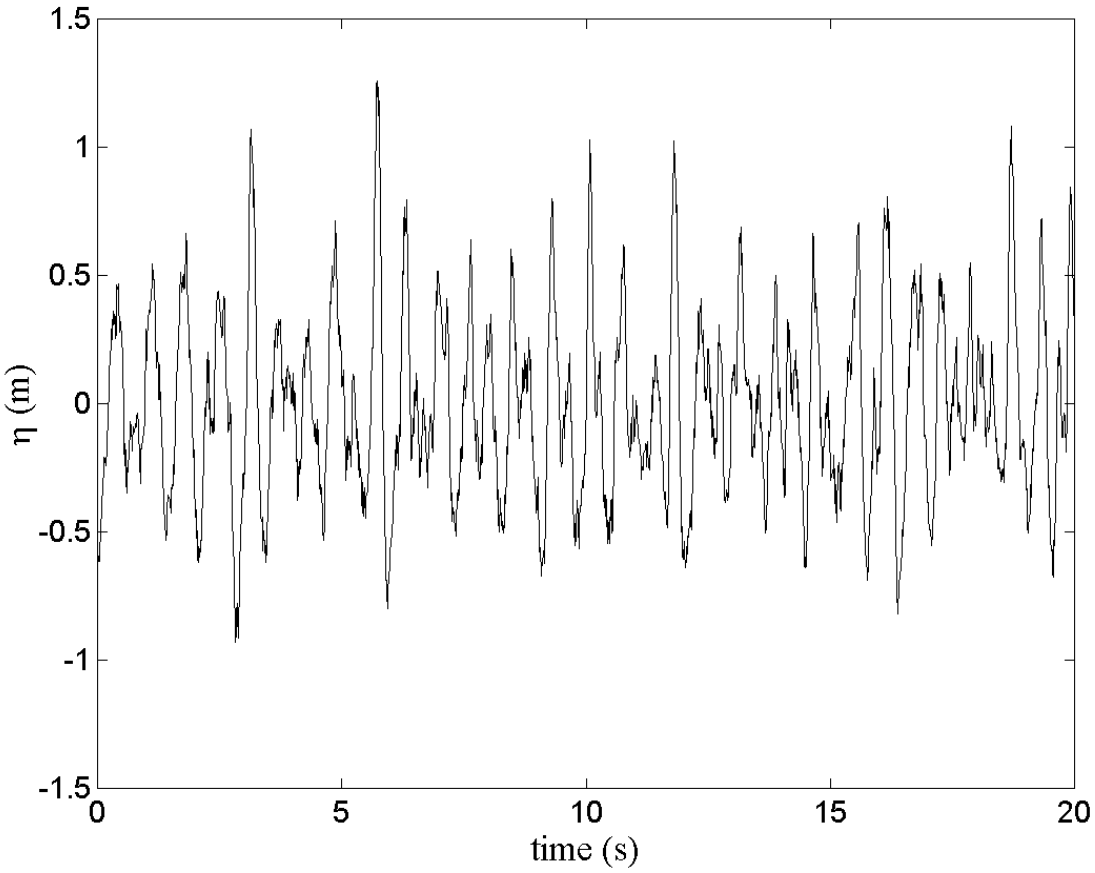

Figure 3.8 Sample LWG surface elevation time series (11 December 1999 at 0943 EST).

spectral wave height and peak frequency, were then computed following the method of Longuet-Higgins et al. (1963).

Additional ground truth wave measurements were available from the FRF's 8-m array (Figure 3.5). The 8-m array is a series of 15 pressure gages that measure surface displacement at several spatial locations (Long, 1996). The array is located north of the pier at the 8-m depth contour. Each 8-m array data set is 136 minutes long with a 2-Hz sample rate. These data are processed using the Iterative Maximum Likelihood Estimation algorithm (Pawka, 1982 and Pawka, 1983).

Data collection commenced on 7 December with the last collection day on 16 December. Co-located ground truth data were collected with the PUV from 8 through 15 December. Data records were collected over a variety of sea-surface conditions. Spectral wave height varied from 0.2 m to 1.5 m and varied in type from one-directional swell to choppy seas.

Data were also collected over a range of ambient light and weather conditions. Weather conditions ranged from sunny and clear to overcast skies. A few data records were collected during periods of light to moderate rain. Because the sensor is not fully weatherproofed, no data records were collected during periods of heavy rain. Wind conditions during data collection varied from nearly 1 m/s up to 12 m/s.

3.3.3 Sensor Difficulties

At the start of data collection on 11 December 1999, Rangefinder (RF) 2 began reporting erroneous ranges. Diagnostics on this rangefinder, after the completion of the field test, showed that a faulty transmitter was the cause. Therefore,

time series collected with RF2 on or after 11 December were not used in the data analyses.

On 14 December 1999, the LWG compass failed. As a result, the exact position of the sensor, relative to magnetic north, was not known for data collected from that point onward. However, the laser footprint position, relative to the sensor itself, was still known.

3.4 Sensitivity to Environmental Conditions

To analyze the LWG's sensitivity to various environmental and sensor parameters, each 83-min data set was divided into five subsets. Each subset contains 10,000 time records. Further, each rangefinder's time series was considered separately; however, data collected with RF2 were used only if collected before 11 December 1999 (see Chapter 3.3.3). A total of 388 rangefinder time series were analyzed, and all but one of the 83-minute data sets collected were used.

In the following sections, LWG performance is assessed in terms of the percentage of quality data collected by each rangefinder. For each laser return, the LWG data acquisition software determines whether there are any hardware-related errors with that return. Based on this check, the data acquisition software assigns the return with an error rating between 0 and 99, where a rating of 0 indicates a good return. If a laser return has a hardware error greater than 0, it is designated a poor return.

Following the hardware check, the laser range time series were analyzed to identify data outliers. Data outliers are false ranges recorded by the rangefinder. These false ranges usually result from measurement of a physical obstruction between the laser and the water surface. Some examples include sea spray, rain, dirt on the

LWG windows, and birds. The data outliers were identified by the significant difference between the mean ranging distance to the water surface and the ranging distance to the obstruction.

The percentage of quality data for each record was then determined from the total number of laser returns (10,000) less the poor hardware returns and the data outliers.

3.4.1 Nadir Angle and Wind Speed

Of all adjustable sensor settings, the LWG performance was most sensitive to nadir angle. A calm water surface is analogous to a mirror in that a very specific orientation of the surface (normal incidence) is required to return a beam of light on itself. Therefore, it was not surprising that ranging performance decreased as nadir angle increased (Figure 3.9; Wu, 1971 and Wu, 1972). However, it was surprising that nadir angles beyond just 10 deg resulted in a significant number of poor hardware returns.

The most significant limiting environmental parameter on LWG performance is wind speed. Wind speed directly correlates with the formation of capillary waves. These capillary waves provide surface roughness from which lidar signals are scattered back to the sensor. Without the presence of capillary waves, the water surface is glassy and generally reflects less laser energy back to the receiver. Therefore, the amount of lidar energy returned to the receiver is a direct function of the water surface roughness, or capillary waves. Consequently, the percentage of strong lidar returns increases as wind speed increases (Figure 3.9). In general, the LWG performed well when wind speeds, measured at the seaward end of the FRF pier, were above 5 m/s.

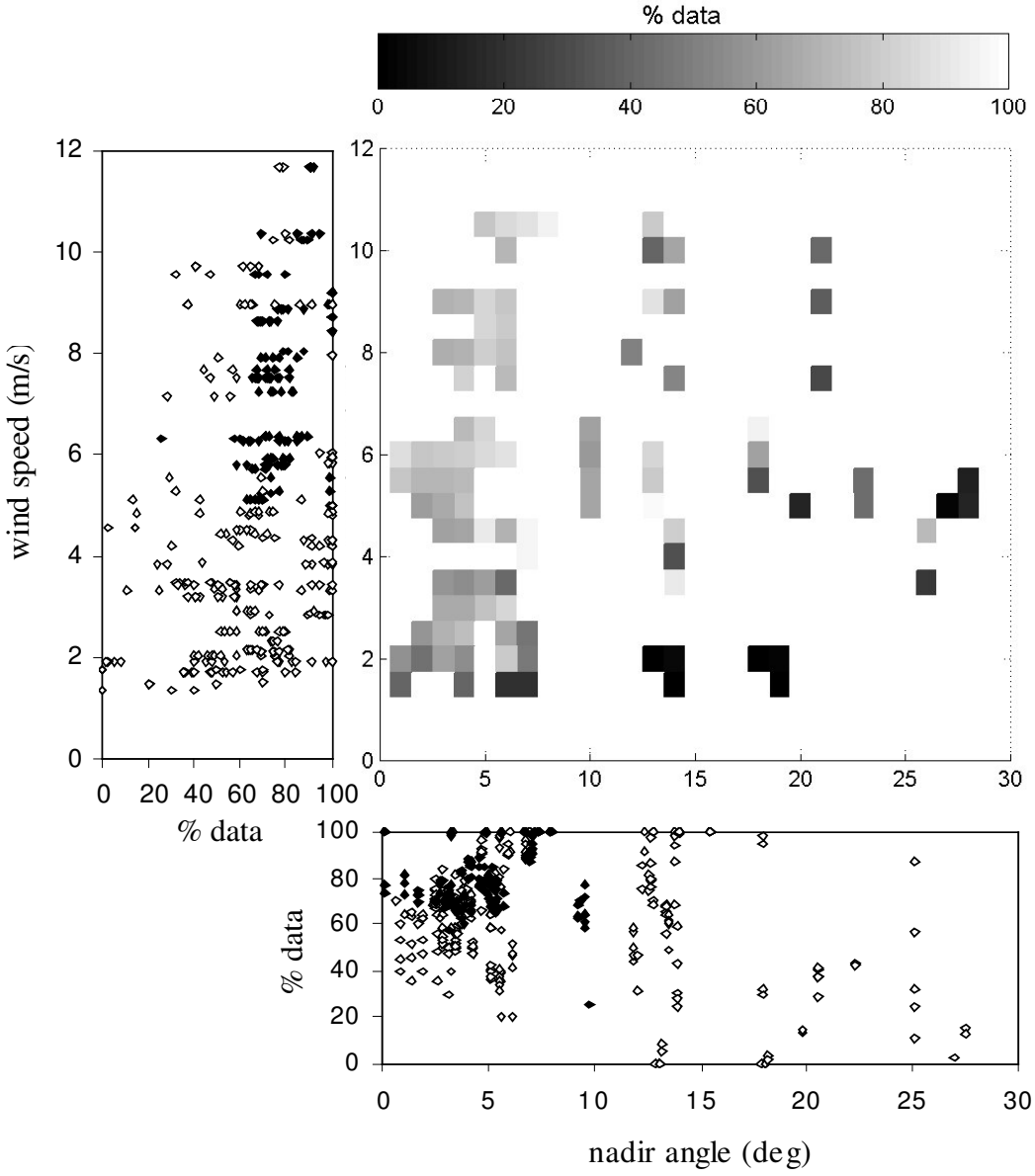

Figure 3.9 **Percentage of quality data collected relative to wind speed and nadir angle for all data collected. In the center plot, grid boxes are color-coded from black to light grey corresponding to 0% quality data to 100% quality data, respectively. A blank, or white, grid box indicates no data were collected for that wind speed and nadir angle pair. In the plots on the left and on the bottom, filled diamonds represent the subset of data with nadir angle of 10 deg or less and wind speed of 5 m/s or more.**

The impacts of wind speed and nadir angle on LWG performance are coupled (Figure 3.9). During the field experiment, the LWG performed well, containing 80% or more quality data, with larger nadir angles when wind speeds were higher.

Because wind speed and nadir angle so strongly influence LWG performance, the data are displayed in two groups for the remainder of Chapter 3.4. In the figures, filled diamonds represent data collected when wind speed is 5 m/s or greater and nadir angle is 10 deg or smaller. Hollow diamonds represent data collected when wind speeds were less than 5 m/s or nadir angles were greater than 10 deg.

3.4.2 Wave Climate

Because the LWG measures water surface elevation by ranging obliquely to the surface (when nadir angle is greater than 0 deg), the measured horizontal position varies with time. Figure 3.10 shows the variation in horizontal position of the footprint center for each rangefinder during two data collections. As expected, this variation is larger for larger wave heights: the variation is 8 cm when spectral wave height is 0.6 m while the variation is 15 cm when the spectral wave height is 1.3 m. Even during the most energetic wave conditions encountered during this field investigation, the spatial variation in footprint position was the same order of magnitude as the footprint size itself, on the order of 10 cm.

3.4.3 Sensor Elevation

Over the range of elevations tested, 6 m to 16 m, there was no correlation between sensor performance and sensor elevation (Figure 3.11). This indicates that

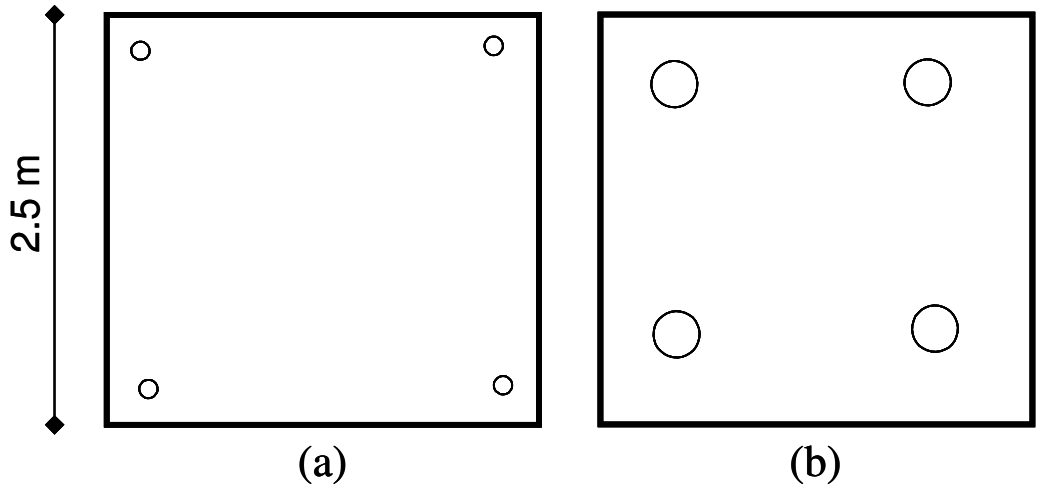

Figure 3.10 Horizontal variation in footprint position: (a) 8-cm variation with spectral wave height of 0.6 m and (b) 15-cm variation with spectral wave height of 1.3 m.

a LWG using model SLX-3A rangefinders may be efficiently deployed at any elevation between 6 m and 16 m.

3.4.4 Rain

There is no obvious correlation between the presence of rain and LWG performance for the range of rainfall conditions during which data were collected (Figure 3.12). However, rainy conditions did occasionally result in false elevation measurement by the rangefinders. The number of false elevations was minimal. In most cases, these false elevations could be detected and removed prior to spectral wave analysis.

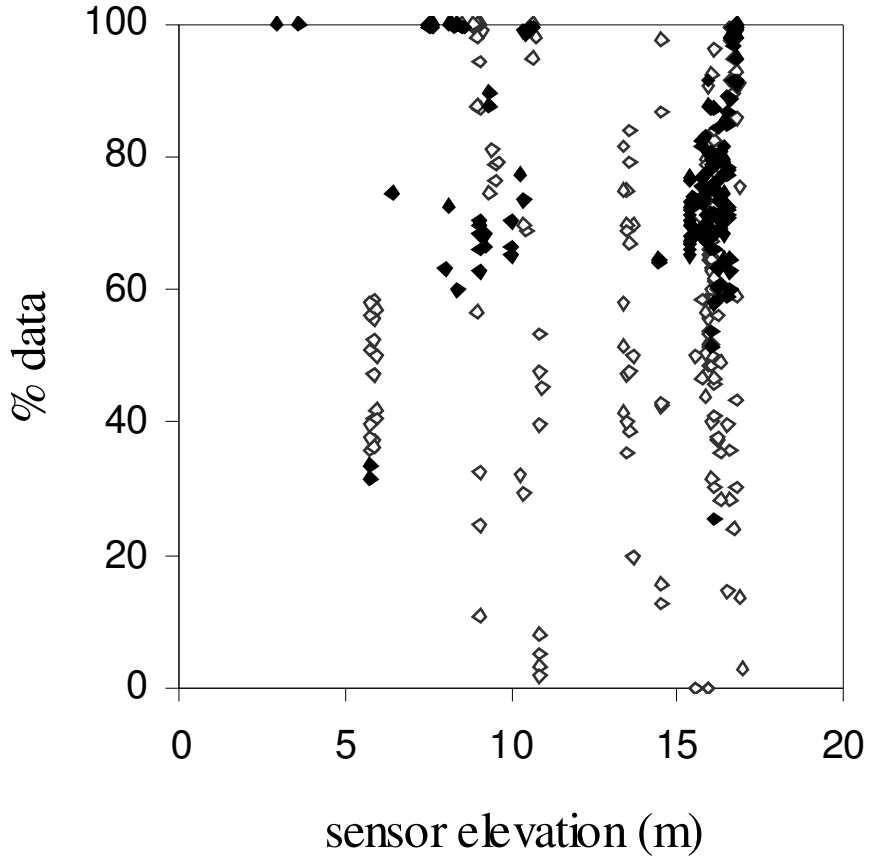

Figure 3.11 Percentage of quality data collected relative to sensor elevation above water surface. Filled diamonds represent the subset of data with nadir angle of 10 deg or less and wind speed of 5 m/s or more.

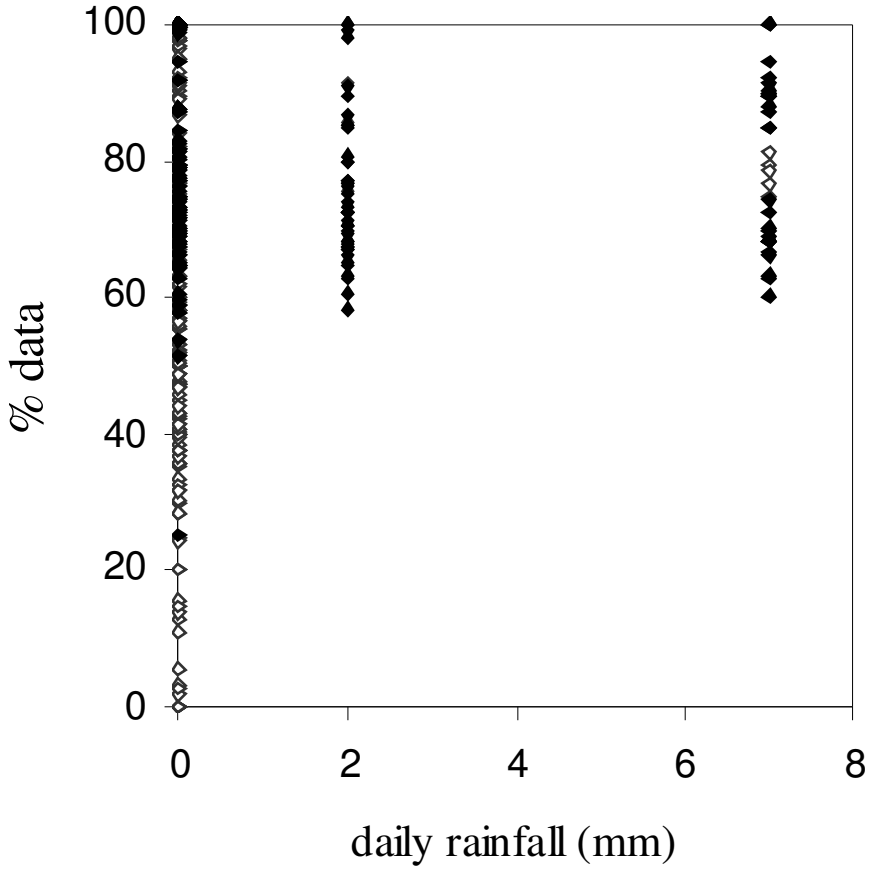

Figure 3.12 Percentage of quality data collected during rain. Filled diamonds represent the subset of data with nadir angle of 10 deg or less and wind speed of 5 m/s or more.

The lack of a fully weatherproofed casing and exposure to heavy rain between data collections resulted in some water damage to the LWG. However, once the LWG dried, there was no noticeable depreciation in LWG performance.

3.4.5 Ambient Light Conditions

The field experiment showed that ambient light conditions did not impact LWG performance. Specifically, there was no correlation between the percentage of strong lidar returns during a given data collection and ambient light conditions (Figure 3.13).

3.5 Accuracy for Measuring Spectral Wave Parameters

3.5.1 Spectral Analysis Methodology

Spectral wave characteristics are derived from Fourier analysis of the surface elevation records. The following sections provide an overview of Fourier analysis methods and application for computing ocean wave characteristics from measured time series.

3.5.1.1 Fourier Series, Fourier Transform, and Correlation Functions

Greenberg (1988) and Kirby (1998) provide a complete overview of the theory governing Fourier analyses, and this section details the Fourier relationships important for wave spectral analysis. Any function may be exactly described by the sum of an even and odd function. For a periodic, piecewise-continuous function, like those of sea surface elevation, it is logical to describe the even component in terms of

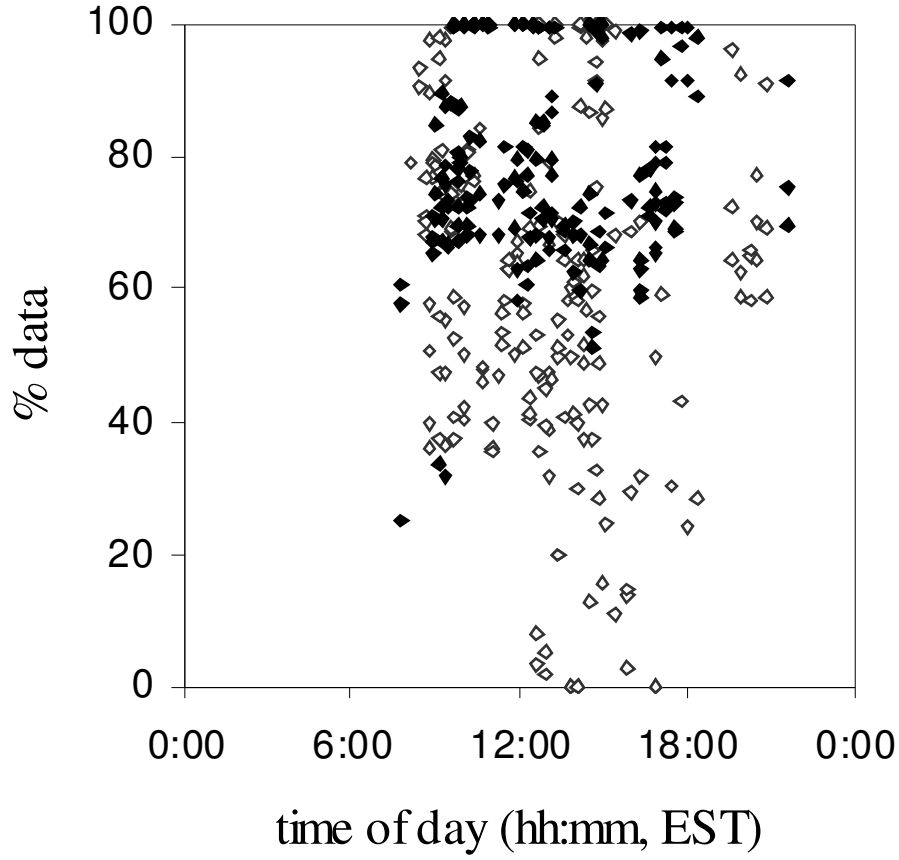

Figure 3.13 Percentage of quality data collected relative to ambient light conditions. Filled diamonds represent the subset of data with nadir angle of 10 deg or less and wind speed of 5 m/s or more.

cosine functions and the odd component in terms of sine functions. This periodic function may be described as a Fourier series. For this analysis, the Fourier series is:

$$\eta(t) = a_o + \sum_{n=1}^{\infty} \left[a_n \cos(n\omega t) + b_n \sin(n\omega t) \right] \tag{3.3}$$

where:

$\eta(t)$	is the water surface elevation at time t
ω	is the fundamental angular frequency
a_0, a_n, and b_n	are the Fourier coefficients

The Fourier coefficients are themselves defined in terms of $\eta(t)$:

$$a_o = \frac{1}{T} \int_0^T \eta(t) dt \tag{3.4}$$

$$a_n = \frac{2}{T} \int_0^T \eta(t) \cos(n\omega t) dt \tag{3.5}$$

$$b_n = \frac{2}{T} \int_0^T \eta(t) \sin(n\omega t) dt \tag{3.6}$$

where T is the fundamental period and equal to $2\pi/\omega$. For wave spectral analysis, it is convenient to consider Equation 3.3 when rewritten in complex exponential form:

$$\eta(t) = \sum_{n=-\infty}^{\infty} F_n \, e^{in\omega t} \tag{3.7}$$

Then the Fourier coefficients are found by using the Fourier transform of η, $F_n(\eta)$:

$$F_n(\eta) = \frac{1}{T}\int_0^T \eta(t) e^{-in\omega t} dt \tag{3.8}$$

such that:

$$F_n(\eta) = \frac{a_n - ib_n}{2} \quad n \geq 0 \tag{3.9a}$$

$$F_n(\eta) = \frac{a_n + ib_n}{2} \quad n < 0 \tag{3.9b}$$

Here, the energy spectrum is represented by the square of the absolute value of F_n. Since Equation 3.9 demonstrates that the complex conjugate of F_n, or F_n^*, equals F_{-n}, the energy spectrum is symmetrical about n = 0. This energy spectrum is termed the two-sided, or unfolded, energy spectrum.

The cross- and auto-correlation functions prove valuable for computing directional wave spectra. The cross-correlation function, C_{ij}, is defined as:

$$C_{ij} = \frac{1}{T}\int_0^T \eta_i(t)\, \eta_j(t+\tau) dt \tag{3.10}$$

where:

η_i, η_j are two surface elevation time series

τ is the time lag between η_i and η_j and equals zero for this study

The auto-correlation function is a special case of the cross-correlation where i = j. The cross-correlation function, Equation 3.10, may also be described in terms of the Fourier transforms of η_i and η_j:

$$C_{ij} = \sum_{n=-\infty}^{\infty} \Phi_{ij}(n) e^{in\omega t} \tag{3.11}$$

where the complex cross-spectral density function, $\Phi_{ij}(n)$, is given by:

$$\Phi_{ij}(n) = F_i^*(n)\, F_j(n) \tag{3.12}$$

3.5.1.2 Wave Spectra and Wave Characteristics

The following describes how the Fourier transform and the complex cross-spectral density function are applied to determine wave field characteristics from the lidar time series collected during this investigation (Kirby, 1998; Earle et al., 1995; and Longuet-Higgins et al., 1963).

3.5.1.2.1 Non-Directional Wave Spectra

The non-directional power spectral density function, S, is determined by folding the energy spectrum discussed earlier about n = 0. The power spectral density function, S, is then defined as:

$$S(f_n) = 2\, T \left| F_n \right|^2 \quad n \geq 1 \tag{3.13}$$

where the frequency, f_n, is defined as:

$$f_n = \frac{n}{T} \tag{3.14}$$

Observing that, for the case where i = j, $\Phi_{ij}(n)$, as give by Equation 3.12, represents the square of the absolute value of F_n, the non-directional power spectral energy density may also be defined as:

$$S(f_n) = 2\ T\ \Phi_{ii}(n) \quad n \geq 1 \tag{3.15}$$

3.5.1.2.2 Directional Wave Spectra

The complex cross-spectral density function may also be used to determine directional wave spectra. For this study, the lidar time series were analyzed using the slope array method (Howell, 1998; Kirby, 1998; Earle et al., 1995; and Higgins et al., 1981). The following outlines the slope-array method for four distinct recording locations. The diagonal sea surface slopes (s_{13} and s_{24}) are defined as (Figure 3.7):

$$s_{31} = \frac{\eta_3 - \eta_1}{\sqrt{(x_3 - x_1)^2 + (y_3 - y_1)^2}} \tag{3.16a}$$

$$s_{42} = \frac{\eta_4 - \eta_2}{\sqrt{(x_4 - x_2)^2 + (y_4 - y_2)^2}} \tag{3.16b}$$

where (x_i, y_i) is the horizontal position of the recorded surface elevation time series, η_i. The mean surface elevation, $\bar{\eta}$, is defined as:

$$\bar{\eta} = \sum_{m=1}^{M} \frac{\eta_m}{M} \tag{3.17}$$

where M is 4 for the case of four distinct recording locations. Finally, the mean wave direction, θ, for a particular wave frequency, f_n, is computed from:

$$\theta(f_n) = \arctan\left(\frac{Q_{\bar{\eta}s_{31}}(f_n)}{Q_{\bar{\eta}s_{42}}(f_n)}\right) \tag{3.18}$$

where Q is the quadrature spectral density function of the mean surface elevation and the sea surface slope, defined as the imaginary part of the complex cross-spectral density function, Φ, given in Equation 3.12:

$$\Phi_{ij}(f) = \hat{C}_{ij}(f) - i\hat{Q}_{ij}(f) \tag{3.19}$$

where C_{ij} is the coincident spectral density function.

3.5.1.2.3 Wave Spectra Characteristics

Several wave spectral properties may be extracted from directional wave spectra. Among these are the spectral wave height, peak wave frequency, and peak wave direction. The following definitions will be used in this study.

Spectral wave height, H_{mo}, is computed from the first moment of the power spectral density function given in Equation 3.15:

$$H_{mo} = 4\sqrt{\int_0^{\infty} S(f)df} \tag{3.20}$$

The peak frequency, f_p, is the frequency corresponding to the peak of the folded non-directional energy spectrum. Finally, peak wave direction, θ_p, is mean wave direction at f_p calculated using Equation 3.18.

3.5.1.3 Application to Discrete Time Series

Kirby (1998) describes how Fourier analysis may be applied to a discrete time series. The required assumption to apply Fourier analysis to a discrete time series is that the time series is periodic, with fundamental period T, over the collection interval such that:

$$T = N\ \Delta t \tag{3.21}$$

where:

N is the number of records in the time series

Δt is the time step

The fundamental frequency, f, is defined as the inverse of the fundamental period, and as such, the spectral resolution is the inverse of the record length. Because the LWG collects discrete time series of finite duration, the Fourier series must be truncated. Consequently, the number of Fourier coefficients, F_n, is limited by n = N/2, where N equals the number of measurements in the time series. In addition, the maximum resolved frequency, the Nyquist frequency ($f_{Nyquist}$), is dependent on the time interval, Δt, and is defined as:

$$f_{Nyquist} = \frac{1}{2\Delta t} \tag{3.22}$$

For analysis of discrete time series, Equation 3.7 and Equation 3.8 become the discrete Fourier transform pair:

$$\eta_j = \sum_{n=0}^{N-1} F_n \, e^{2\pi i\left(\frac{nj}{N}\right)} \tag{3.23}$$

$$F_n(\eta) = \frac{1}{N}\sum_{j=1}^{N} \eta_j \, e^{-2\pi i\left(\frac{nj}{N}\right)} \tag{3.24}$$

where j is the record number such that η_j is the time series value for record number j at time $t_j = j\Delta t$. For this study, computer programs were written with Matlab software to perform these calculations.

3.5.2 Data Processing

Prior to spectral wave analysis, each data set was analyzed to determine the percentage of quality data using the procedure discussed in Chapter 3.4. If any one rangefinder time series had more than 20% data loss, the entire data set was excluded from the spectral analysis. In addition, a data set was eliminated when any one rangefinder time series had a continuous data gap longer than 2 s. Artificial data were linearly interpolated to fill in any data gaps smaller than 2 s. The 2-s gap length was somewhat arbitrarily selected. Decreasing the acceptable gap length reduced the number of data sets that could be analyzed, and a 2 s gap is anticipated to be small enough such that analyses of wave fields characterized by peak periods on the order of 10 s or greater is not significantly impacted.

Ten 83-minute data sets, collected between 8 and 14 December 1999, were selected for spectral wave analysis. From these ten 83-minute data sets,

55-minute data sets were analyzed and compared with wave measurements made by the FRF's 8-m array. In addition, the 83-minute data sets were divided into 5 subsets: 50 14-minute data sets were compared with wave measurements made by the co-located PUV. The time series durations of 55 minutes and 14 minutes were selected for analyses to correspond with the time series durations of the 8-m array and the PUV, respectively. The mean and linear trends were removed from each time series prior to analysis. This is accomplished by using the detrend command in Matlab which computes the least-squares straight line fit for the time series then subtracts it from the time series.

All LWG data were analyzed using the Fourier methods and slope array methods described in Chapter 3.5.1 above, and the horizontal position of each rangefinder's footprint on the surface was assumed stationary.

Each rangefinder time series was divided into 15 half-overlapping segments, and analysis was conducted for each. Once analysis was completed for each of the 15 segments, the results were averaged to produce a final result for the data set. The spectral analysis parameters used for processing the 55-minute and 14-minute LWG data sets are summarized in Table 3.1. The LWG resolution frequency bandwidths are 0.0391 Hz and 0.0123 Hz to align with the PUV and the 8-m array resolution bandwidths of 0.0313 Hz and 0.0098 Hz, respectively.

LWG data sets collected prior to 11 December were processed using time series from all four rangefinders. The slope array method was configured to use two independent gage pairs: RF1 paired with RF3 and RF2 paired with RF4 (Figure 3.7). As mentioned earlier, RF2 time series were not used for data sets collected on

Table 3.1 Spectral analysis parameters.

		14-Minute Record	55-Minute Record
Record length:	time (min)	13.7	54.6
	number of measurements	8192	32768
Number of segments		15	15
Segment length:	time (min)	1.7	6.8
	number of measurements	1024	4096
Raw bandwidth (Hz)		0.00977	0.00244
Resolution bandwidth:	number of bands	4	5
	bandwidth (Hz)	0.0391	0.0122

11 December or later. For these data sets, the two gage pairs are RF1 paired with RF4 and RF3 paired with RF4, where RF4 is used twice.

3.5.3 Comparison with PUV

Wave energy and direction spectra calculated with LWG data sets are compared to those calculated with PUV data sets in Figure 3.14 and Figure 3.15. In the figures, the displayed direction is the direction from which waves are coming, measured counter-clockwise from the FRF pier axis (Figure 3.5). For the representative cases shown, the LWG spectra match well with the PUV spectra, particularly near the spectral peaks. Away from the spectral peak, however, there is some discrepancy in wave direction for the higher energy case (Figure 3.15). While there are some discrepancies (as illustrated in Figure 3.15), the LWG spectral shape and magnitude match well with PUV results for all 50 data sets compared.

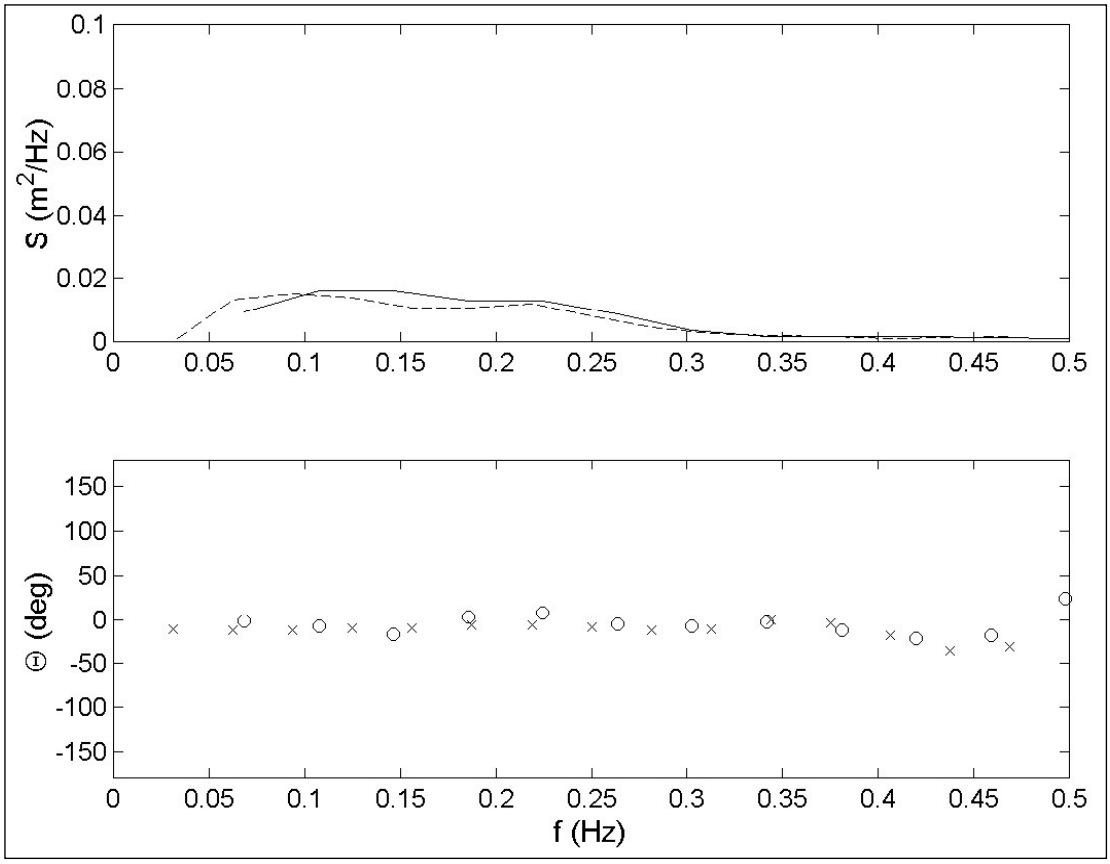

Figure 3.14 Directional spectrum for LWG (solid line and circles) and PUV (dashed line and x's) on 9 December 1999 at 1226 EST.

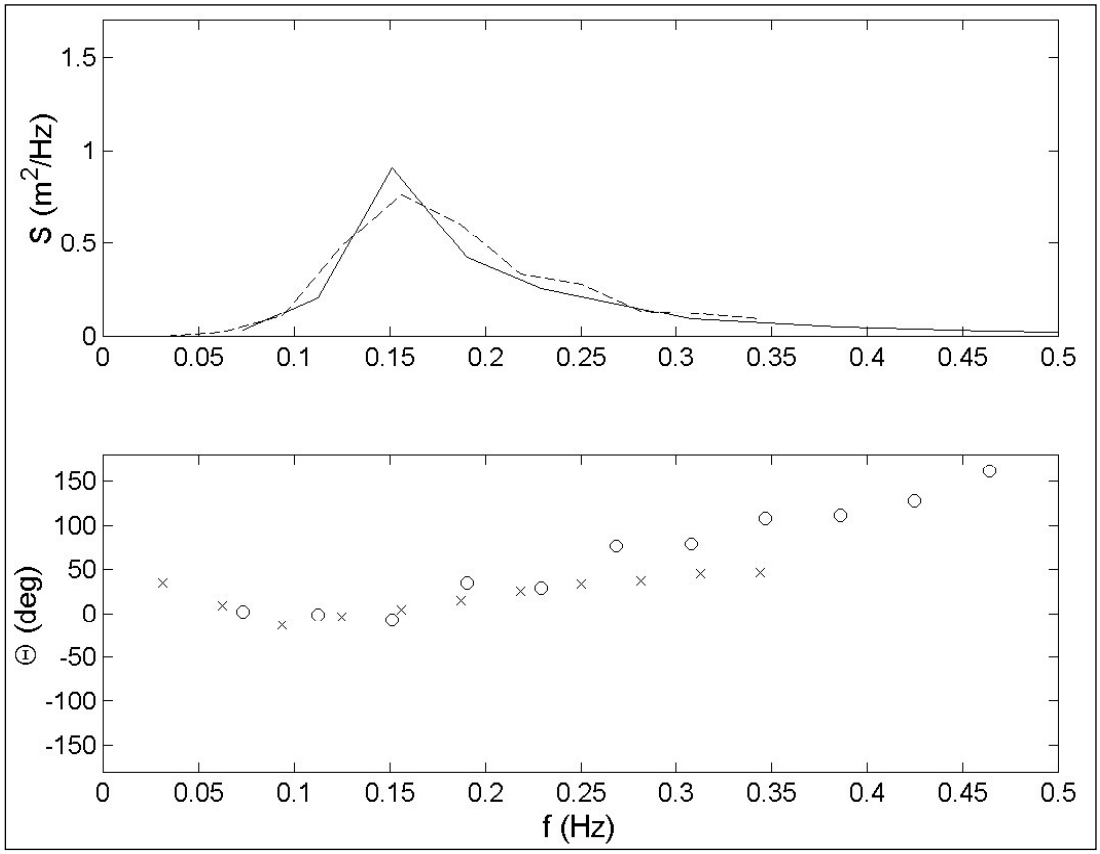

Figure 3.15 Directional spectrum for LWG (solid line and circles) and PUV (dashed line and x's) on 11 December 1999 at 1151 EST.

The spectral wave characteristics f_p, H_{mo}, and θ_p also compare well (Table 3.2). The f_p computed for the LWG versus that for the PUV for all 50 data sets is shown in Figure 3.16. With the exception of two data sets, all of the LWG results fall within one resolution bandwidth of the PUV results. These two data sets overlap on this figure and subsequent figures because the data sets were collected sequentially and effectively represent the same wave condition. RMS error and the square of the Pearson product moment correlation coefficient (R^2) for f_p are 0.0129 Hz and 0.95, respectively.

The H_{mo} computed from the LWG data and the PUV data are compared in Figure 3.17. Again, the LWG data match well with the PUV data. As wave height increases, there is more deviation between the LWG and PUV H_{mo} measurement. However, all but two of the LWG wave heights fall within 10% of the PUV wave heights (dashed lines on the figure). The RMS error and R^2 for H_{mo} are 0.05 m and 0.99, respectively.

Table 3.2 Statistics from LWG and PUV comparisons.

	Mean Difference	Standard Deviation of Difference	RMS Error	R^2
H_{mo} (m)	0.01	0.05	0.05	0.99
f_p (Hz)	0.0057	0.0117	0.0129	0.95
θ_p (deg)	0.4	7.7	7.6	0.89

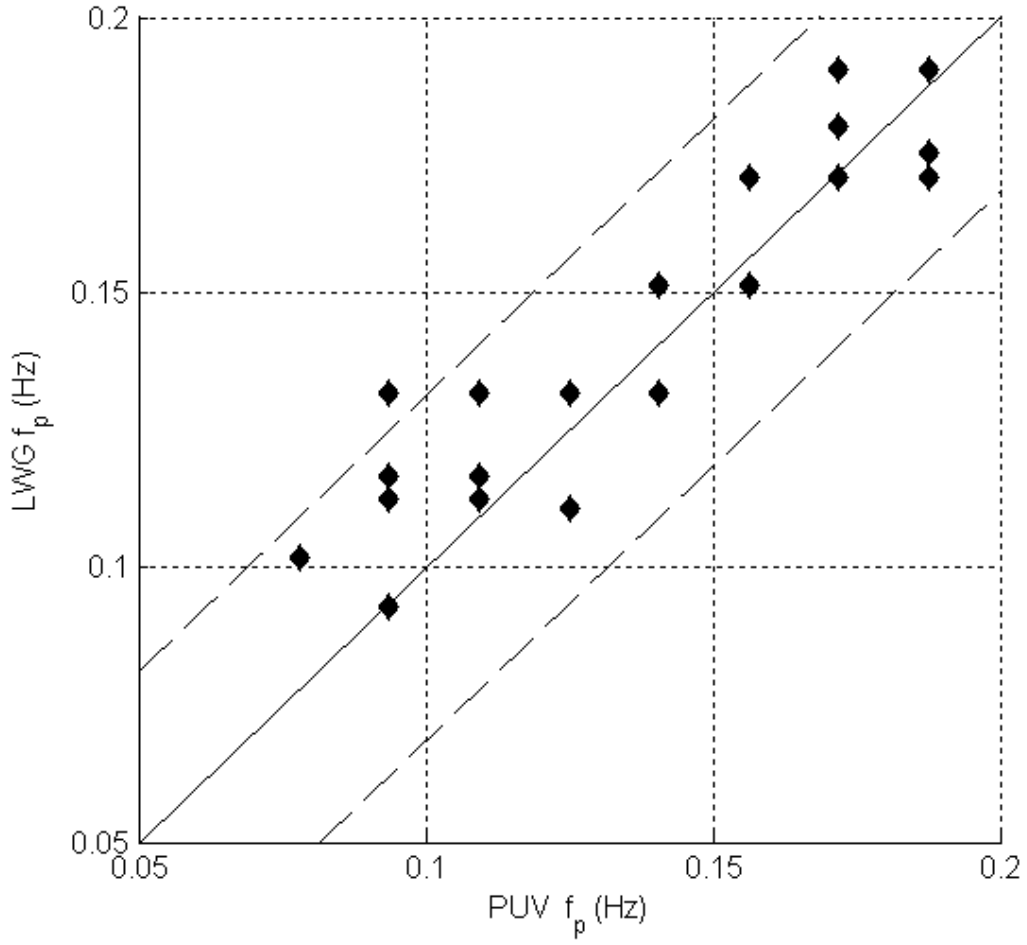

Figure 3.16 Comparison between the LWG and PUV peak frequency, f_p. Solid line on figure indicates an exact match while dashed lines on figure indicate one resolution frequency bandwidth.

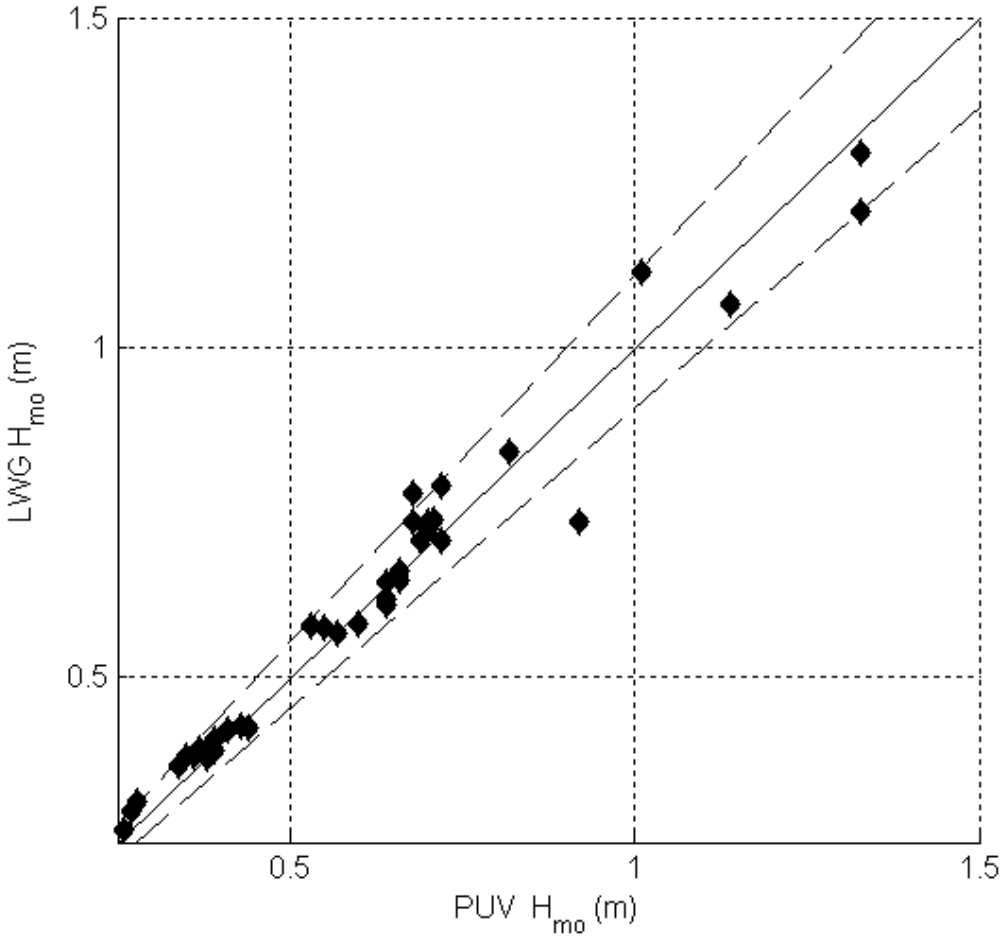

Figure 3.17 Comparison between the LWG and PUV spectral wave height, H_{mo}. Solid line on figure indicates an exact match while dashed lines on figure indicate 10% about the measured spectral wave height.

Mean wave direction at the spectral peak, θ_p, for the LWG and PUV data are plotted in Figure 3.18. The figure shows that LWG θ_p correlates fairly well with PUV θ_p, and all LWG-PUV comparisons fall within 18 deg of each other. RMS error and R^2 for θ_p are 7.6 deg and 0.89, respectively. While such errors in θ_p may be significant for assessing coastal processes such as longshore sediment transport, they are comparable to errors reported for in situ PUV sensors, as discussed below.

Grosskopf et al. (1983) reported on measurements of nearshore mean wave direction at the spectral peak for several co-located in situ wave gages, including two PUV sensors. Data collected with the two PUV sensors during this experiment were processed in the manner PUV sensor data were processed for this study. Specifically, wave direction was determined by assuming linear wave theory and following the methods of Longuet-Higgins et al. (1963). The authors reported R^2 between the two PUV sensors to be 0.90. Reported R^2 between mean direction at the spectral peak as measured with the two PUV sensors relative to direction measured with a co-located slope-array sensor were 0.94 and 0.90. The slope-array sensor was configured to record pressure at four locations in a square pattern similar to the LWG square pattern. The direction data presented by Grosskopf et al. (1983) showed comparisons similar to those observed in this study. Specifically, the authors showed that direction comparisons between the two PUV sensors and the slope-array sensor were almost all within 20 deg; only two measurements reported had differences greater than 20 deg.

The relationship between wave height and directional measurement accuracy is illustrated in Figure 3.19. As anticipated, the directional measurement

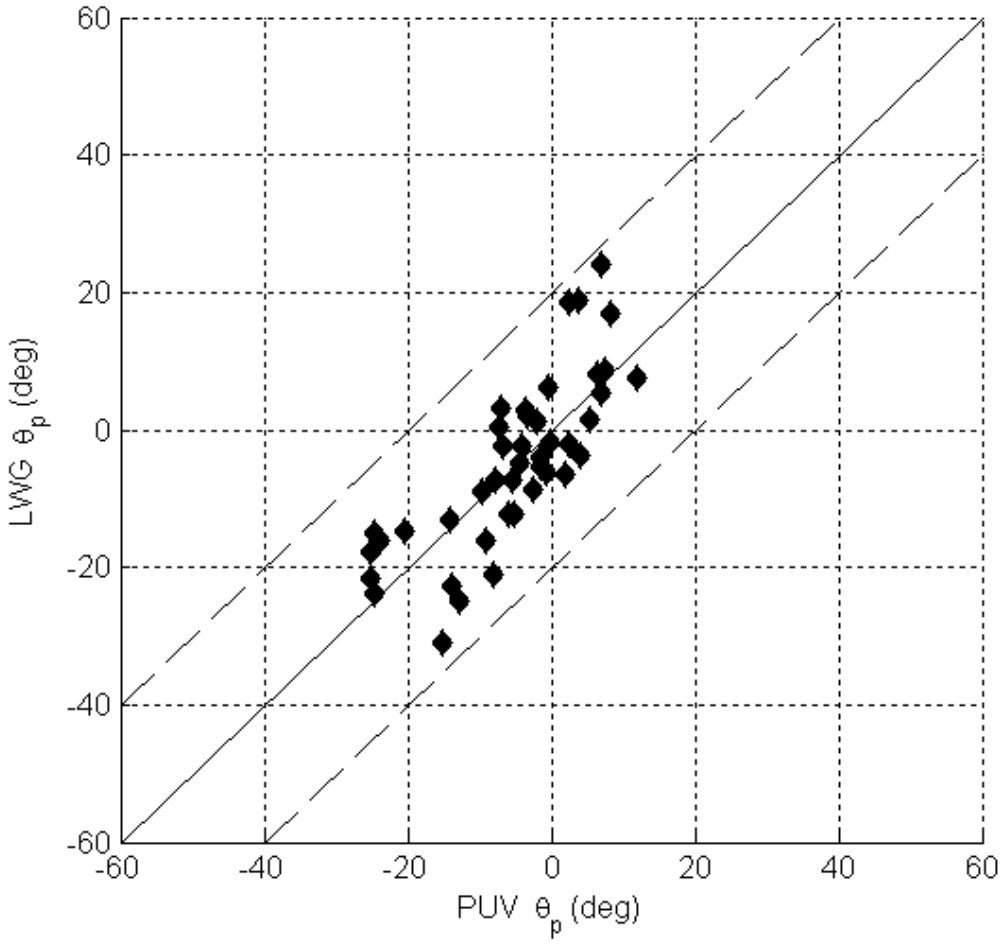

Figure 3.18 Comparison between the LWG and PUV peak direction, θ_p. Solid line on figure indicates an exact match while dashed lines on figure indicate 20 deg about the measured peak direction.

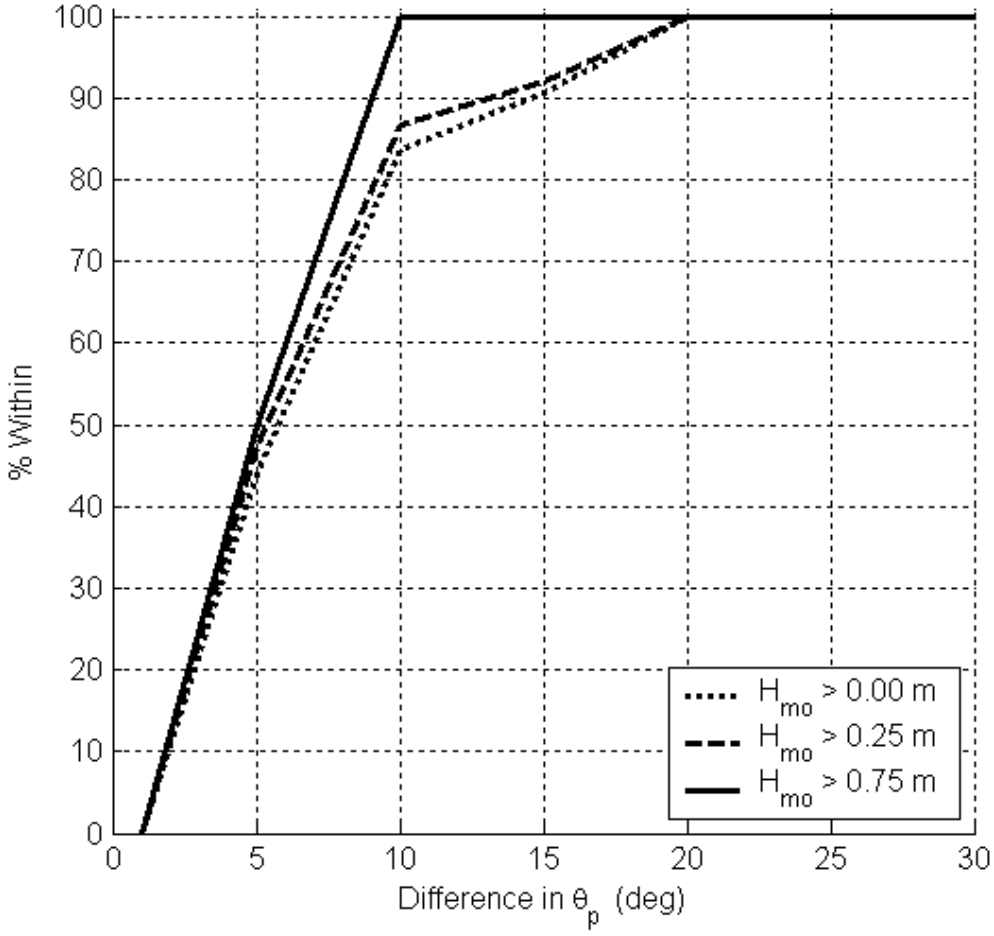

Figure 3.19 Deviation in mean wave direction at spectral peak, computed from the LWG and PUV data, as a function of H_{mo}. Percent within indicates percent of measured direction differences within the direction difference given by the x-axis.

capability of the LWG improves as wave height increases. This is a logical finding since surface slope (s_{31} and s_{42}) is better quantified when the surface elevation difference is amplified. The figure shows that 90% of the 50 LWG peak wave directions, for all wave heights, fall within 15 deg of PUV peak directions. When considering only the peak wave directions when H_{mo} is greater than 0.75 m, 90% of the LWG directions fall within 8 deg of the PUV directions.

3.5.4 Comparison with 8-m Array

Even though the 8-m array is north and offshore of the LWG, comparisons between these two data types are valuable. Firstly, the longer data sets collected by the 8-m array allow for comparison of LWG data collected over longer periods. Using longer data sets provides stability to the spectral analysis and allows for much finer frequency resolution (see Table 3.1). Using longer data records should then produce results that are more reliable.

Energy and direction spectra computed with the LWG are compared to those computed with the 8-m array in Figure 3.20 and Figure 3.21. Comparing the spectra, energy appears to shift somewhat for both cases shown. These energy shifts are most likely attributed to the physical processes governing wave propagation inshore, to wind field variation between the 8-m array location and the LWG location, to FRF pier effects, or to the slight variation or shift in time of data collection. All ten LWG data sets energy and direction spectra match with the 8-m array spectra in light of the uncertainties discussed above.

The LWG f_p, H_{mo}, and θ_p are compared against those measured by the 8-m array in Figure 3.22 through Figure 3.24. In two cases, the peak wave frequency for

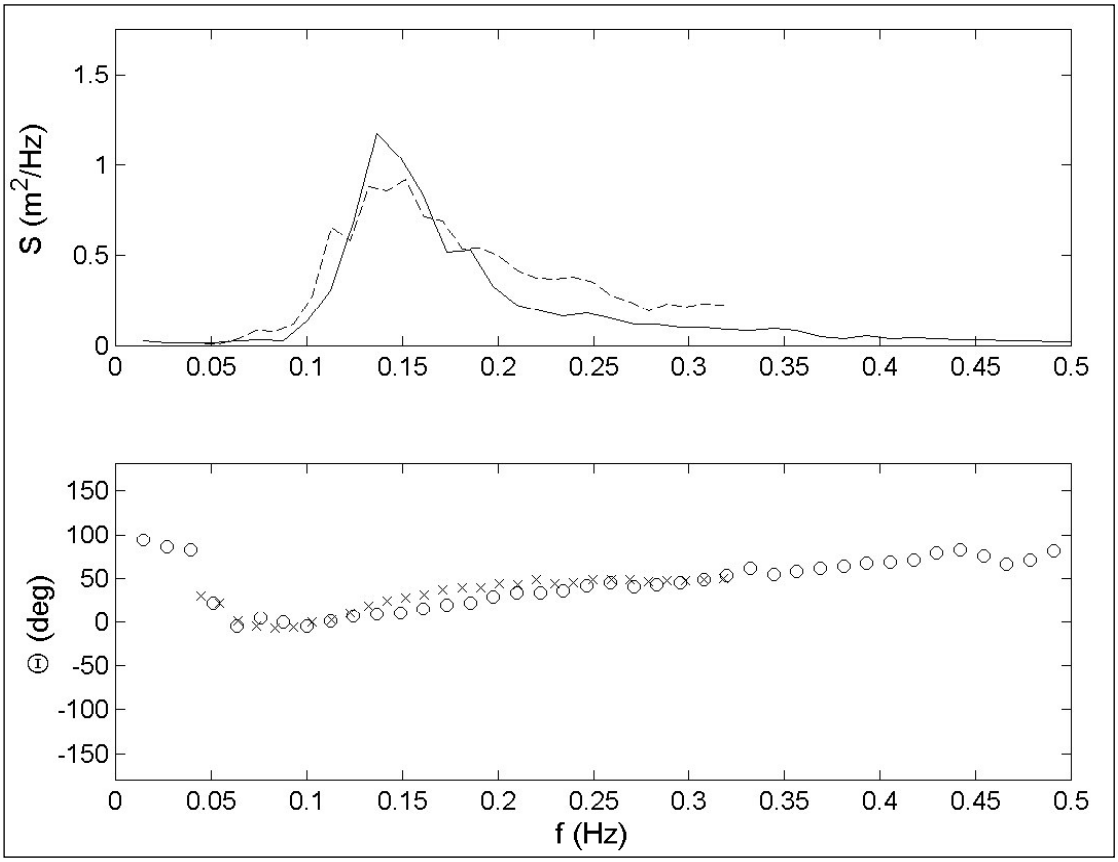

Figure 3.20 Directional spectrum for LWG (solid line and circles) and 8-m array (dashed line and x's) on 11 December 1999 at 1151 EST.

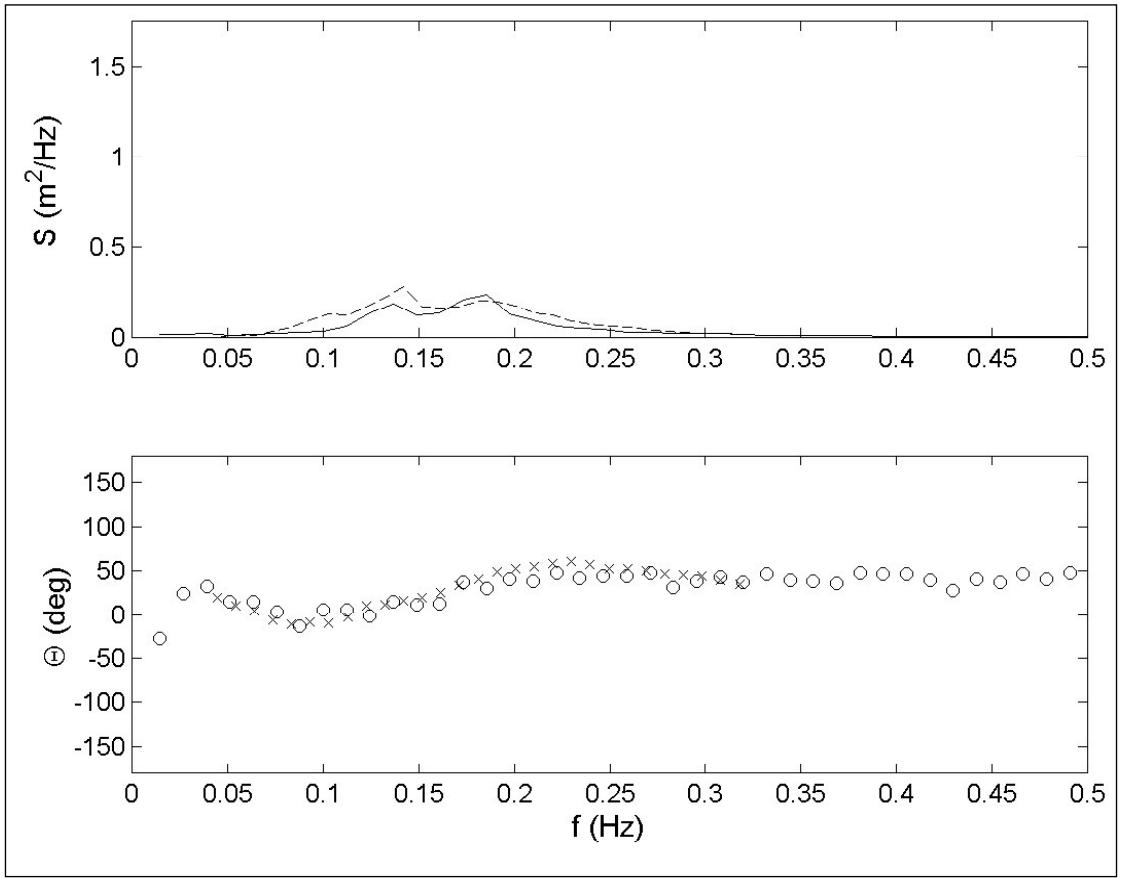

Figure 3.21 Directional spectrum for LWG (solid line and circles) and 8-m array (dashed line and x's) on 12 December 1999 at 1043 EST.

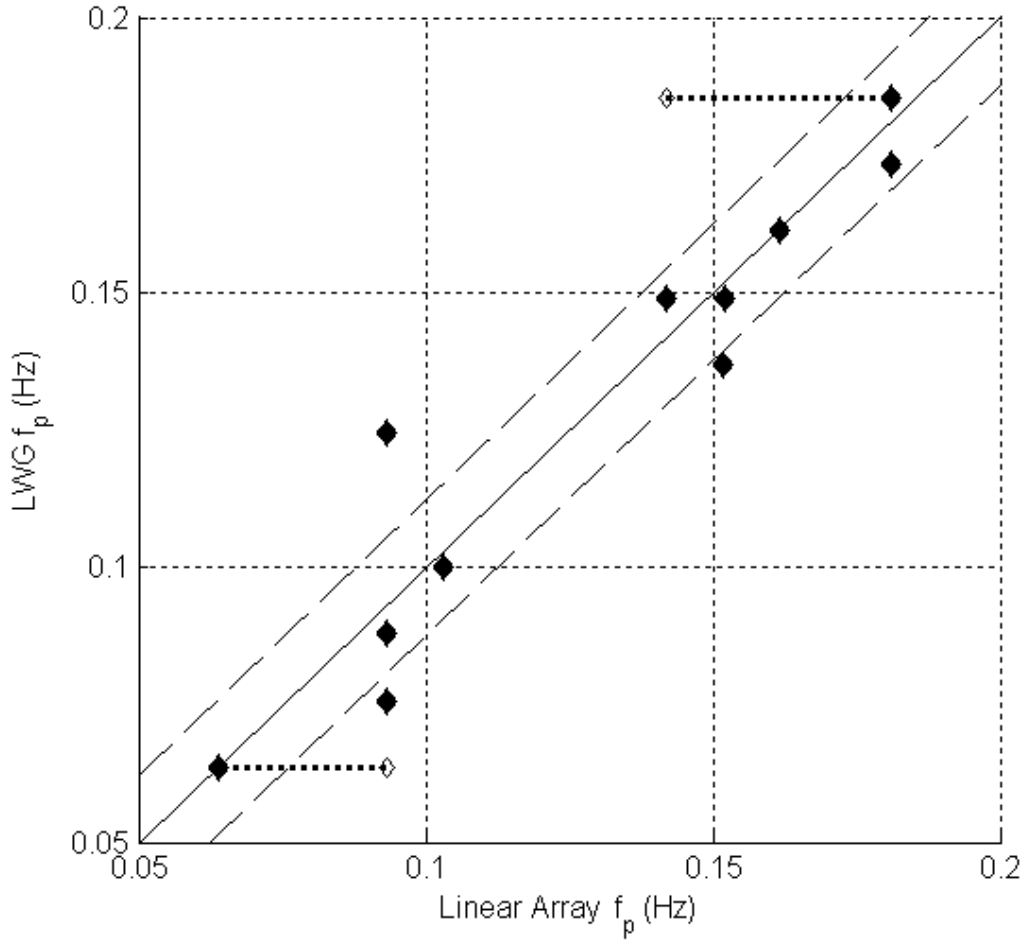

Figure 3.22 Comparison between the LWG and 8-m array peak frequency, f_p. Solid line on figure indicates an exact match while dashed lines on figure indicate one resolution frequency bandwidth.

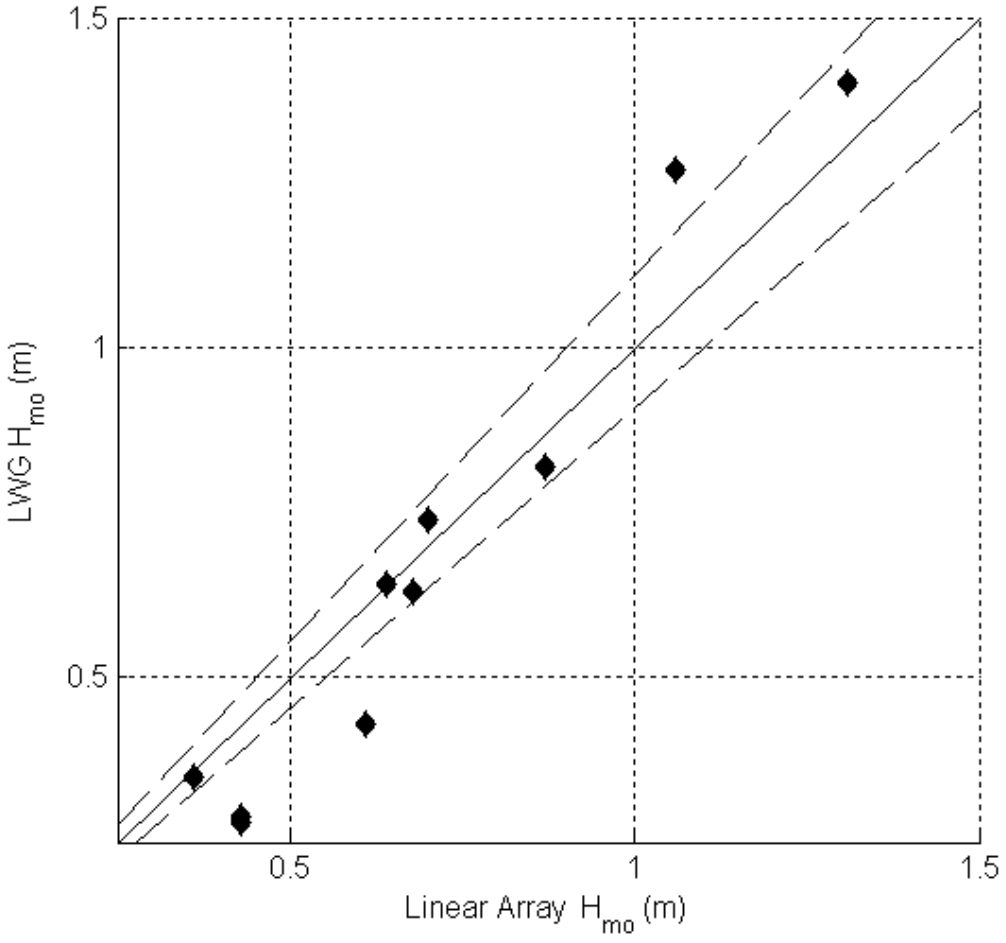

Figure 3.23 Comparison between the LWG and 8-m array spectral wave height, H_{mo}. Solid line on figure indicates an exact match while dashed lines on figure indicate 10% about the measured spectral wave height.

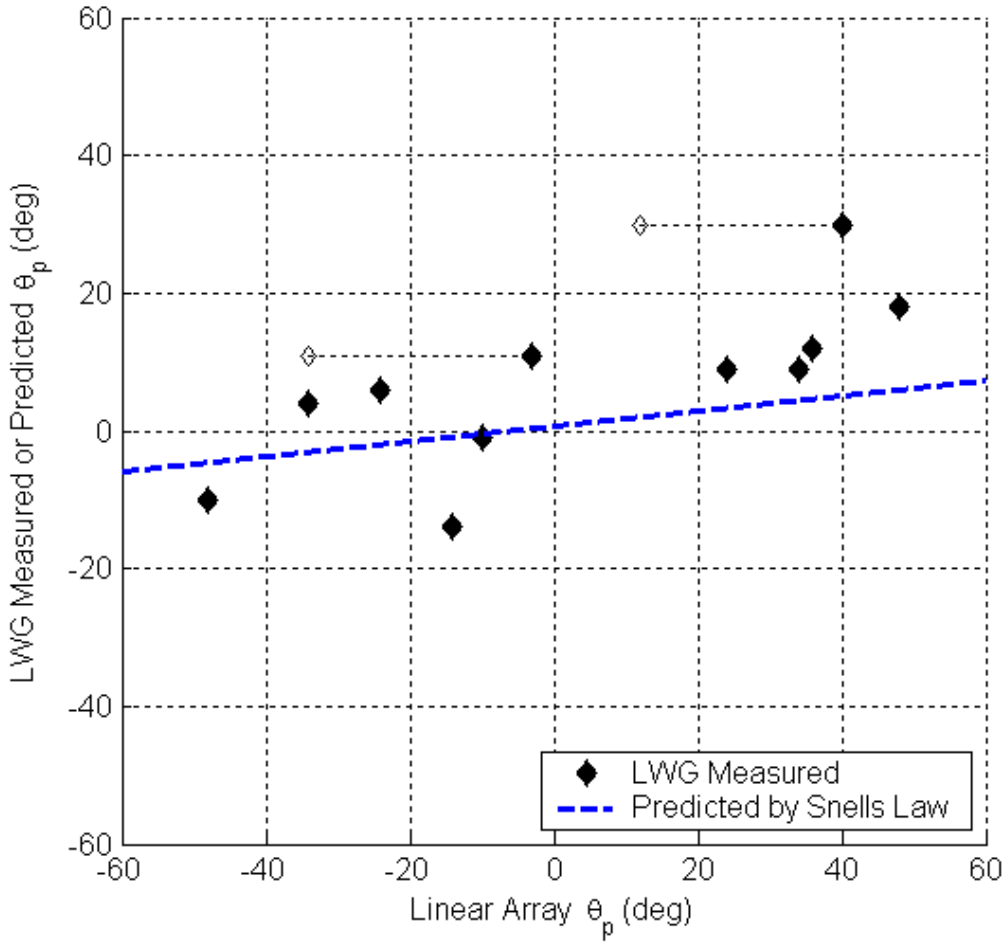

Figure 3.24 Comparison between the LWG and 8-m array peak direction, θ_p. Dashed line on the figure represents a linear fit to the peak direction as predicted by Snell's Law.

the LWG data sets is distinctly different from the peak wave frequency of the 8-m array data sets. In both cases, the energy spectra for the LWG and the 8-m array show two distinct peaks. This is depicted in the spectrum shown in Figure 3.21. In these two cases, the f and θ selected for comparison were based on the secondary peak of the spectrum. In Figure 3.22 and Figure 3.24, the actual f_p and θ_p are shown as hollow diamonds and the modified f and θ are shown as filled diamonds. When this correction is made, only one of the LWG peak frequencies is significantly different from that measured by the 8-m array.

The LWG and 8-m array H_{mo} compare well for wave heights above 0.6 m (Figure 3.23). However, the comparison is not as good for smaller wave heights. Comparison between LWG and 8-m array mean wave directions at the spectral peak frequency is reasonable (Figure 3.24). This comparison, however, is only qualitative. As waves propagate inshore, they refract to a more shore-normal orientation (approximately 0 deg relative to the FRF pier axis), as predicted by Snell's Law (Dean and Dalrymple, 1991). This trend is evident in the comparison, and all but one of the LWG data sets have a more shore-normal angle of approach, relative to the 8-m array data sets.

3.6 Future Applications

3.6.1 Additional Prototype Testing

The USACE attempted to deploy the LWG in the Currituck Sound at the FRF to evaluate its performance when measuring wind waves. The gage was configured to collect surface elevations along a four-element linear array, 70 cm in length. This additional test of the LWG was to better define the sensor's ability to

measure short-frequency, lower-energy wave fields. Cross talk between the narrowly spaced laser footprints, as narrow as 10 cm, prohibited data collection. Consequently, the experiment was abandoned.

3.6.2 Operational Lidar Wave Gage Design

Optech Inc. is developing an operational LWG design (Optech, Inc., 2001). The new LWG design requirements are summarized in Table 3.3. The exterior casing will be weatherproof, keeping out all external moisture, and all LWG components will be designed to withstand temperatures between 0° C and 40° C. Nadir angles for all ranges will be less than 6 deg, and the four ranges will form a 2-m square on the water surface when the LWG elevation above the surface is 10 m. The re-engineered LWG elevation range, power requirements and supply, data acquisition, and sensor cleaning and maintenance are optimized to meet a variety of measurement requirements.

The operational LWG design uses four-laser-beam rangefinders recording ranges from four distinct locations on the water surface (Figure 3.25). The four detectors share common detection electronics (receiver module) and timing system. This system design was selected for its cost-effectiveness, reliability, and durability.

The operational LWG design illustrated in Figure 3.25 addresses a number of issues including data storage, gage accessibility, gage power, gage durability, and unattended deployment duration. The operational LWG may prove a valuable asset for nearshore research, monitoring, and management.

Table 3.3 Operational LWG design requirements.

Elevation above water surface	2 to 20 m (variable)
Sample rate	10 Hz
Number of ranges	4
Footprint spacing	2-m square at 10-m elevation
Power requirements	24-V DC 110-V (option)
Power supply	Cable or Battery
Data acquisition	Radio modem or Cable

The results presented herein indicate that direct lidar ranging is a viable method for measuring coastal waves. For the range of environmental conditions experienced during its field deployment, the LWG accurately characterized directional-spectral characteristics of nearshore waves.

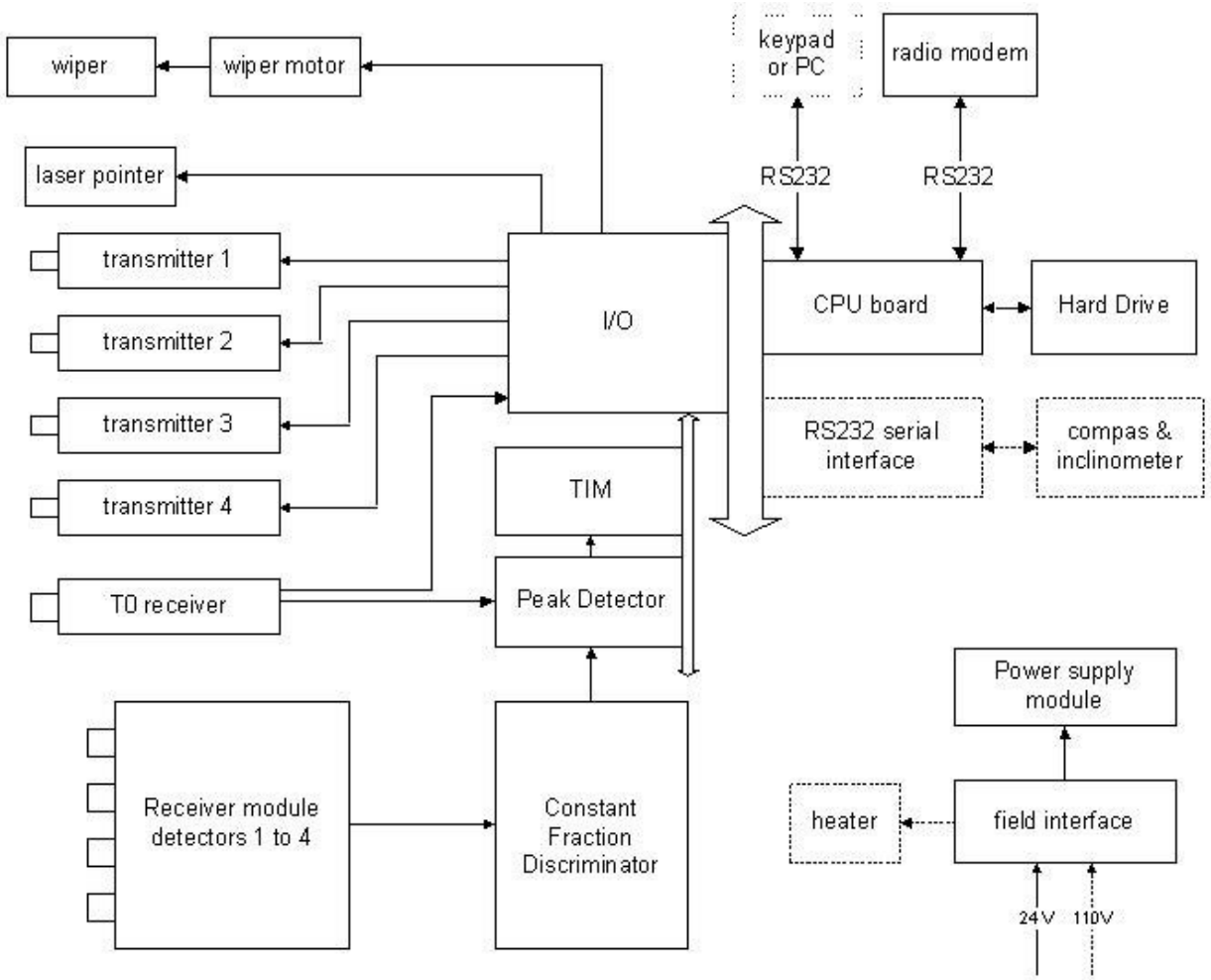

Figure 3.25 Operational LWG diagram.

Chapter 4

CONCLUSIONS

The following two sections provide recommendations for the future direction of research to advance both remote sensing of the sea bottom and of ocean waves.

4.1 Future Direction for Airborne Lidar Bathymetry Advancements

In August 2001, the 2nd International Airborne Hydrography workshop was held at Stennis Space Center, MS. The outcome of this meeting was a white paper by Irish (2001) describing the direction and focus of future research and development to advance airborne remote sensing for coastal mapping.

Table 4.1 summarizes existing ALB and other airborne operational capabilities for meeting coastal monitoring requirements. While ALB systems currently meet several measurement requirements, namely depth, elevation, shoreline position, and hazard detection, there are a number of environmental requirements that cannot be quantified with ALB sensors and algorithms, as they exist now. Further research and development is needed to improve upon some existing ALB capabilities.

4.1.1 Shallow Water Depths and Shoreline Position

For coastal monitoring initiatives, accurate bathymetric mapping within the surf zone is critical for understanding littoral processes. As such, seamless measurement capability from the nearshore through the upland beach is a goal for

Table 4.1 Existing operational ALB capabilities.

Environmental Requirement	ALB	Other Airborne	Other
Depths: 0 to 2 m	X		X
Depths: 2 to 20 m	X		X
Depths: 20 to 60 m	X		X
Depths: 60 m +			X
Elevation (topography)	X	X	X
Tides	X	X	X
Shoreline position	X	X	X
Bottom characterization			X
Sub-bottom profiling			X
Surf conditions			X
Meteorological observation		X	X
Photography	*	X	X
Ocean waves	**	X	X
Suspended sediment concentration			X

*SHOALS collects downward looking analog video.
**The operational algorithm employed by Hwang et al. (1998) to extract wave energy and directional wavenumber directly from lidar water surface returns is applicable to SHOALS surface return data.

ALB. As ALB systems exist today, accurate depth measurement in very shallow waters (i.e. depths of 2 m or less) through the land-water interface can only be achieved in areas with little or no surf zone (Guenther et al., 2000). The blue-green laser energy used to range the sea bottom cannot penetrate white-water generated by breaking waves (surf zone). Further, the infrared energy returned from white-water is often interpreted as a dry-land measurement, rather than a water-surface measurement. This technological limitation leads to two distinct problem areas: land/water discrimination and surf-zone depths. The ability to accurately distinguish between land and water in the presence of white water will greatly enhance the accuracy with which shoreline position is extracted.

4.1.1.1 Depth Measurement in the Surf Zone

There are a number of approaches for determining water depths in white water, especially in the surf zone. In many cases, mapping of surf zone depths can be achieved by modified survey planning. In areas where there is significant water level fluctuation, standard operation of an ALB mission should include a survey flight at low water plus a survey flight at high water. However, this operational procedure will not ensure depths in the surf zone at all locations for all surveys.

Recent improvements in ALB land-water discrimination algorithms may also provide additional information within the surf zone (Sosebee, 2001). These land-water discrimination algorithms should be investigated specifically to identify any potential for improving depth measurement within the surf zone.

The collection of supplementary data may be the most viable solution to measuring depths in the surf zone. Using existing or modified analysis methods,

multi- or hyper-spectral imagery (MHS) collected concurrently with lidar may be evaluated to extract water depths.

Surface elevations collected with topographic or bathymetric lidar, MHS, video, and/or photography may be analyzed to measure wave scattering and deformation. These wave characteristics are indicative of bathymetric irregularities. In addition, depth-inversion algorithms based on the phase speed of breaking waves may be used to estimate water depth and nearshore slope. Future research and development is required to assess the operational feasibility and accuracy of such methods for various ALB applications.

4.1.1.2 Detection of Coincident Surface and Bottom Returns

Processing very shallow depths, on the order of 1 m, is oftentimes challenging for an ALB system. Specifically, accurate methods for separating coincident surface and bottom returns are necessary. There are two approaches to improving processing of coincident detection of surface and bottom returns from the lidar waveform. The first approach involves the improvement and automation of the existing shallow depth algorithm employed during SHOALS post-flight processing. Specifically, the algorithm should be further developed so it can reliably detect water clarity and surf limitations on a laser shot by laser shot basis. If the algorithm can successfully detect which laser shots may be effectively reprocessed with the existing algorithm, the algorithm should be automated. The automation of this algorithm will reduce error and improve processing consistency and speed. This development approach is relatively low-risk as it builds upon existing methodology already integrated into the ALB processing procedure.

The second approach involves the investigation of polarization techniques. In general, polarization methods allow for distinction between light backscattered in one direction from light backscattered in another direction. While polarization methods have yet to be integrated with ALB systems, these methods may provide valuable additional information. Specifically, polarization techniques may allow for distinction between the surface and bottom returns recorded in the blue-green (532 nm) signal. Initial research in this area should involve the assessment of existing polarization techniques for ALB applications.

4.1.2 Sea Bottom Classification

Since ALB technology is limited by water clarity and, to a lesser extent, bottom type, it is probable that ALB waveforms contain information on these properties. Future research and algorithm development could lead to stand-alone lidar bottom classification capabilities.

To accurately describe the sea bottom, ALB must be operated with additional sensors. Research is required to assess the operational feasibility and accuracy of various technologies for bottom description. Several potential methods capitalize on additional lidar capabilities. These include the use of tunable lasers, variable frequency lasers (or the use of another laser at a frequency different than the ALB frequency), a Raman receiver configured to deeper depths to detect fluorescence, and polarization techniques. The collection of fluorescence may allow distinction between coral and other bottom types, and allow assessment of coral reef health. Ongoing research of polarization methods shows that this technology has the potential to distinguish between various material types and to distinguish between man-made and natural objects.

While preliminary tests combining ALB with MHS reveal this method is promising for determining bottom type, additional research is required to determine which spectral bands must be collected to detect which material types (Figure 4.1). Further, existing analysis methods must be interrogated and improved as needed to assure this approach meets survey accuracy requirements.

Airborne deployment of in situ measurement devices may improve description capabilities, and they should be investigated. Specifically, the use of buoys fitted with acoustic sensors, deployed from the aircraft, should be investigated for their potential to describe the sea bottom.

4.1.3 Depth Measurement in Turbid Waters

Water clarity limits ALB sensor applicability to clear-water coastal systems or to missions in very shallow water. Investigations into ways to increase depth penetration may make ALB sensors more versatile. Basic lidar research should focus on stretching existing depth-penetration capabilities. An increased depth-penetration capability will reduce the occurrence of data gaps resulting from poor water clarity in addition to increasing the offshore extent of survey coverage.

For some ALB missions, an estimate of bathymetry is better than no measurement at all. For these cases, inverse hydrodynamic modeling may be a viable option for estimating depths. Several agencies have developed inverse models, and these should be evaluated to determine their applicability and accuracy when combined with lidar surface data.

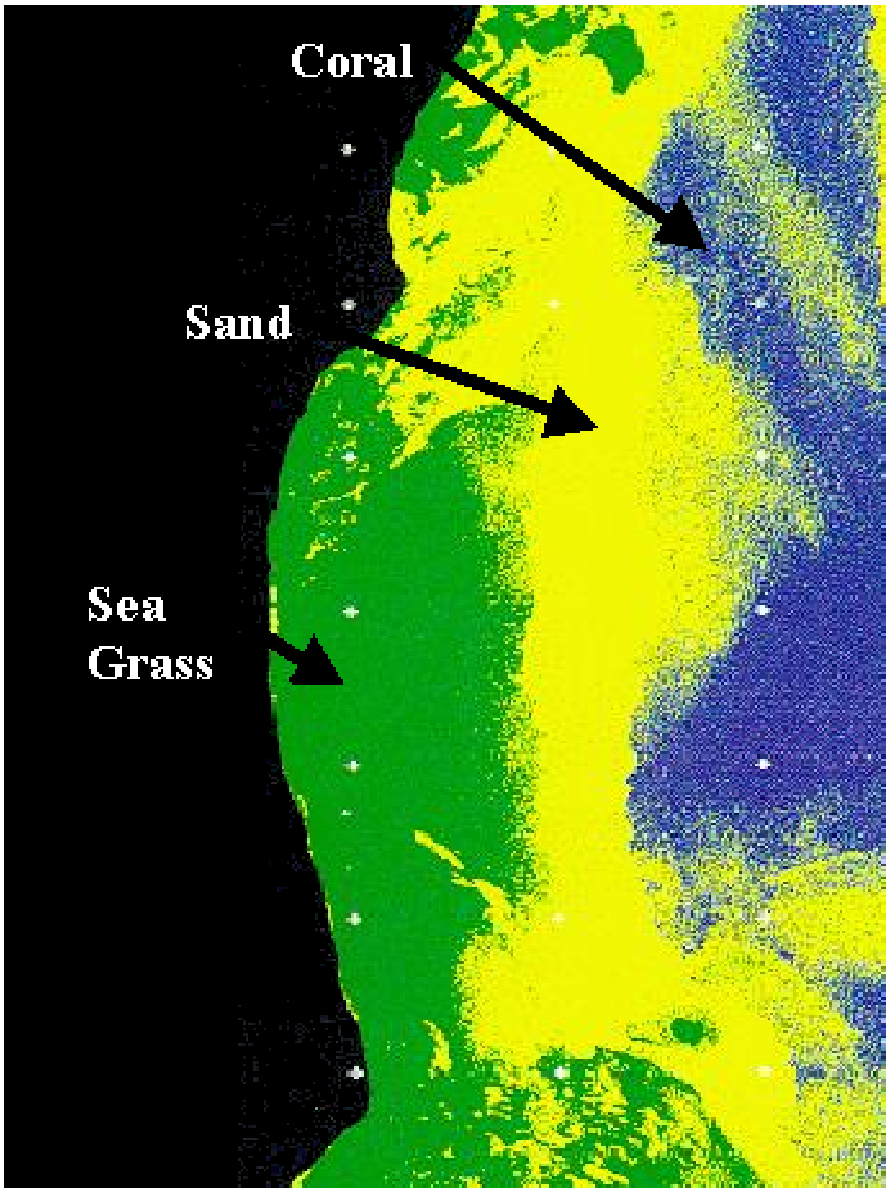

Figure 4.1 **Compact Airborne Spectrographic Imager (CASI) hyperspectral imagery fused with SHOALS data to map bottom type at Key Biscayne, FL in 1994 (from Irish, 2001).**

4.2 Future Non-Intrusive Wave Measurement

The LWG design and field testing presented in Chapter 3 demonstrate that lidar is a viable technology for directional wave measurement. However, the existing LWG design has a limited measurement region. Specifically, the sensor must be operated within a limited range of nadir angles. Present and future development with laser receiver technologies should extend the range of angles from which surface returns may be reliably detected. As such technology evolves, deployment of a fixed LWG will become more versatile. Furthermore, such technological advancements could lead to future development of a scanning lidar gage capable of measuring wave characteristics over an entire region.

4.2.1 Surf Zone and Swash Zone LWG Applications

The LWG may prove to be a viable measurement tool for investigating surf zone and swash zone processes as the LWG may be deployed in these dynamic shallow-water environments. In the surf zone, the presence of white water naturally roughens the sea surface and may therefore improve the LWG performance for wave measurement and may allow data collection from larger nadir angles. Future testing is required, however, to determine the effectiveness of the LWG for measuring surf zone waves.

Another potential application of the LWG is in measuring swash processes. Since infrared lidar energy returned varies with the reflective properties of the detected surface, it may be possible to discern the presence or absence of water in the swash zone. The improvements by Sosebee (2001) for SHOALS land/water

discrimination are likely applicable here as well. Further testing and development would be required to assess the viability of this LWG application.

4.2.2 Other Technologies

A promising new sensor, briefly introduced in Chapter 3, is the X-Band marine radar system WAMOS (Nieto Borge and Soares, 2000 and Reichert et al., 1999). This fixed-platform sensor has the capacity to synoptically measure a 1-km^2 area of the ocean surface as it evolves through time. The sensor has been used successfully to determine directional wavenumber spectra. A rigorous field testing of the WAMOS is scheduled for spring 2005 at the FRF (Resio, personal communications). Specific goals of this investigation are to quantify the accuracy of the system to determine directional energy spectra over a large coastal domain.

Fusion of lidar and X-Band radar methods may be a feasible alternative. Building on the strength of lidar to accurately range the ocean surface and the ability of X-Band radar to map a large area, directional energy spectra over large domains may be obtainable in the near future. Such a system would be ideal for monitoring a complex system such as a tidal inlet.

4.3 Concluding Remarks

Two sensors based upon lidar technology were presented herein. This study shows that near-synoptic depth measurements over large coastal regions with ALB have advanced our understanding of complex morphological processes. This technology has also proven invaluable for post-storm monitoring and regional mapping.

Some of the research proposed in Chapter 4.1 above is presently ongoing at the Joint Airborne Lidar Bathymetry Technical Center of Expertise (JALBTCX) in Stennis Space Center, MS. Furthermore, the JALBTCX recently retired the SHOALS system and introduced the next-generation ALB system, CHARTS (Heslin et al, 2003 and Guenther et al., 2002). The CHARTS system is now entering into its second year of operation.

Herein, a prototype lidar sensor for measuring temporal evolution of directional energy spectra was introduced. The data discussed in this study demonstrate that lidar methods are a viable approach for measuring ocean waves. Further development, however, is warranted to maximize the sensor's versatility. Continued research on lidar applications for monitoring the coastal zone could lead to collection of valuable future data sets to advance coastal engineering research.

BIBLIOGRAPHY

Aarninkhof, S. and Holman, R. A., 1999. Monitoring the nearshore with video. Backscatter, 10(2): 8-11.

Abbot, R. H., 1981. WRELADS II trials. Proc. 4th Laser Hydrography Symp. Defence Research Centre (Australia), Salisbury, South Australia, pp. 188-215.

Abbot, R. H. and Penny, M. F., 1975. Air trials of an experimental laser bathymeter. Tech. Note WRE-TN-1509, Department of Defence (Australia), Salisbury, South Australia.

Abbot, R. H., Watts, G. J., and Penny, M. F., 1978. WRELADS I trials report. Tech. Rep. ERL-0026-TR, Department of Defence (Australia), Salisbury, South Australia.

Alpers, W. and Hasselmann, K., 1982. Spectral signal to clutter and thermal noise properties of ocean wave imaging synthetic aperture radars. Int. J. Remote Sens., 3: 423-446.

Anderson, N., Bellemare, P., Casey, M., Malone, K., MacDougall, R., Monahan, D., O'Neil, R., and Till, S., 1983. Beginning the second hundred years: The laser sounder. Proc. Centennial Canadian Hydrographic Conference. Canadian Hydrographic Association, Burlington, Ontario, Special Publication 67.

Axelsson, R., Steinvall, O., and Sundberg, P., 1990. Programmable scanner for laser bathymetry. International Hydrographic Review, 67(1): 161-170.

Balandin, V. N. and Volodarskiy, R. D., 1979. Laser instruments for measuring the depth of shallow water. Geodeziya i Kartografiya, 2: 58-61.

Baltsavias, E. P., 1999. Airborne laser scanning: Basic relations and formulas. ISPRS J. Photogrammetry and Remote Sensing, 54: 199-214.

Banic, J., Sizgoric, S., and O'Neil, R., 1986. Scanning lidar bathymeter for water depth measurement. Proc. SPIE Laser Radar Technology and Application. SPIE, Bellingham, WA, pp. 187-195.

Bao, M., Alpers, W., and Bruning, C., 1999. A new nonlinear integral transform relating ocean wave spectra to phase image spectra of an along-track interferometric synthetic aperture radar. IEEE Trans. Geosci. Remote Sens., 37(1): 461-466.

Barrick, D. E., 1972a. First order theory and analysis of MF/HF/VHF scatter from the sea. IEEE Transactions Antennas Propag., AP-20: 2-10.

Barrick, D. E., 1972b. Remote sensing of sea stat by radar. In: V. E. Derr (Editor), Remote Sensing of the Troposphere. U.S. Government Printing Office, Washington, DC, pp. 12.1-12.46.

Barrick, D. E., 1977. Extraction of wave parameters from measured HF radar sea-echo Doppler spectra. Radio Sci., 12: 415-424.

Borman, K., 1978. Airborne Oceanographic Lidar postflight bathymetry processor, program documentation version 4.0. Planetary Sciences Department Rep. 004-78, EG&G/Washington Analytical Services Center, Inc., Riverdale, MD.

Bunkin, A. F., Vlasov, D. V., Galumyan, A. S., Mal'tsev, D. V., Mirkamilov, D. M., and Slobodyanin, V. P., 1984. Versatile airborne laser system for remote probing of ocean, atmosphere, and farmland. Soviet Physics Tech. Physics, 29(11): 1284-1287.

Cañizares, R., personal communications.

Cañizares, R., Alfageme, S., and Gravens, M., in press. Modeling of storm induced barrier island overwash and breaching in the Atlantic coast of Long Island. Proc. 29th International Conference on Coastal Engineering, American Society of Civil Engineering, New York, NY.

Carswell, A. I. and Sizgoric, S., 1974. Underwater probing with laser radar. Proc. The Uses of Lasers for Hydrographic Studies. National Aeronautics and Space Administration, Wallops Island, VA, pp. 89-103.

Casey, M. J., 1984. Deploying the lidar on hydrographic surveys. Proc. 9th Canadian Symposium on Remote Sensing. Memorial University, St. Johns, Newfoundland, pp. 165-175.

Casey, M. J., O'Neil, R. A., and Conrad, P., 1985. The advent of LARSEN. Proc. Canadian Hydrographic Conference. Canadian Hydrographic Association, Burlington, Ontario, pp. 7-12.

Chavez, P. S., Velasco, M. G., Isbrecht, J., Field, M. E., and Roberts, C., 2000. Use of digitized multitemporal aerial photographs to monitor and detect change in clear shallow coastal waters, Molokai, Hawaii. Proc. National Beach Preservation Conference. American Shore and Beach Preservation Association, Concord, CA, pp. 1-2 (published on CDROM).

Clegg, J. E. and Penny, M. F., 1978. Depth sounding from the air by laser beam. J. Navigation, 31(1): 52-61.

Compton, J. S., and Hudson, M. A., 1988. New charting technology in Australia: The Laser Airborne Depth Sounder. International Hydrographic Review, LXV(2): 145-157.

Crombie, D. D., 1955. Doppler spectrum of sea echo at 13.56 MC/S. Nature, 175: 681-682.

Cunningham, L. L., 1972. Test report on Pulsed Light Airborne Depth Sounder (PLADS). Naval Oceanographic Office Tech. Note 6620-102-72, U.S. Navy, Washington, DC.

Curtis, W. R., Hathaway, K. K., Holland, K. T., and Seabergh, W. C., 2002. Video-based wave direction measurements in a scale physical model. CHETN-IV-49, U.S. Army Corps of Engineers Waterways Experiment Station, Vicksburg, MS.

Dean, R. G., 1982. Summary. Symp. and Workshop on Wave-Measurement Technology. National Academy of Engineering, Washington, DC: pp. 1-13.

Dean, R. G. and Dalrymple, R. A., 1991. Water Wave Mechanics for Engineers and Scientists. World Scientific Publishing, Singapore.

Driver, D., 1985. Remote sensing techniques for measuring ocean waves. CETN-I-26, U.S. Army Corps of Engineers Waterways Experiment Station, Vicksburg, MS.

Driver, D., 1986. High frequency radar measurements of coastal ocean parameters. CETN-I-41, U.S. Army Corps of Engineers Waterways Experiment Station, Vicksburg, MS.

Earle, M. D., McGehee, D., and Tubman, M., 1995. Field wave gaging program, wave data analysis standards. IR CERC-95-1, U.S. Army Corps of Engineers Waterways Experiment Station, Vicksburg, MS.

Feigels, V. I., and Kopilevich, Y. I., 1993. Russian airborne lidar for oceanography. Proc. Symp. on Russian airborne geophysics and remote sensing. SPIE, Bellingham, WA, Vol. 2111, pp. 127-141.

Ferguson, G. D., 1975. Blue-green lasers for underwater applications. Proc. SPIE Conf. on Ocean Optics. SPIE, Bellingham, WA, pp. 150-156.

Forget, P. and Broche, R., 1996. Slicks, waves, and fronts observed in a sea coastal area by an X-Band airborne synthetic aperture radar. Remote Sens. Environ., 57: 1-12.

Frasier S. J. and McIntosh, R. E. 1996. Observed wavenumber-frequency properties of microwave backscatter from the ocean surface at near-grazing angles. J. Geophys. Res., 101(C8): 18391-18407.

Frasier, S. J., Liu, Y., and McIntosh, R. E, 1998. Space-time properties of radar sea spikes and their relation to wind and wave conditions. J. Geophys. Res., 103(C9): 18745-18757.

Goldstein, R. M. and Zebker, H. A., 1987. Interferometric radar measurements of ocean surface currents. Nature, 328: 707-709.

Goldstein, R. M., Barnett, T. P., and Zebker, H. A., 1989. Remote sensing of ocean currents. Science, 246: 1282-1285.

Grace, P. J., 1989. Investigation of breakwater stability at Presque Isle Pennsylvania Erie Pennsylvania. TR-CERC-89-3, U.S. Army Corps of Engineers Waterways Experiment Station, Vicksburg, MS.

Greenberg, M. D., 1988. Advanced Engineering Mathematics. Prentice-Hall, Englewood Cliffs, NJ.

Grosskopf, W. G., Aubrey, D. G., Mattie, M. G., and Mathiesen, M., 1983. Field intercomparison of nearshore directional wave sensors. IEEE J. Oceanic Engineering, OE-8(4): 254-271.

Guenther, G. C., 1985. Airborne laser hydrography: System design and performance factors. NOAA Professional Paper Series, National Ocean Service 1, National Oceanic and Atmospheric Administration, Rockville, MD.

Guenther, G. C., in press. Airborne lidar bathymetry. In: Digital Elevation Models. American Society of Photogrammetry and Remote Sensing, Annapolis Junction, MD, pp. 8.1-8.73.

Guenther, G. C. and Goodman, L. R., 1978. Laser applications for near-shore nautical charting. Proc. SPIE Ocean Optics V. SPIE, Bellingham, WA, Vol. 160, pp. 174-183.

Guenther, G. C. and Borman, K., 1981. Depth estimation in the Airborne Oceanographic Lidar postflight bathymetry processor. NOAA Tech. Memorandum OTES 02, National Oceanic and Atmospheric Administration, Washington, DC.

Guenther, G. C. and Thomas, R. W. L., 1983. System design and performance factors for airborne laser hydrography. Proc. SPIE Ocean Optics VII. SPIE, Bellingham, WA, Vol. 489, pp. 287-296.

Guenther, G. C. and Mesick, H. C., 1988. Analysis of airborne laser hydrography waveforms. Proc. SPIE Ocean Optics IX. SPIE, Bellingham, WA, Vol. 925, pp. 232-241.

Guenther, G. C. Goodman, L. R., Hoge, F., Swift, R. N., Thomas, R. W. L., and Bright, D., 1979. AOL project: Results to date. Proc. Airborne Laser Hydrography Symposium III. National Oceanic and Atmospheric Administration, Rockville, MD, pp. 62-103.

Guenther, G. C., Thomas, R. W. L., and LaRocque, P. E., 1996. Design considerations for achieving high accuracy with the SHOALS bathymetric lidar system. Proc. SPIE: Laser Remote Sensing of Natural Waters: From Theory to Practice. SPIE, Bellingham, WA, Vol. 15, pp. 54-71.

Guenther, G. C., Cunningham, A. G., LaRocque, P. E., and Reid, D. J., 2000. Meeting the accuracy challenge in airborne lidar bathymetry. Proc. EARSeL Symp. Workshop on Lidar Remote Sensing of Land and Sea. EARSeL, Paris, pp. 1-27 (published on CDROM).

Guenther, G. C., Lillycrop, W. J., and Banic, J. R., 2002. Future advancements in airborne hydrography. International Hydrographic Review, 3(2): 67-90.

Hashimoto, N., Kobune, K., and Kameyama, Y., 1987. Estimation of directional spectrum using the Bayasian approach, and its application to field data analysis. Rept. P. H. R. I., 25(5): 57-100.

Hashimoto, N., Wyatt, L., and Kojima, S., 2003. Verification of a Bayesian method for estimating directional spectra from HF radar surface backscatter. Coastal Engineering, 45(2): 255-274.

Hasselmann, K., 1971. Determination of ocean wave spectra from Doppler return from sea surface. Nature, Physical Science, 229: 16-17.

Heslin, J. B., Lillycrop, W. J., and Pope, R. W., 2003. CHARTS: An evolution in airborne lidar hydrography. Proc. U.S. Hydro 2003. The Hydrographic Society of America, Rockville, MD, pp. 5.2.1-5.2.4 (published on CDROM).

Hessner, K., Reichert, K., Dittmer, J., and Nieto Borge, J. C., 2003. Ocean wave measurements by X-Band radar – from spectral wave parameters to single wave detection. Proc. Radar and Marine Environment, SEE Workshop. European Centre for Information on Marine Science and Technology, Lisbon, pp. C03.1-C03.6 (published on CDROM).

Hickman, G. D. and Hogg, J. E., 1969. Application of an airborne pulsed laser for near-shore bathymetric measurements. Remote Sens. Environ., 1: 47-58.

Hickman, G. D., Hogg, J. E., and Ghovanlou, A. H., 1972. Pulsed neon laser bathymetric studies using simulated Delaware Bay waters. Technical Report No. 1, ONR/NOAA/USGS Contract No. N000-14-71C-0202, Sparcom, Inc., Alexandria, VA.

Hickman, G. D., Gault, C. S., Ghovanlou, A. H., Friedman, E. J., and Hogg, J. E., 1974. Airborne laser shallow water bathymetric system. Final Report, ONR/NOAA/USGS Contract No. N000-14-71c-0202, Sparcom, Inc. Alexandria, VA.

Higgins, A. L., Seymour, R. J., and Pawka, S. S., 1981. A compact representation of ocean wave directionality. Applied Ocean Research, 3(3): 105-112.

Hisaki, Y. and Tokuda, M., 2001. VHF and HF sea echo Doppler spectrum for a finite illuminated area. Radio Sci., 36(3): 425-440.

Hoge, F. E., Swift, R. N., and E. B. Frederick, 1980. Water depth measurement using an airborne pulsed neon laser system. Appl. Opt., 19(6): 871-883.

Howell, G. L., 1998. Shallow water directional wave gages using short baseline arrays. Coastal Engineering, 35: 85-102.

Huang, N. E., Shen, Z., and Long, S. R., 1999. A new view of nonlinear water waves: The Hilbert spectrum. Annual Review of Fluid Mechanics, 31: 417-457.

Hwang, P. A. and Walsh, E. J., 1998. Remote sensing and coastal wave research. Proc. Coastal Dynamics 1997. American Society of Civil Engineers, New York, NY, pp. 337-345.

Hwang, P. A., Walsh, E. J., Krabill, W. B., Swift, R. N., Manizade, S. S., Scott, J. F., and Earle, M. D., 1998. Airborne remote sensing applications to coastal wave research. J. Geophys. Res., 103: 18791-18800.

Hwang, P. A., Krabill, W. B., Wright, W., Swift, R. N., and Walsh, E. J., 2000a. Airborne scanning lidar measurement of ocean waves. Remote Sens. Environ., 73: 236-246.

Hwang, P. A., Wang, D. W., Walsh, E. J., Krabill, W. B., Wright, W., and Swift, R. N., 2000b. Directional wavenumber spectra of ocean surface waves: Part 1. Spectral slope and dimensionless spectral coefficient. J. Phys. Oceanogr., 30: 2753-2767.

Hwang, P. A., Wang, D. W., Walsh, E. J., Krabill, W. B., Wright, W., and Swift, R. N., 2000c. Directional wavenumber spectra of ocean surface waves: Part 2. Directional distribution, J. Phys. Oceanogr., 30: 2768-2787.

Hwang, P. A., Kaihatu, J. M., and Wang, D. W., 2002a. A comparison of the energy flux computation of shoaling waves using Hilbert and wavelet spectral analysis techniques. Proc. 7th Int. Workshop on Wave Hindcasting and Forecasting. Oceanweather, Inc., Cos Cob, CT, pp. G.4.1-G.4.5 (published on CDROM).

Hwang, P. A., Wright, W., Krabill, W. B., and Swift, R. N., 2002b. Airborne remote sensing of breaking waves. Remote Sens. Environ., 80: 65-75.

Irish, J. L., 1997. Navigation channel prediction sensitivity to wave field characterization. PIANC Bulletin, 95-1997: 5-20.

Irish, J. L., 2000. An introduction to coastal zone mapping with airborne lidar: The SHOALS system. Proc. Corso di Aggiomamento Techniche per la Difesa Dallinquinamento, University of Calabria, Cosenza, Italy, pp. 1-8 (published on CDROM).

Irish, J. L., 2001. Airborne Hydrography Research and Development Plan. White Paper, Joint Airborne Lidar Bathymetry Technical Center of Expertise, U.S. Army Corps of Engineers, Mobile, AL.

Irish, J. L. and Truitt, C. L., 1995. Beach fill response at Longboat Key, Florida. Proc. National Conference on Beach Preservation Technology. Florida Shore and Beach Preservation Association, Tallahassee, FL, pp. 103-117.

Irish, J. L. and Lillycrop, W. J., 1997. Monitoring New Pass, Florida with high density lidar bathymetry. J. Coastal Research, 13(4): 1130-1140.

Irish, J. L. and White, T. E., 1998. Coastal engineering applications of high-resolution lidar bathymetry. Coastal Engineering, 35: 47-71.

Irish, J. L. and Lillycrop, W. J., 1999. Scanning laser mapping of the coastal zone: The SHOALS system. ISPRS J. Photogrammetry and Remote Sensing, 54: 123-129.

Irish, J. L., Thomas, E. J., Parson, L. E., and Lillycrop, W. J., 1996. Monitoring storm response with high density lidar bathymetry: The effects of Hurricane Opal on Florida's panhandle. Proc. 2nd International Airborne Remote Sensing Conference and Exhibition. Environmental Research Institute of Michigan, Ann Arbor, MI, Vol. 3, pp. 723-732.

Irish, J. L., Lillycrop, W. J., and Parson, L. E., 1997. Accuracy of sand volumes as a function of survey density. Proc. 25th International Conference on Coastal Engineering, American Society of Civil Engineers, New York, NY, Vol. 3, pp. 3736-3749.

Irish, J. L., McClung, J. K., and Lillycrop, W. J., 2000a. Airborne lidar bathymetry: The SHOALS system. PIANC Bulletin, 2000(103): 43-53.

Irish, J. L., Wozencraft, J. M., and Cunningham, A. G., 2000b. Lidar sensor for measuring directional-spectral characteristics of water waves. EARSeL Symposium 2000. EARSeL, Paris, pp. 1-9 (published on CDROM).

Irish, J. L., Wozencraft, J. W., and Cunningham, A. G., 2001. Water wave measurement with lidar from a fixed platform. Proc. Coastal Dynamics 2001. American Society of Civil Engineers, New York, NY, pp. 998-1006.

Irish, J. L., Cañizares, R., and Grosskopf, W. G., 2004. The effect of hindcasted waves on coastal storm water levels during the blizzard of 2003. Proc, 8th International Workshop on Wave Hindcasting and Forecasting, U.S. Army Corps of Engineers, Waterways Experiment Station, Vicksburg MS, pp. 1-11 (published on CDROM).

Irish, J. L., Williams, B. P., Militello, A., and Mark, D. J., in press. Regional-scale storm-surge modeling of Long Island, New York, U.S.A. Proc. 29th International Conference on Coastal Engineering, American Society of Civil Engineers, New York, NY.

Irish, J. L., Wozencraft, J. W., Cunningham, A. G., and Giroud, C., submitted. Non-intrusive measurement of waves: Lidar wave gage. J. Atmos. Oceanic Technol.

Ivanov, A. P., Skrelin, A. L., and Sherbaf, I. S., 1972. Study of optical characteristics of water media using pulsed sounding. ZhPS, 17(2): 232-240.

Jerlov, N. G., 1976. Marine Optics, Elsevier Scientific Publication Company, Amsterdam.

Kim, H. H., Cervenka, P., and Lankford, C., 1975. Development of an airborne laser bathymeter. NASA Technical Note TND-8079, National Aeronautics and Space Administration, Washington, DC.

Kirby, J. T., 1998. Analysis of regular and random ocean waves. Spring 1998 Water Wave Spectra course notes, University of Delaware, Center for Applied Coastal Research, Newark, DE.

Koppari, K., Karlsson, U., and Steinvall, O., 1994. Airborne laser depth sounding in Sweden. International Hydrographic Review, LXXI(2): 69-90.

Krabill, W. B., Thomas, R. H., Martin, C. F., Swift, R. N., and Frederick, E. B., 1995. Accuracy of airborne laser altimetry over the Greenland ice sheet. Int. J. Remote Sens., 16: 1211-1222.

Leffler, M. W., Baron, C. F., Scarborough, B. L., Hathaway, K. K., Hodges, P. R., and Townsend, C. R., 1996. Annual data summary for the 1994 CERC Field Research Facility. TR CERC-96-9, U.S. Army Corps of Engineers Waterways Experiment Station, Vicksburg, MS.

Lillycrop, L. S., personal communications.

Lillycrop, W. J., Parson, L. E., and Guenther, G. C., 1993. Processing lidar returns to extract water depth. Proc. Int. Symp. on Spectral Sensing Research. SPIE, Bellingham, WA, pp. 1131-1136.

Lillycrop, W. J., Parson, L. E., Estep, L. L., LaRocque, P. E. ,Guenther, G. C., Reed, M. D., and Truitt, C. L., 1994. Field testing of the U.S. Army Corps of Engineers airborne lidar hydrographic survey system. Proc. U.S. Hydrographic Conference 1994. The Hydrographic Society of America, Rockville, MD, Special Publication No. 32, pp. 144-151.

Lipa, B., 1977. Derivation of directional ocean-wave spectra by integral inversion of second-order radar echos. Radio Sci., 12(3): 425-434.

Lipa, B. and Barrick, D. E., 1986. Extraction of sea state from HF radar sea echo: Mathematical theory and modeling. Radio Sci., 21: 81-100.

Lippmann, T. C. and Holman, R. A., 1991. Phase speed and angle of breaking waves measured with video techniques. Proc. Coastal Sediments 1991. American Society of Civil Engineers, New York, NY, pp. 542-556.

Liu, P. C. and Ross, D. B., 1980. Airborne measurements of wave growth for stable and unstable atmospheres in Lake Michigan. J. Phys. Oceanogr., 10: 1842-1853.

Liu, Z. S., 1990. Estimate of maximum penetration depth of lidar in coastal water of the China Sea. Proc. SPIE Ocean Optics X. SPIE, Bellingham, WA, Vol. 1302, pp. 655-661.

Loewen, M. R. and Melville, W. K., 1991. Microwave backscatter and acoustic radiation from breaking waves. J. Fluid Mech., 224: 601-623.

Long, C. E., 1996. Index and bulk parameters for frequency-direction spectra measured at CERC Field Research Facility, June 1994 to August 1995. MP CERC-96-5, U.S. Army Corps of Engineers Waterways Experiment Station, Vicksburg, MS.

Longuet-Higgins, M. S., Cartwright, D. E., and Smith, N. D., 1963. Observations of the directional spectrum of the sea waves using the motions of a floating buoy. In: Ocean Wave Spectra. Prentice-Hall, Englewood Cliffs, NJ, pp. 111-136.

Lyzenga, D. R., and Ericson, E. A., 1998. Numerical calculations of radar scattering from sharply peaked ocean waves. IEEE Trans. Geosci. Remote Sens., 36(2): 636-646.

Marom, M., Goldstein, R. M., Thorton, E. B., and Shemer, L., 1990. Remote sensing of ocean wave spectra by interferometric synthetic aperture radar. Nature, 345: 793-795.

McClung, J. K., 2000. Observing and modeling the wave-driven, landward migration of sand shoals at tidal inlets. Master of Science Thesis, University of South Alabama, Mobile, AL.

Melville, W. K., Loewen, M. R., Felizardo, F. C., Jessup, A. T., and Buckingham, M. J., 1988. Acoustic and microwave signatures of breaking waves. Nature, 336: 54-56.

Miller, H. C., Smith, S. J., Hamilton, D. G., and Resio, D. T., 1999. Cross-shore transport processes during onshore bar migration. Proc. Coastal Sediments 1999. American Society of Civil Engineers, New York, NY, pp. 1065-1080.

Mohr, M. C., 1994. Presque Isle shoreline erosion control project. Shore and Beach, 62: 23-28.

Morang, A., 1993. Geological and physical processes at a Gulf of Mexico tidal inlet, East Pass, Florida. Ph.D. Dissertation, Louisiana State University, Baton Rouge, LA.

Morang, A., Irish, J. L., and Pope, J., 1996. Hurricane Opal morphodynamic impacts on East Pass, Florida: Preliminary findings. Proc. 1996 National Conference on Beach Preservation Technology. Florida Shore and Beach Preservation Association, Tallahassee, FL, pp. 192-208.

Nairn, R., 1994. Royal Australian Navy Laser Airborne Depth Sounder, the first year of operations. International Hydrographic Review, LXXI(1): 109-119.

Nieto Borge, J. C. and Soares, 2000. Analysis of directional wave fields using X-Band navigation radar. Coastal Engineering, 40: 375-391.

Nieto Borge, J. C., Reichert, K., and Dittmer, J., 1999. Use of nautical radar as a wave monitoring instrument. Coastal Engineering, 37: 331-342.

O'Neil, R. A., 1981. Field trials of a lidar bathymeter in the Magdalen Islands. Proc. 4th Laser Hydrography Symposium. Defence Research Centre (Australia), Salisbury, South Australia, pp. 56-84.

O'Neil, R. A., Thomson, V., de Villiers, J. N., and Gibson, J. R., 1978. The aerial hydrography program at CCRS. Proc. Coastal Mapping Symp. National Oceanographic and Atmospheric Administration, Rockville, MD, pp. 125-132.

Optech, Inc., 1999. SENTINEL 3100 User Manual. Document No. 290-000123(5), Optech, Inc., North York, Ontario.

Optech, Inc., 2001. Laser wave gauge design document. Optech, Inc., North York, Ontario.

Ott, L. M., 1965. Underwater ranging measurements using blue-green laser. NAVAIRDEVCEN Report No. NADC-AE-6519, U.S. Naval Air Development Center, Warminster, PA.

Parson, L. E., and Smith, J. B., 1995. Assessment of native beach characteristics for St. Joseph, Michigan – Southeastern Lake Michigan. MP-CERC-95-2, U.S. Army Corps of Engineers Waterways Experiment Station, Vicksburg, MS.

Pawka, S. S., 1982. Wave directional characteristics on a partially sheltered coast. Ph.D. Dissertation, Scripps Institution of Oceanography, University of California, San Diego, CA.

Pawka, S. S., 1983. Island shadows in wave directional spectra. J. Geophys. Res., 88: 2579-2591.

Penny, M. F., 1981. Laser hydrography in Australia. Proc. Int. Conf. on Lasers 1981. SPIE, Bellingham, WA, pp. 1029-1042.

Penny, M. F., Billard, B., and Abbot, R. H., 1989. LADS: The Australian laser airborne depth sounder. Int. J. Remote Sens., 10(9): 1463-1479.

Pope, J. and Lillycrop, W. J., 1988. Development of a helicopter lidar bathymeter system. Proc. U.S. Army Corps of Engineers Surveying Conference. U.S. Army Corps of Engineers, Fort Belvoir, VA, pp. 213-216.

Pope, R. W., Reed, B. A., West, G. R., and Lillycrop, W. J., 1997. Use of an airborne laser depth sounding system in a complex shallow-water environment. Proc. Hydrographic Symp. XVth Int. Hydro Conf. International Hydrographic Organization, Monaco, pp 17.

Reichert, K., Hessner, K., Nieto Borge, J. C., and Dittmer, J., 1999. WAMOS II: A radar based wave and current monitoring system. Proc. 9th International Offshore Polar Engineering Conf. 1999. International Society of Offshore and Polar Engineers, Cupertino, CA, Vol. 3, pp. 139-143.

Resio, D., personal communications.

Rice, S. O., 1951. Reflection of electromagnetic waves from slightly rough surfaces. Commun. Pure Appl. Math., 4: 351-378.

Riley, J. L., 1995. Evaluating SHOALS bathymetry using NOAA hydrographic survey data. Proc. 24th Joint Meeting of UJNR Sea-Bottom Surveys Panel. National Oceanographic and Atmospheric Administration, Rockville, MD, pp. 10.

Robinson, L., 1995. Hurricane Opal reconnaissance report. U.S. Army Corps of Engineers, Mobile District, Mobile, AL.

Ross, D. B., Peloquin, R. A., and Sheil, R. J., 1968. Observing ocean surface waves with a helium neon laser. Proc. 5th Symposium on Military Oceanography. U.S. Navy, Alexandria, VA.

Ross, D. B., Cardone, V. J., and Conaway, J. W. Jr., 1970. Laser and microwave observations of sea-surface condition for fetch-limited 17- to 25-m/s winds. IEEE Trans. Geosci. Remote Sens., GE-8: 326-336.

Saville, T. and Caldwell, J. M., 1952. Accuracy of hydrographic surveying in and near the surf zone. Proc. 1952 Coastal Engineering Conference, American Society of Civil Engineers, New York, NY.

Schule, J. J., Simpson, L. S., and DeLeonibus, P. S., 1971. A study of fetch-limited wave spectra with an airborne laser. J. Geophys. Res., 76(18): 4160-4171.

Setter, C. and Willis, R. J., 1994. LADS: From development to hydrographic operations. Proc. U.S. Hydrographic Conference 1994. The Hydrographic Society, The Hydrographic Society of America, Rockville, MD, Special Publication No. 32, pp. 134-139.

Shannon, J. G., 1975. Correlation of beam and diffuse attenuation coefficients measured in selected ocean waters. Proc. SPIE Conf. on Ocean Optics. SPIE, Bellingham, WA, Vol. 64, pp. 3-11.

Sinclair, M., 1999. Laser hydrography–commercial survey operations. Proc. U.S. Hydrographic Conference 1999. The Hydrographic Society of America, Rockville, MD, pp. 9.2.1-9.2.10 (published on CDROM).

Sizgoric, personal communications.

Sorenson, G. P., 1966. Proposed airborne fathometer system for high-speed offshore beach mapping. Technical Note, Stanford Research Institute, Menlo Park, CA.

Sorenson, G. P., Honey, R. C., and J. R. Payne, 1966. Analysis of the use of airborne laser radar for submarine detection and ranging. SRI Report No. 5583, Stanford Research Institute, Menlo Park, CA.

Sosebee, C., 2001. Improvement of the land/water discrimination algorithm for the U.S. Army Corps of Engineers Scanning Hydrographic Operational Airborne Lidar System. Master of Science Thesis, Cornell University, Ithaca, NY.

Steinvall, O., Klevebrant, H., Lexander, J., and Widen, A., 1981. Laser depth sounding in the Baltic Sea. Appl. Opt., 20(19): 3284-3286.

Steinvall, O., Koppari, K., and Karlsson, U., 1992. Experimental evaluation of an airborne depth sounding lidar. Proc. SPIE Lidar for Remote Sensing. SPIE, Bellingham, WA, Vol. 1714, pp. 108-126.

Steinvall, O., Koppari, K., and Karlsson, U., 1994. Airborne laser depth sounding: System aspects and performance. Proc. SPIE Ocean Optics XII. SPIE, Bellingham, WA, Vol. 2258, pp. 392-412.

Stockdon, H. and Holman, R. A., 2000. Estimation of wave phase speed and nearshore bathymetry from video imagery. J. Geophys. Res., 105 (C9): 22015-22033.

Suhayda, I. N., and Pettigrew, N. R., 1977. Observations of wave height and wave celerity in the surf zone. J. Geophys. Res., 82(9): 1419-1424.

Thomas, R. W. L., and Guenther, G. C., 1990. Water surface detection strategy for an airborne laser bathymeter. Proc. SPIE Ocean Optics X. SPIE, Bellingham, WA, Vol. 1302, pp. 597-611.

Tsai, B. M., and Gardener, C. S., 1982. Remote sensing of sea state using laser altimeters. Appl. Opt., 21: 3932-3940.

Walrafen, G. E., 1967. Raman spectral studies of the effects of temperature on water structure. J. Chemical Physics, 47(1): 114-126.

Wehr, A. and Lohr, U., 1999. Airborne laser scanning–an introduction and overview. ISPRS J. Photogrammetry and Remote Sensing, 54: 68-82.

Witt, A. K., Shannon, J. G., Rankin, M. B., and Fuchs, L. A., 1976. Air/underwater laser radar test results, analysis, and performance predictions. Report No. NADC-76005-20, U.S. Naval Air Development Center, Warminster, PA.

Wozencraft, J. M., personal communications.

Wozencraft, J. M. and Irish, J. L., 2000. Airborne lidar surveys and regional sediment management. Proc. EARSeL Symposium 2000. EARSeL, Paris, pp. 1-11 (published on CDROM).

Wozencraft, J. M., Irish, J. L., Wiggins, C. E., Stupplebeen, H., and Chaves, P. S., 2000. Regional mapping for coastal management: Maui and Kauai, Hawaii. Proc. National Beach Preservation Conference. American Shore and Beach Preservation Association, Concord, CA, pp. 1-4 (published on CDROM).

Wu, J., 1971. Slope and curvature distribution of wind-disturbed water surface. J. Optical Society of America, 61(7): 852.

Wu, J., 1972. Surface curvature of wind waves observed from different angles. J. Optical Society of America, 62(3): 395.

Young, I. R., Rosenthal, W., and Ziemer, F., 1985. A three-dimensional analysis of marine radar images for the determination of ocean wave directionality and surface currents. J. Geophys. Res., 90: 1049-1065.